8-2008

The Applications of the Tracer Particle Method to Multi-Dimensional Supernova Simulations

Ching-Tsai Lee
University of Tennessee - Knoxville

To the Graduate Council:

I am submitting herewith a dissertation written by Ching-Tsai Lee entitled "The Applications of the Tracer Particle Method to Multi-Dimensional Supernova Simulations." I have examined the final electronic copy of this dissertation for form and content and recommend that it be accepted in partial fulfillment of the requirements for the degree of Doctor of Philosophy, with a major in Physics.

Mike W. Gudiry, Major Professor

We have read this dissertation and recommend its acceptance:

John Quinn, Raphael Hix, Carl Sundberg, Kate Jones

Accepted for the Council:

Carolyn R. Hodges

Vice Provost and Dean of the Graduate School

(Original signatures are on file with official student records.)

To the Graduate Council:

I am submitting herewith a dissertation written by Ching-Tsai Lee entitled "The Applications of the Tracer Particle Method to Multi-Dimensional Supernova Simulations." I have examined the final electronic copy of this dissertation for form and content and recommend that it be accepted in partial fulfillment of the requirements for the degree of Doctor of Philosophy, with a major in Physics.

Mike W. Gudiry
Major Professor

We have read this dissertation
and recommend its acceptance:

John Quinn

Raphael Hix

Carl Sundberg

Kate Jones

Accepted for the Council:

Carolyn R. Hodges
Vice Provost and Dean of the Graduate School

(Original signatures are on file with official student records.)

The Applications of the Tracer Particle Method to Multi-Dimensional Supernova Simulations

A Dissertation

Presented for the

Doctor of Philosophy

Degree

The University of Tennessee, Knoxville

Ching-Tsai Lee

August 2008

Acknowledgments

I would like to thank my advisors Dr. Mike Guidry, Dr. William Raphael Hix for their support and guidance. In addition I would like to thank the other members of my committee: Dr. John Quinn, Dr. Carl Sundberg, Dr. Kate Jones for their help and guidance.

I am very grateful to Dr. Stephen Bruenn for his assistance in my research work. My gratitude also goes to Dr. Cheng-Li Wu and Dr. Yang Sun for generously adding so much to my knowledge about nuclear physics.

Special thanks to all my family members for their support and encouragement.

Abstract

A new tracer particle implementation has been developed for the 2D supernova code "CHIMERA". 2D supernova simulations have been performed for a wide range of progenitors, between 10 and 25 solar mass. In the case of the Heger12 model, we have obtained a successful explosion. Analysis of the tracer particle data generated by supernova simulations reveals the aspherical geometry of the ejecta. Using the hydrodynamic trajectories provided by the tracer particles, we have performed the nucleosynthesis calculations in the post processing approximation, including the effects of neutrino captures, to understand the nucleosynthesis consequences of these models.

Contents

List of Tables

List of Figures

Chapter 1

Introduction

1.1 What is a supernova?

Stars undergoing a sudden brightening and tremendous explosion, during which their luminosity becomes comparable to that of an entire galaxy, are called supernovae (SN). Supernovae have been classified into two basic types based on spectroscopic observations: Type-I which show no hydrogen lines in their spectra and Type-II where hydrogen lines are clearly present. The further differences within these types lead to a sub-classification. Type-I supernovae are subdivided into Type-Ia, which show the marked Si II λ6355 absorption feature, blue-shifted to λ6150 in their spectra during the peak light, and Type-Ib and Ic which do not. The presence of helium lines, especially He I λ5876 in turn distinguishes Type-Ib from Type-Ic [Fil97].

From the theoretical point of view, Type-Ia SN are thought to originate from the thermonuclear explosion of dwarfs which exceed the Chandrasekhar mass ($\approx 5.85(Y_e)^2\times M_\odot, Y_e$ is the electron fraction) owing to mass transfer in a binary system. Since the luminosities of Type-Ia are almost constant, they serve as standard candles to determine extragalactic distances and to measure the basic cosmological parameters. The

supernovae that serve as the focus of this dissertation are Type-II, Ib and Ic. They result from the core collapse of massive stars.

The total energy released by a core-collapse supernova is typically $\approx 3 \times 10^{53}$erg. Most of this is in the form of neutrinos. The total light and kinetic energy of a supernova outburst is $\approx 10^{51}$erg. In addition to their prodigious light display, supernovae are the most important nucleosynthesis events. They produce or release most of the elements between oxygen and iron. They are also the most favored candidate sites for the r-process, which is responsible for the production of half the elements heavier than iron. Studies of supernovae are also important for the detection of neutrinos and gravitational waves, the birth of neutron stars and black holes, and their connection to long-duration gamma-ray bursts.

SN1987A was observed in the Large Magellanic Cloud, a satellite galaxy of our Milky Way. It was the brightest supernova observed since 1604. SN1987 was identified as a Type-II supernova whose progenitor star was a blue giant. Thanks to SN1987A, we had the opportunity to watch the time-dependent dynamics of a supernova in detail. A neutrino burst was detected a few hours before the optical detection. This is the first time humans have captured neutrinos from outside the solar system, marking the birth of extra-solar neutrino astronomy. At the moment of explosion, neutrinos are temporarily confined in the core and escape by diffusion. Since the interactions between matter and neutrinos are extremely weak, supernova neutrinos provide invaluable information from deep in the core. The detection of neutrinos in SN1987A gives us confidence in the basic ideas of the supernova mechanism, but gives little detail beyond that. The debris of SN1987A is confirmed to be globally asymmetric by the images of the Hubble Space Telescope (HST). Both the ejecta and the inner ring around SN1987A show a common axis of symmetry, potentially indicating a bi-polar explosion [Wan02]. SN1987A also provided evidence for large-scale mixing processes

which carried radioactive nuclei from the deep interior into the outer layers. The degree of asymmetry tends to increase with time which suggests the central engine is itself asymmetric.

There is growing observational evidence of non-spherical explosion. This supports recent scenarios of the supernova mechanism, which suggest that hydrodynamic instability, rotation, and magnetic fields play an important role. The best way to study the geometry a supernova's ejecta is through spectropolarimetry. Since the polarization of light scattered by electrons are completely cancelled out in the spherical case, the detection of polarization is a strong indication of deviation from spherical symmetry [Tan08]. The asymmetry is believed to have its origin in the explosion mechanism itself. Spectroparimetry has become a powerful tool to study the asymmetric nature of core-collapse supernovae in the last ten years. Leonard et al. reported the spectropolarimetric observation of SN 2004dj (Type II-P) which reveals the abrupt appearance of significant polarization when the the inner core is first exposed in the thinning ejecta (90 days after explosion) [Leo06]. Note the asphericity in SN 2004dj is cloaked by the hydrogen envelope at early times. Thus, the deeper they probe into the supernova, the greater the asphericity seemto be. They infer a departure from spherical symmetry of at least 30 precent for the inner ejecta. Combined with earlier results, Leonard et al. suggest that a non-spherical core may be a generic feature of core-collapse supernovae of all types. One of the goals of this dissertation is to examine how the asymmetric central engine impacts the nucleosynthesis of the supernova.

1.2 The mechanism of core collapse supernova

Massive stars in the course of their life cycle acquire an onion-like structure, with the hot central core surrounded by cooler outer layers of different composition. They go

through a series of burning stages, first hydrogen reacting to become helium, then helium combining to form carbon, and so on. Stars with 8-10$M_\odot$ can produce O/Ne/Mg cores. More massive stars can proceed even further. Near the end, the core consists of silicon and sulfur, and these react further to become iron. ^{56}Fe and its nuclear neighbors are the most strongly bound nuclei, so no further nuclear energy can be extracted by further fusion. The core of iron is held up by the pressure of degenerate electrons and grows as the silicon layer produces more and more iron. When the iron core's mass surpasses its Chandrasekhar limit (which is $\approx 1M_\odot$ for an interior where Ye ≈ 0.41), the pressure created by the degenerate electrons can not support it against gravity, and the core collapses. In the beginning of the collapse, when densities in the core rise above approximately 10^9g/cm^3, electrons are captured rapidly by nuclei and free protons and the resulting electron neutrinos freely escape the star. The severe energy loss by neutrinos and removal of pressure provided by electrons further decreases the pressure. Thus the collapse proceeds very fast, in less than a second. During core collapse, the density at the center increases and finally reaches nuclear density. Nuclei melt together into nuclear matter, which is incompressible. With this transition to nuclear matter, the collapse of the inner part of the iron core suddenly halts while the outer part continues infalling supersonically. The inner core rebounds and emits sound waves. The sound waves accumulate near the sonic point and become a shock wave. While propagating outwards, the shock is heavily damped by nuclear dissociations and neutrino escape. If the shock wave reaches the surface of the iron core, it can blow off the mantle to cause a "prompt explosion". There has been a debate for many years whether this prompt mechanism works. A number of numerical simulations in the early 1980's indicated that with then current equation of state (EOS), the energy is not sufficient for the prompt shock to reach the surface of the iron core. The shock stalls at a radius on the order of 100 km [Bru89]. However, recent work by Yamada and

his colleague seeks to reopen this debate, by studying the effect of the new Shen's EOS and the conventional Lattimer-Swesty EOS on the dynamics of the prompt propagation of a shock wave [Sum04]. They obtained a successful prompt explosion in the case of 11, 12, and 15 $M_\odot$ models. In the case of 13, 18 and 20 $M_\odot$ models, a shock stalls on the way. Currently it's generally believed the prompt explosion does not occur for a major fraction of progenitors, but the question remains open as further improvements are made to the EOS.

Neutrino Reheating (Delayed) Mechanism

Wilson proposed another scenario as the mechanism of an SN explosion [Bet85]. This scenario is called the "delayed explosion mechanism" or the "neutrino reheating mechanism". It assumes that the shock wave in the iron core stalls for less than one second, then gains further energy from the neutrinos, which diffuse out slowly behind the shock. Usually neutrinos interact with matter weakly. But in the extremely dense conditions of the collapsed core, they couple to matter more strongly. They heat the layer above the inner core of a supernova mainly by charged-current electron neutrino and antineutrino absorption on protons and neutrons, raising the pressure behind the stalled shock wave. The rejuvinated shock wave is then able to reach the envelope with sufficient energy to eject the envelope explosively. Neutrino-driven convection behind the shock and stationary accretion shock instability (SASI) play a supportive role in the neutrino reheating mechanism [Blo03]. Neutrino-driven convection may increase the efficiency of neutrino energy deposition behind the shock to power an explosion. SASI leads to violent bipolar sloshing motions of the shock. This drives the shock front to large radii and thus reduces the accretion velocities. SASI also causes the quasi-periodic expansion and contraction phases of the shock and thus leads to secondary

convection. Due to the effects of SASI, gas accreted through the stalled shock can stay longer in the heating layer and absorb more energy from the neutrino flux. In addition to aiding the explosion, SASI may be the cause of large pulsar kicks and global asymmetry observed in supernovae like SN1987A [Blo07]. At present the neutrino reheating mechanism is the most popular mechanism.

Alternate Mechanisms

It is generally accepted that rotation and magnetic fields could also play significant roles in the supernova explosion. The Magnetorotational Mechanism was first suggested by Bisnovatyi-Kogan in 1970 [Kog70]. The pre-supernova core is known to be rotating and to possess some magnetic field. Magnetic fields can be amplified due to differential rotation during the core collapse. If the magnetic pressure is high enough, a compression wave starts to move outwards and transforms quickly into a fast MHD shock [Moi07]. As a result, part of the rotational energy of the presupernova star is transformed into kinetic energy. The magnetorotational mechanism is experiencing a comeback mainly for two reasons. Firstly, some fraction of long-soft gamma-ray bursts are accompanied by very energetic and highly asymmetric supernovae. The progenitor stars of these supernovae are thought to be rapidly rotating massive stars, making them excellent candidates for this mechanism. Secondly, there has been accumulating evidence that many supernovae are highly asymmetric. The spectra of some supernovae (e.g., SN87A, SN1993J, SN1994I, SN1999em) are significantly polarized indicating asymmetric envelopes with axis ratios up to 2 [Hof04]. The orientation of the polarization vector tends to stay constant in time. This implies that there is a global symmetry axis in the ejecta.

It's well known that many of the massive stars are rapid rotators on the main sequence [Tas78]. However, it's controversial if the iron cores have much angular momentum before the gravitational collapse. Akiyama et al. suggested that the magnetorotational instability (MRI) could be an important factor in the supernova explosion [Aki03]. With sufficient differential rotation, MRI leads to the exponential growth of poloidal and toroidal components of the magnetic field and transfers angular momentum. If there is a suitable combination of rapid rotation and strong magnetic field, two opposing supersonic jets can form and a jet-like explosion is induced [Yam04].

Progenitors of most core-collapse supernovae lie in the mass range 8-20$M_{\odot}$. Heavier stars usually lose their hydrogen envelopes and much of their outer-core mass before they finally experience core collapse producing type Ic supernovae. Some are likely to be accompanied by gammy-ray bursts. In the collapsar scenario proposed by Woosley [Mac99], a massive Wolf-Rayet star with a rapidly rotating iron core may collapse to form a black hole. Part of the infalling matter forms a disk around the black hole. The disk acts as an efficient engine to extract gravitational energy and power strong polar jets. Gamma-ray bursts are expected to be driven by such jets. Rotation and magnetic fields may also be important to the neutrino reheating mechanism. Rotation alone can induce asymmetric neutrino fluxes. Rotation will lead to magnetic field amplification thus producing MHD effects, and affect neutrino transport [And03].

Recently, Burrows et al. suggested that supernovae might be energized by acoustic power originating from g-mode oscillations of the accreting proto-neutron star [Bur06]. SASI plays an important role in the acoustic mechanism. The vigorous stirring and turbulence generated by the SASI sets the stage for the excitation of the oscillations. The large-amplitude core motions create powerful sonic activity by which energy is transported to the shock. However, the acoustic mechanism requires a significant delay of the explosion. If another mechanism, such as the neutrino reheating mechanism,

succeeds earlier, the acoustic mechanism will be aborted. In their 2D simulation, Burrows et al found that if the delay to explosion is long, perhaps 0.5 to 1.0 seconds, the inner core can be excited to oscillate in g-mode which damps by the anisotropic emission of sound. At this late stage, acoustic power can rival or exceed neutrino deposition power and explode the envelope. According to the acoustic mechanism, large progenitor stars have more accretion onto the proto-neutron star, producing larger core oscillations, and a much stronger gravitational wave [Bur06]. As a result, the detection of the gravitational wave may help to ascertain the acoustic mechanism.

The explosion mechanism for core-collapse supernovae has been a long standing problem despite continuous efforts for decades. We know the general picture of core-collapse supernovae: the explosion energy is provided by gravitational potential energy during the collapse. But the mechanism of transporting energy to outer layers is still controversial. We have to wait for realistic 3D simulations before we can say anything conclusive. It is ultimately observations that will tell us which is the proper mechanism. Many of these observations depend on the nuclear composition of the ejecta. Thus nucleosynthetic studies like that at the heart of this dissertation help to shed light on the true mechanism.

1.3 Recent developments in core-collapse supernova simulations

Supernovae are dramatic events including a rich diversity of physics from the fields of particle physics, nuclear physics, fluid dynamics and general relativity. All four forces of nature are involved in these extreme events. The complexity of supernovae precludes a purely analytic investigation. Therefore, numerical simulations together with observations are the best approach to study supernovae. Simulations of a variety

of suggested SN mechanisms performed thus far have shown that (1) neutrino heating, (2) convection, (3) rotation, (4) magnetic fields, together with proper treatments of (5) the nuclear equation of state, (6) nuclear burning, and (7) gravity, and more recently (8) standing shock instability and (9) g-mode oscillation of the proton-neutron star will be important to understanding the central engine of the explosion [Mez04]. Ultimately simulations must include all the effects mentioned above.

Since the discovery of the SN1987, more and more evidence shows that supernovae are not spherical. The evidence includes the observed high polarization, pulsar kicks, high velocities of iron-group and intermediate-mass elements, and direct observations of the debris in remnants. The violations of spherical symmetry may result from rotation, magnetic fields, and various kinds of hydrodynamic instabilities. Presently, it is recognized that spherically symmetric simulations with the current input physics do not yield realistic explosions. To accurately investigate multi-dimensional effects such as convection, rotation, and magnetic fields, future simulations must be carried out in two and ultimately three dimensions and must implement realistic, multi-dimensional, multi-group neutrino transport [Jan04].

Even after forty years of intense research, the numerical simulation of core collapse supernova still pose one of the most fascinating and challenging problems in astrophysics. Numerical simulations have often had trouble reproducing the explosions. As recently as five years ago, Janka et al. suggested that some important physics is missing in supernova models because the explosions were not obtained in 1D and 2D models with state of art input nuclear and weak interaction physics and Boltzmann neutrino transport [Bur03]. However, we have seen significant progress in numerical modeling of supernovae in the last several years. With the improvement of neutrino interactions and the inclusion of nuclear burning, the ORNL group has produced explosions successfully in simulations of both 11 and 15 $M_{\odot}$ progenitors [Bru07]. They have

discovered that the shock is not revived in the iron core but in the oxygen-rich layer, at much later time than previously anticipated. SASI causes large-scale distortions of the shock. As a result, the shock reaches the oxygen layer sooner in certain directions. The energy released by the nuclear burning of the shock-heated oxygen-rich material and the neutrino energy deposition together with the reduced ram pressure leads to a revival of the shock and an explosion.

Similar results are now being obtained by the Garching group. Janka et al. obtained neutrino-driven explosions for stars in the 8-10$M_\odot$ range with O/Ne/Mg cores. For more massive stars (11 and 15$M_\odot$), they found the explosion occurs later than previously thought, and is crucially supported by SASI [Jan07]. On the contrary, Burrows et al. did not see neutrino-driven explosion in their 2D simulations. They claimed that SASI does not lead to explosion itself, but creates an anisotropic accretion stream onto the core that excites the core g-mode oscillations. The sound waves radiated by the neutron star may contribute to the shock revival. With the aid of acoustic power, Burrows et al. obtained explosions for progenitors with wide mass range from 11-25$M_\odot$, at very late times [Bur06]. However, Marek et al. show the amplitude of core oscillations is very small and the acoustic energy flux injected by the neutron star is minuscule compared to the neutrino energy deposition [Mar07].

Most supernova simulations so far are done in one or two dimensions. The real world is 3D. To reduce the 3D problem to the 2D or 1D problem, one needs to introduce artificial symmetries which pose severe limitation of the flow motion. Therefore, it's not surprising that the result of 1D simulations is quite different from that of 2D simulations. However, there is cause to wonder if 3D will look like 2D. Recently Blondin et al. have performed a series of hydro-only simulations of a steady accretion shock on a three-dimensional Cartesian grid [Blo07]. They found the supernova shock wave is unstable and leads to a non-axisymmetric spiral flow pattern. They also found

the spiral flow pattern had resulted in the deposition of angular momentum onto the forming neutron star. The neutron star spin could not have been obtained in 2D models, where the imposition of axisymmetry reduces the number of degrees of freedom. Their 3D results demonstrate how different the outcomes in 2D and 3D simulations may be. Therefore, it's very desirable to perform supernova simulations in 3D.

To date, very few supernovae simulations using more accurate multi-group neutrino transport have been performed in 2D, much less in 3D, because of the limitations of the computing hardware. Since the real world is 3D, the assumption of spherical symmetry or axial symmetry may prevent certain multidimensional effects to occur. The pioneering 3D supernova simulations have been performed by Fryer et al [Fry02]. They found that convection arising in 3D collapse shows a remarkable resemblance to 2D simulations. Thus the explosion energy, explosion timescale and remnant mass does not differ greatly between 2D and 3D simulations. However, their result is far from conclusive. They use a gray flux-limited scheme to transport the neutrinos which may overestimate the total energy deposition by neutrinos. This leads to a too rapid re-energizing of the shock, not allowing the SASI time to develop. 2D simulations with multigroup transport exhibit a much longer delay in the shock's redevelopment than seen in Fryer's simulations. Thanks to the rapid development of supercomputer and parallel computing, the 3D multi-group supernova simulations will be performed in the near future when the Petascale computing is available.

Chapter 2

Supernova nucleosynthesis

2.1 Introduction to supernova nucleosynthesis

Core collapse supernova nucleosynthesis is a topic of great relevance to our search for our cosmic origins, because supernovae play such a dominant role in the production of many heavy elements and because these products are readily observable. During the explosion, the material is heated by the passage of the shock wave. Therefore, explosive nuclear reactions are induced in a short period, and can include reactions with tremendous flux of neutrinos that are powering the explosion. Nucleosynthetic products observed in an individual supernova or supernova remnant can provide information about the explosion mechanism and explosion energy. Their spatial distribution can reveal anisotropies and mixing. The comparison of integral yields of supernova nucleosynthesis accross the range of SN progenitors with galactic or solar abundances can also shed light on the explosion mechanism. It is commonly accepted that multi-dimensional hydrodynamical calculations are necessary for the successful supernova simulations, though even multi-D models have problems describing the explosion mechanism since they currently do not all show explosions. Due to limitations in both computer power

and numerical approaches, it has not yet been possible to couple full reaction networks, including all nuclei produced in the supernova explosion, to multi-D hydrodynamical solvers. When focusing on nucleosynthesis, one traditionally resorts to a number of approximations: instead of multi-D, the simulation is reduced to one spatial dimension; two reaction networks are used, a smaller one which provides the nuclear energy generation and is directly coupled to the hydrodynamical solver and a larger one without feed-back to the hydrodynamical solver following all the nucleosynthesis; multi-D effects such as convection and mixing are ignored or treated via mixing-length approximations [Rau04]. The failure of self-consistent models for core collapse supernovae to produce explosions has also generally forced the modeling of core collapse supernova nucleosynthesis to rely on parameterized models. There are two common ways to simulate the explosion artificially. One is by means of a "thermal bomb", injecting thermal energy inside the iron core, in sufficient quantity that the ejecta attains the desired kinetic energy, roughly 10^{51} erg [Thi96]. Another alternative is the injection of momentum, through a "piston", outward-moving during the explosion, with a velocity such that the desired kinetic energy of ejecta is obtained [Woo95]. The comparison of the nucleosynthetic yeilds between these two approaches has been done by Young et al [You07]. Neither approach truly mirrors the neutrino driven explosion process nor accounts for the detailed neutrino interactions. Artificial induced explosions for supernova nucleosynthesis predictions may be a valid approach for the outer layers, but are inconsistent for the innermost layers, affecting the Fe-group composition [Auf91].

Only recently, has it become feasible to study the explosive nucleosynthesis using limited nuclear networks coupled to multi-D supernova models as is done in the work of Kifonide, et al. and in CHIMERA. The main advantages of Kifonids' approach are that they drive the shock by neutrino-matter interactions in the layers outside the protoneutron star, using an adjustable neutrino "lightbulb" instead of a "thermal

bomb" or a "piston". Thus the impact of the neutrinos has been better considered [Kif03]. The results of [Kif03] show large differences in the final maximum nickel velocities between their type-II and type-Ib models. In the type-Ib model the maximum velocities of metals remain frozen in at about 3500-5500 km/s, for t = 300s, while in the type-II model they drop significantly for t > 1500s due to the massive hydrogen envelope which forces the supernova shock to slow down strongly. The type-Ib model is in fair agreement with observed clump velocities and the amount of mixing. However maximum velocities of iron-group elements like those seen in SN 1987A cannot be reproduced in case of the 15 solar-mass progenitor considered.

Neutrino interactions play an important role not only on supernova mechanism but also on supernova nucleosynthesis. Recent supernova simulations with accurate neutrino transport show the presence of proton-rich region in the inner ejecta and the early neutrino wind from the proton-neutron star. Very recently Frohlich et al. and Pruet et al. studied the nucleosynthesis in the innermost layers of core-collapse supernova [Pru05, Fro06a]. The dominant quantity to describe nucleosynthesis correctly in the innermost ejecta is Y_e. It can be altered by neutrino-induced weak interactions as well as electron or positron captures. Frohlich et al show that Y_e in the innermost ejected layers is close to 0.5, in some areas even exceeding 0.5. This improves agreement with the abundance constraints from galactic evolution and solar abundances. Both of their works found improvements within the Fe-group. The strong overproduction of neutron-rich nuclei in the vicinity of the N=50 closed shell in previous neutron-rich environments is reduced. ^{45}Si and ^{49}Ti are enhanced to permit predictions closer to solar proportions. Frohlich et al. suggest antineutrinos streaming in huge numbers from the neutron star could irradiate the protons and turn some into neutrons [Fro06b]. This so-called νp-process could explain the surprisingly large number of certain heavy

elements, such as strontium, seen in otherwise metal-poor stars. These recent investigations have demonstrated that multi-dimensional effects and neutrino interactions are important in determining the spatial distribution and composition of the iron-rich ejecta from SN. In the following sections we will present our plan to extend the current state of art of nucleosynthesis calculations and examine both of these effects.

2.2 Nuclear reaction network

Nucleosynthesis refers to those processes by which atomic nuclei are transformed on the cosmic scale. It involves the study of how primordial matter is processed into the abundances observed in astronomical objects (the solar system, stars, interstellar gas and so on). The energy generation and nucleosynthesis at various astrophysical sites can be calculated by nuclear reaction networks.

A nuclear reaction network contains a system of differential equations in time for the nuclear abundances of the form:

$$\dot{Y}_i = \sum_j \mathcal{N}^i_j \lambda_j Y_j + \sum_{j,k} \mathcal{N}^i_{j,k} \rho N_A \langle j,k \rangle Y_j Y_k + \sum_{j,k,l} \mathcal{N}^i_{j,k,l} \rho^2 N_A^2 \langle j,k,l \rangle Y_j Y_k Y_l. \qquad (2.1)$$

We introduce the nuclear abundance $Y_i = n_i/\rho N_A$, where n_i is the number density, ρ is the mass density, N_A is Avagadro's number. The $\mathcal{N}$ s provide for proper accounting of numbers of nuclei and are given by: $\mathcal{N}^i_j = N_i$, $\mathcal{N}^i_{j,k} = N_i/\prod_{m=1}^{n_{j,k}} |N_m|!$, and $\mathcal{N}^i_{j,k,l} = N_i/\prod_{m=1}^{n_{j,k,l}} |N_m|!$. The $N_i's$ can be positive or negative numbers that specify how many particles of species i are created or destroyed in a reaction, while the denominators, including factorials, run over the $n_{j,k}$ or $n_{j,k,l}$ different species destroyed in the reaction and avoid double counting of the number of reactions when identical particles react

with each other. The first term of Eq. (2.1) describes changes of due to the reactions involving a single nucleus, which include decays, electron captures, photodisintegrations and so on. λ_j is the one particle interaction rate. The second and third term describe changes due to two and three-body reactions, respectively [Hix06]. For a set of nuclear abundances $\vec{Y}$, one can calculate the time derivatives of the abundances, $\dot{\vec{Y}}$ using Eq. (2.1). The desired solution is the abundance at a future time, $\vec{Y}(t+\Delta t)$, where Δt is the network timestep. For simplicity, most past and present nucleosynthesis calculations use the simple finite difference prescription:

$$\frac{\vec{Y}(t+\Delta t)-\vec{Y}(t)}{\Delta t} = (1-\Theta)\dot{\vec{Y}}(t+\Delta t) + \Theta\dot{\vec{Y}}(t). \tag{2.2}$$

For the stiff set of non-linear differential equations which form most nuclear reaction networks, a fully implicit treatment is generally most successful [Arn69]. Solving the fully implicit version of Eq. (2.2) is equivalent to finding the zeros of the set of equations

$$\vec{\mathcal{Z}}(t+\Delta t) \equiv \frac{\vec{Y}(t+\Delta t)-\vec{Y}(t)}{\Delta t} - \dot{\vec{Y}}(t+\Delta t) = 0. \tag{2.3}$$

This is done using the Newton-Raphson method, which is based on the Taylor series expansion of $\vec{\mathcal{Z}}(t+\Delta t)$, with the trial change in abundances given by

$$\Delta\vec{Y} = \left(\frac{\partial\vec{\mathcal{Z}}(t+\Delta t)}{\partial\vec{Y}(t+\Delta t)}\right)^{-1}\vec{\mathcal{Z}}\ , \tag{2.4}$$

where $\partial\vec{\mathcal{Z}}/\partial\vec{Y}$ is the Jacobian of $\vec{\mathcal{Z}}$.

At conditions of high temperature and density, thermonuclear reaction rates may be sufficiently rapid to achieve nuclear statistical equilibrium (NSE). This permits considerate simplification of the calculation of the nuclear abundances, where the temperature exceeds 5.5 GK. For regions in NSE, CHIMERA uses LSEOS where the density exceeds

1.7×10^8 g/cm^3 and Cooperstein EOS [Bar85] where the density is less than 1.7×10^8 g/cm^3. For regions not in NSE, CHIMERA turns on the Xnet nuclear reaction network to evolve the nuclear composition. The Cooperstein EOS which contains an ideal gas of nucleons and nuclei is used.

Chapter 3

The relevant physics for supernova studies and the physics inputs to the CHIMERA code

3.1 Weak interaction processes

The weak interaction is the most universal interaction after gravitation. All fermions participate in the weak interaction. The weak interaction can alter the charge of fermions and their flavours. Charge alteration corresponds to the fact that the field quanta, the W bosons, carry charges. There are also processes in which the fermion charge is not altered. Such processes are covered by the term "neutral currents". Weak interaction processes like electron capture are of fundamental importance in a core collapse supernova. During presupernova evolution, the core is supported by degenerate electron pressure. Because of a combination of photodisintegration and electron capture, a dynamical instability develops and the core collapses. In addition, neutrino interactions with shock-heated nucleons are the major source of the neutrino

heating which revives the shock wave. The weak interactions also largely determine the mass of the iron core, and thus affect the strength and evolution of the shock wave.

Calculation of the rate of weak interactions like electron capture and beta decay requires knowledge of the nuclear structure. Fuller, Fowler and Newman (FFN) did their pioneering calculations of stellar weak interaction rates for nuclei in the mass range A=45∼60 based on the independent particle model [Ful82]. They recognized the important role played by Gamow-Teller transitions. In the independent particle picture, GT transitions can only proceed in the same harmonic oscillator shell. Consequently, for nuclei with charge number Z $<$ 40 and N $>$ 40, GT transitions are completely blocked due to the Pauli principle. Hence it has been assumed for many years that electron captures during the collapse phase occur predominantly on free protons rather than on nuclei. However, recent calculations based on the nuclear shell model show the Pauli blocking of the GT transition is overcome by correlations and thermal effects. Langanke et al. found that electron capture on nuclei dominate over capture on free protons during the collapse phase [Lan03]. The effects of this more realistic implementation of electron capture on various heavy nuclei have been evaluated in supernova simulations by the Oak Ridge group. Despite the quantitative change of the electron capture rates and hence the lepton fraction, there is little change for the shock propagations in 1D models [Hix03].

As the collapse proceeds, matter gets denser and the outflowing neutrinos interact with matter strongly, mainly via scattering by electrons, nucleons and nuclei. If the weak interaction involves neutral currents, as many experiments have suggested since 1974, then neutrinos can be coherently scattered by nuclei with enhanced cross section with an A^2 independence where A is the atomic number. The neutral elastic scattering of neutrinos with nuclei and electrons is responsible for neutrino trapping during collapse. The inelastic neutrino scatterings with nuclei can also contribute to

neutrino opacity and promote nuclei to excited states [Her94], although they are not included in most of the simulations. Based on the shell model for Gamow-Teller transitions and the Random Phase Approximation for forbidden transitions, Langanke et al have calculated reaction rates of inelastic neutrino scatterings under supernova conditions [Lan08]. They incorporated the rates into supernovae simulations with detailed multi-group neutrino transport. They found inelastic neutrino-nucleus scattering increases the neutrino opacities noticeably for high energy neutrinos and strongly reduces the high-energy tail of the neutrino spectrum emitted in the neutrino burst at shock breakout, although no significant effect on the SN dynamics is observed.

Weak interaction rates at low energies have been calculated by shell model or random phase approximation (RPA). In principle, the shell model can provide wave functions of nuclear ground states and excited states. But the shell model is not applicable to heavy-mass nuclei due to the necessarily huge model spaces. For those nuclei (A > 50-65), the complete fpgds shells are required to describe the mixing due to nuclear correlations and finite temperature effects. Currently this is only possible by means of the shell model Monte Carlo approach (SMMC). Another judicious scheme is the Projected Shell Model (PSM). The PSM adopts a deformed basis in which important nuclear correlations can be taken into account very efficiently. Therefore the diagonalization in the PSM can be carried out in a smaller space for medium or heavy nuclei. Recently, Gao et al calculated Gamow-Teller transition rates by PSM [Gao06]. Their results show the PSM may be a powerful tool to calculate beta decay or electron capture rates for the core-collapse supernova modeling.

The effects of weak interaction processes on supernova nucleosynthesis are threefold [Hix03]. First, in the inner layers of the ejecta, neutrinos interact with the iron group nuclei which result from alpha-rich freezeout thus change the composition. Second, neutrino process (ν process) occurs in the outer layers followed by shock heating.

Third, the neutrino proton (νp) process may occur in the early phase of the neutrino driven wind and may be followed by the r-process.

3.2 Neutrino transport

Neutrinos play a key role at every stage of core collapse supernova explosions. They take away $\approx 99\%$ of the neutron star's gravitational binding energy. It is currently thought that neutrino heating of the proto-neutron star mantle drives the supernova explosion.

At the time the shock stalls, the core consists of an inner "neutrino sphere" radiating neutrinos and antineutrinos of all three favors : electron, muon, and tau. This inner core will ultimately radiate away its thermal energy, cool, and go on to form a neutron star or a black hole. Revival of the stalled shock wave above the neutrino sphere is mediated primarily by the absorption of electron neutrinos and antineutrinos emerging from the radiating proto-neutron star. This heating depends sensitively on the neutrino luminosities, spectra, and angular distributions in the region behind the shock, ultimately necessitating multigroup Boltzmann neutrino transport [Mez99]. The term multigroup means that the transport is carried out for multiple neutrino energies separately. Since the neutrino interactions are energy dependent, neutrinos with different energies may behave very differently. Moreover, in the semitransparent region around the neutrinosphere, neutrino transport is neither diffusive nor free steaming. Thus only Boltzmann neutrino transport can capture the neutrino quantities with sufficient accuracy.

A solution to the Boltzmann equation describes the time evolution of the neutrino distribution function, which gives the number of neutrinos at a given spatial location with a given direction cosine and energy. Solving the Bolzmann equation is highly

computationally extensive, even in one dimension simulations that assume spherical symmetry. Historically a number of approximations have been implemented. Prior to the advent of full Boltzmann neutrino transport in 2000, simulations had implemented approximate treatments of neutrino transport, from simple "leakage schemes", to "two-fluid" approaches, and ultimately "multigroup flux-limited diffusion". MGFLD accurately describes the radiation field at high optical depth where the diffusion approximation is exact. In the free-streaming limit, the flux must be limited to maintain causality and an interpolation must be performed between diffusion and free-streaming regimes by an ad-hoc prescription (using a flux limiter) [Ott08].

Exact Boltzmann neutrino transport has only recently been applied in spherical core collapse simulations with Newtonian gravity [Mez01], approximate treatment of relativistic effects [Ram02], and general relativity [Lie01]. All of them have failed to produce explosion. We can conclude that accurate neutrino transport alone does not overcome the failure of supernova simulations that assume spherical symmetry to produce explosions. Moreover, there were suggestions that the success of multi-dimensional simulations might disappear once the neutrino transport is improved to the sophistication reached in one dimension model [Bur03].

Efforts to develop full multi-D Boltzmann transport are underway, but it is very computationally expensive. To compromise, a ray-by-ray-plus approximation was implemented in the CHIMERA code. In the ray-by-ray-plus approximation, the lateral effects of neutrinos such as lateral pressure gradients, neutrino advections, and velocity corrections are taken into account, but full transport is performed only in the radial direction. This radial transport is computed by means of multigroup flux-limited diffusion with a flux limiter that has been tuned to reproduce full Boltzmann transport results to within a few percent [Lie05].

3.3 Nuclear equation of state and nuclear composition

The equations of inviscid fluid dynamics consist of three equations describing the conservation of momentum, mass, and energy. The dependent variables are d, e, p, and $\vec{v}$ which denote the mass density, specific internal energy, pressure and fluid velocity respectively. The equations of inviscid dynamics represent five equations containing six unknowns. An equation of state, which represents the sixth equation, is necessary to complete the formulation.

An equation of state (EOS) is a relationship between various thermodynamic variables characterizing a medium. The equation of state (EOS) of strongly interacting matter at high densities plays an important role in the mechanism of core collapse supernova explosions. It affects the core bounce, the propagation of the shock wave, and the formation of the proto-neutron star. The collapse of the core is halted when the nuclear potential becomes repulsive, causing the core to rebound, launching a bounce shock. The size of the inner core and the initial shock energy depend sensitively on the stiffness of the equation of state. A softer EOS gives a more compact core and a larger inner core at bounce. This in turn leads to a larger initial shock energy and a smaller outer core through which the shock wave must propagate. The dependence of the supernova explosion on the softness of EOS has been studied by changing the incompressibility of nuclear matter [Swe94]. Smaller incompressibility is indeed found to be preferable. The composition of dense matter is another important factor toward the success of the explosion. The abundances of protons, neutrons, alpha particles and nuclei determine the reaction rates of electron captures, neutrino scatterings and others.

Although study of dense matter for supernova research has a long history, there are only a few studies which cover the wide range of density, electron fraction and temperature in the supernova environment. Direct numerical calculation of the EOS is extremely complicated and time consuming, so it is unsuitable for incorporation into a hydrodynamic simulation. Tabular equations of state have often been used in supernova simulations. They must cover the wide range of density, composition, and temperature. The most widely-used equations of state are :

(1)The standard EOS (Lattimer and Swesty) [Lat91], which is based on a compressible liquid drop model and employs a skyrme force for the nucleon interaction. It includes baryon, lepton and photo contributions.

(2)A new relativistic mean field EOS [She98], which is based on the relativistic mean-field (RMF) theory with a Thomas-Fermi approach. It includes only nuclear contributions.

(3)The Wilson EOS [May91], which is based on the empirical relation of Coorperstin EOS [Bar85], constrained by relativistic Brueckner-Hartree-Fock calculations of [Mut87]. It is a tabular complete EOS which includes baryon, lepton, photon, and Pions.

In the currently available sets of equation of state for supernova simulations such as the Lattimer-Swesty EOS and the Shen-EOS, dense matter is described as a mixture of neutrons, protons, alpha particles, and the representative species of nuclei.

CHIMERA uses the equation of state (EOS) of Lattimer and Swesty (1991) for regions in NSE where the density exceeds 1.7×10^8 g/cm^3. The LS EOS assumes

NSE between of free neutrons, free protons, alpha-particles and a representative or average heavy nucleus. A highly modified version of Cooperstein EOS is employed in CHIMERA for regions in NSE but the density is lower than 1.7×10^8 g/cm^3 and regions in non NSE. CHIMERA use Xnet to calculate the temporal evolution of the abundances of nuclear speices. Xnet is a thermonuclear reaction network which use the fully implicit Backward Euler scheme. Currently Xnet in CHIMERA only contain 14 elements. While this 14 element reaction network provides a reasonable estimate of nuclear energy generation in supernova simulations, it is insufficient to calculate the detailed supernova nucleosynthesis. Detailed nucleosynthesis requires evolving more than 150 nuclear isotopes. Currently this is prohibitive due to the large execution time for a large network. To explore the detailed nucleosynthesis with the CHIMERA code, we adopt a post-processing approach. We assume that nucleosynthesis occurs uniformly in each Lagrangian zone which is characterized by a tracer particle, nucleosynthesis calculations are done by using a large nuclear reaction network after the supernova simulations. Recently, tabulated cross sections for electron andanti-electron neutrinos have been installed in Xnet. Thus we are able to study neutrino nucleosynthesis in supernovae.

Chapter 4

Tracer particle methods

4.1 Motivation

Two main purposes of utilizing tracer particles are (1) to provide a Lagrangian view of the explosion, and (2) to provide the data which is necessary to do the post processing nucleosynthesis calculations.

There are two basic schemes for simulating hydrodynamic motion: the Lagrangian scheme (where the grid moves with the material) and the Eulerian scheme (where the grid is fixed in the space). The Lagrangian scheme has the advantage that it naturally yields the necessary data for the nuclear reaction calculations, since it directly follows the evolution of specific fluid elements. Unfortunately the Lagrangian scheme is very difficult to apply for multi-dimensional simulations because it can lead to severe grid distortions and tangles. The Eulerian scheme does not have the same problem since the Eulerian grids are fixed in space and with time. Therefore the Eulerian scheme has been preferred for the multi-dimensional simulations. However, there is a disadvantage associated with the Eulerian scheme: we don't know the history of field variables for a given parcel of material. In order to obtain the Lagrangian evolution of the physical

quantities for the post-processing nuclear network calculations, we apply "the tracer particle method". We add a Lagrangian component to the Eulerian scheme in the form of tracer particles that move with the flow in the course of the Eulerian calculation, recording their temperature and density history by interpolating the corresponding quantities from the underlying Eulerian grid. The tracer particle method (also called test particle method) has been applied to post-processing nucleosynthesis calculations in core-collapse supernovae [Nag98], Type Ia supernovae [Tra04], also hypernova, and Gamma-ray bursts [Nag06]. The tracer particle method has also been used to study the mixing of the core-collapse supernova [Nag99] and the turbulent mixing in the interstellar medium [Fed08].

4.2 Algorithm

We assume the tracer particles move with the local velocities which are given by the hydrodynamic calculations. Therefore we can calculate the particles' path by a number of numerical integration methods. Here we will examine the simple Euler method and the predictor-corrector method. The simple Euler method is the simplest and most common way to integrate the equations of motion numerically. It assumes the velocities are constant through the time interval dt. Thus the particles move according the formula:

$$X_{n+1} = X_n + V_n(X_n) * dt \tag{4.1}$$

The predicted-corrector method can be described as follows: initially particle velocities $V_n(X_n)$ are obtained by interpolation at the position of each particle, and a predicted position after half a time step is calculated from the velocities:

$$X_{n+1/2} = X_n + V_n(X_n) * dt/2 \tag{4.2}$$

Then we can calculate the particle velocities $V_n(X_{n+1/2})$ at the predicted midtime step positions. After evolution of the hydrodynamics, again we update the particle position. The particles move according to the average of the velocities at the same predicted position but at different times:

$$X_{(n+1)} = X_n + (dt/2) \times (V_{n+1}(X_{n+1/2}) + V_n(X_{n+1/2})) \tag{4.3}$$

With the information of the tracer particle's path, the physical quantities of the particles such as the density and temperature at each time are determined by interpolation from the Eulerian grids.

The interpolation method should be consistent with the numerical method to minimize introducing systematic error. In the case of a finite-volume method, the computational domain is discretized into a finite number of cells. The mesh quantities have cell-averaged values rather than point values, which requires the interpolation function also represent cell-averaged values. Cell averaged quantities are defined as follows:

$$f_i(x) \equiv 1/\Delta \times \int_{i-1/2}^{i+1/2} f(x^{'})dx^{'} \tag{4.4}$$

where i is the zone index. In the piecewise parabolic method, as is used for the hydrodynamic component in the CHIMERA code, a second-order interpolation function is in the form of:

$$f(x) = A + B \times (x - x_i) + C \times (x - x_i)^2 \tag{4.5}$$

Integrating Eq.(4.4) with the function Eq.(4.5) over the nearest cells gives A, B, and C. Using the same procedure as above, it's easy to extend to the multi-dimensional and curvilinear coordinates. We have derived interpolations in one, two, and three

dimensions with cartesian, cylindrical and spherical geometries. To do the 2D simulations, we can use a polar grid spanning the entire equatorial plane (ϕ varies from 0 to 2π) or a spherical-polar grid stretching from one pole to the other (θ varies from 0 to π). Note the interpolation functions for a polar grid (ϕ) are quite different from that of a spherical-polar (θ) grid. We do not assume the Eulerian grids are uniform in the above procedure, so the interpolation functions obtained can be used for uniform, nonuniform and even adaptive grids.

4.3 Implementation

We have implemented the numerical algorithms described in the previous section into the hydrodynamic code VH-1. VH-1 was written and tested by the Virginia Numerical Astrophysics Group, and is based on the piecewise parabolic method (PPM) which is a higher order Godunov method developed by Colella and Woodward. PPM is particularly well suited for following discontinuities in the flow like shocks. VH-1 is the basis for the hydrodynamics modules in the supernova code "CHIMERA" (see Chapter 5). The tracer particle module contains several subroutines. A short description of these subroutines are shown in Table 4.1. The tracer particle module extracts pressure, density, and velocities from VH1 code (see Table 4.2). The particle variables are listed in Table 4.3.

We have developed a MPI edition of the tracer particle code. Message Passing Interface (MPI) is the most widely used parallel computing tool. It is not a new programming language; rather it is a message passing library standard. It was developed by an open, international forum consisting of representatives from industry, academic and government laboratories. The advantages of MPI are portability, efficiency and flexibility. MPICH is an open source implementation of MPI. The goals of MPICH are

Table 4.1: Description of the particle subroutines

Subroutine name	Description
particle_step	evolve the tracer particles and calculate the particle quantities
cartesian1d(x) cartesian2d(xy) cartesian3d(xyz) cylindrical1d(r) cylindrical2d(rz) cylindrical3d(rzϕ) spherical1d(r) spherical1d(θ) spherical1d(ϕ) spherical2d(rθ) spherical2d(rϕ) spherical3d(r$\theta\phi$)	interpolating functions for different geometries
particle_output	subroutine for output

Table 4.2: Hydro variables used in tracer particle module

Hydro variables	Description
zpr	pressure
zro	density
zux	x velocity
zuy	y velocity
zuz	z velocity

Table 4.3: Particle variables and corresponding description

Particle variables	Description
px	particle positions in the x direction
py	particle positions in the y direction
pz	particle positions in the z direction
pzpr	pressures of the particles
pzro	densities of the particles
pzux	x velocities of the particles
pzuy	y velocities of the particles
pzuz	z velocities of the particles

provide an MPI implementation for various platforms, including clusters, SMPs, and massively parallel processors.

The Enhanced Virginia Hydrodynamics 1 (EVH1) is a parallel version of VH1 developed jointly by NCSU and ORNL. EVH1 uses 2nd order operator splitting and 1D Lagrangian hydrodynamics in each coordinate direction. The parallelization is base on domain decomposition into stripes: every processor is responsible for a domain in real space. Directional splitting is implemented with an explicit MPI All-to-All to restructure domain decomposition.

When doing parallel computing of tracer particles one has to divide particles over processors. There are two basic methods to do that: domain decomposition and particle decomposition. We have chosen the domain decomposition method. Thus the tracer particles are assigned to different processors according to their positions. If the distribution of the particles is not homogeneous in space, the amount of computation porformed by each processor is not equal. In other words, we can not keep the load balanced. This is the possible drawback of using domain decomposition with particles. Using particle decomposition can guarantee the load balance. However, we can not adopt particle decomposition because we need local hydrodynamic data to calculate the particle data. In EVH1, hydrodynamic sweeps are made along each direction. Then a hydrodynamic data transpose is performed to switch the sweep to the other direction by using All-to-All collective communication. The tracer particle module is called after each hydrodynamic sweep. All the particle message passing between different processors is done by collective All-to-All communication as in EVH1 itself, avoiding complicated point-to-point communication. We have implemented a MPI edition of the tracer particle code into both the EVH1 and the CHIMERA code (see Chapter 5.2).

4.4 Verification tests

The verification tests are done by using our tracer particle code together with the hydrodynamic code VH-1. Since VH-1 uses a Lagrangian-Remap approach, we can run it by Lagrangian or Eulerian scheme in 1D. We will compare the results of the Eulerian scheme + tracer particle method to those of the Lagrangian scheme.

The first test problem chosen is the Sod shock tube problem. It has become a standard test problem in numerical hydrodynamics. The initial conditions are very simple. In the standard case, the density and pressure on the left are equal to 1, and the density on the right side of the contact is 0.125 and the pressure is 0.1. As the evolution begins, a shock propagates to the right while a rarefaction wave travels to the left. The tube (domain) extends from x=0 to x=1 for Cartesian coordinates, while from x=0.1 to x=1 for spherical and cylindrical coordinates to avoid singularity problems. In all cases, the domain is divided into 100 computational cells. We place a tracer particle at x=0.6. The particle is initially at rest and will be passed by a strong shock wave. We calculate the physical quantities of the particles by Lagrangian scheme and Eulerian scheme + tracer particle method. We adopt the simple Euler method as the intergration methods for the tracer particles. The results are reported at t=0.2 in Figures 4.1-4.12. There is good agreement between the results of the Lagrangian scheme and Eulerian scheme + tracer particle method. We have also tried a predictor-corrector method for time intergration, which produced no significant differences for this problem. These verification tests demonstrate that the Eulerian scheme + tracer particle method can provide the Lagrangian view of the hydrodynamics.

Our goal is to implement the tracer particle module to the supernova code "CHIMERA" (see Chapter 5). CHIMERA adopts "directionally split" algorithm. A time step update is accomplished by successive sweeps in each direction. When doing parallel computing,

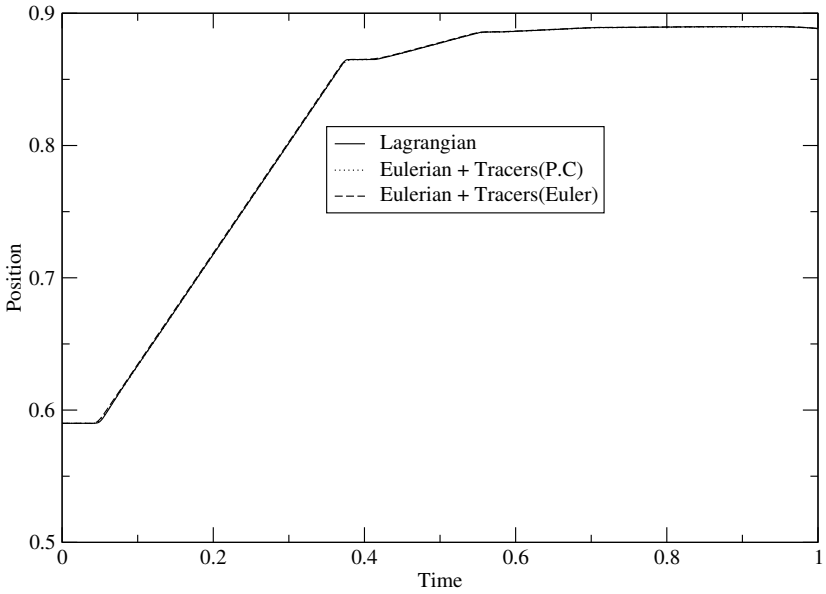

Figure 4.1: Particle position as a function of time for the 1D cartesian shock problem.

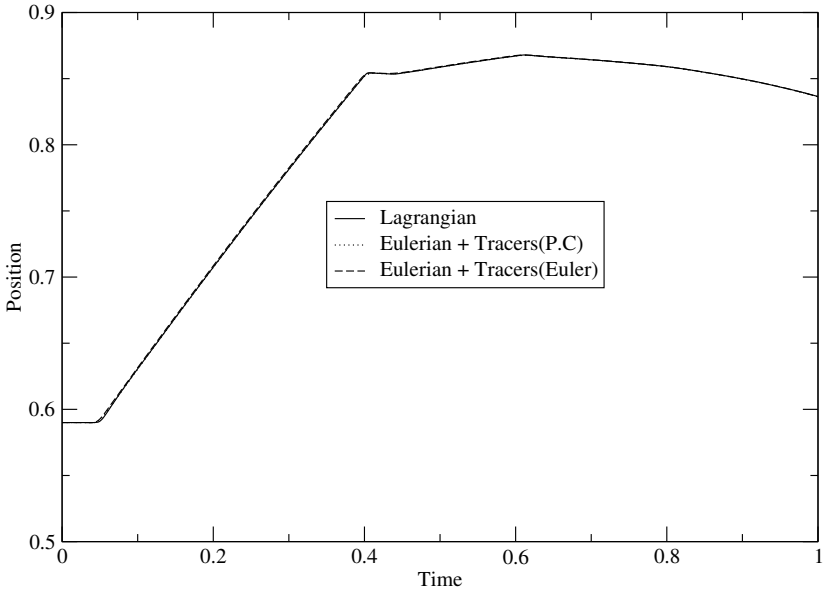

Figure 4.2: Particle position as a function of time for the 1D cylindrical shock problem.

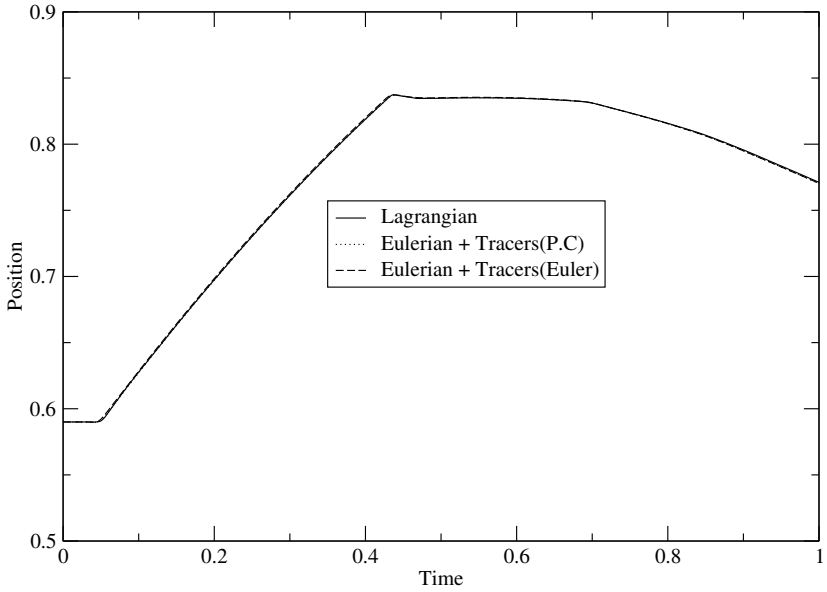

Figure 4.3: Particle position as a function of time for the 1D spherical shock problem.

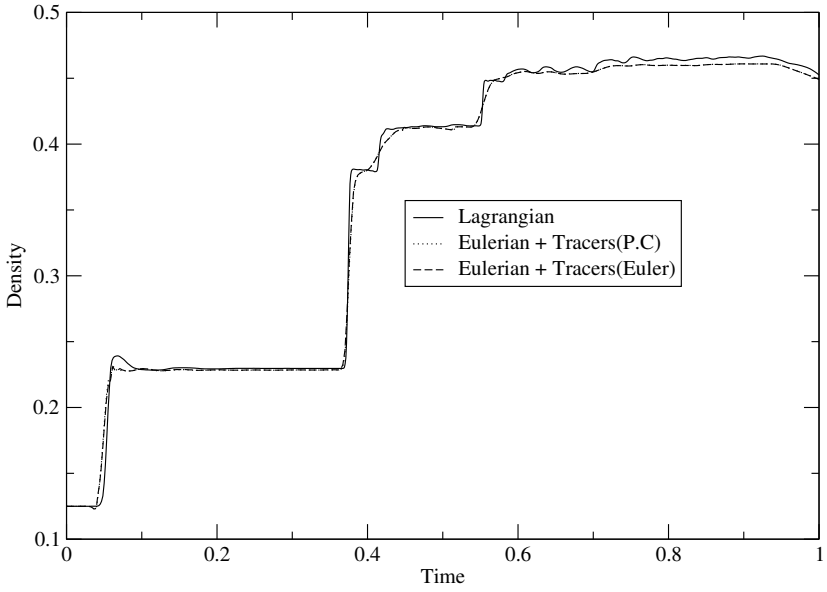

Figure 4.4: Particle density as a function of time for the 1D cartesian shock problem.

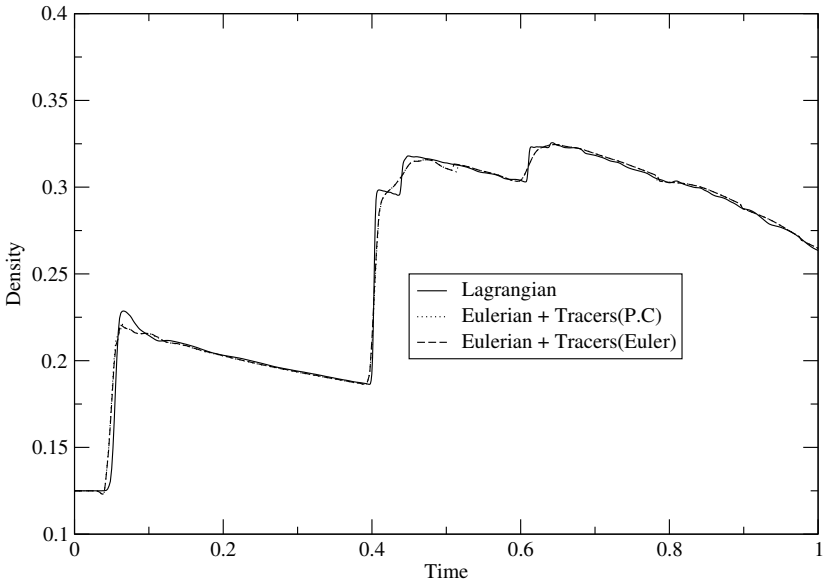

Figure 4.5: Particle density as a function of time for the 1D cylindrical shock problem.

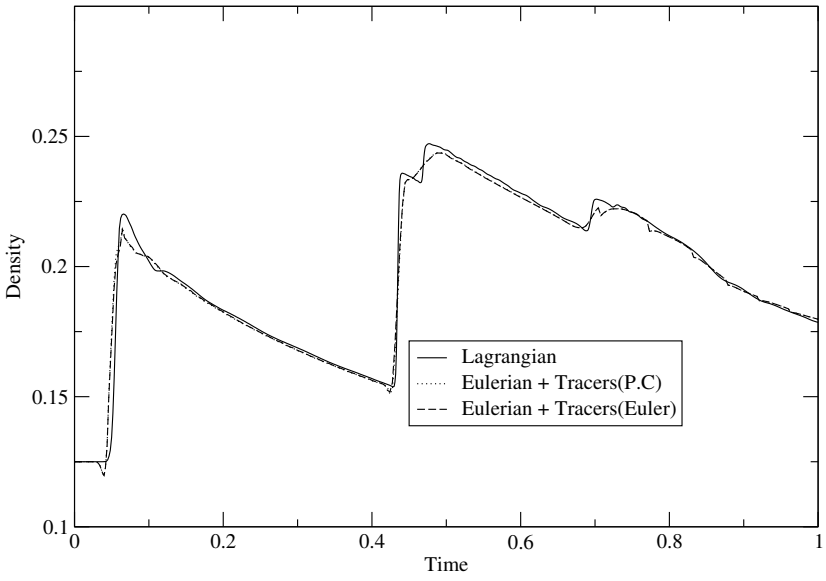

Figure 4.6: Particle density as a function of time for the 1D spherical shock problem.

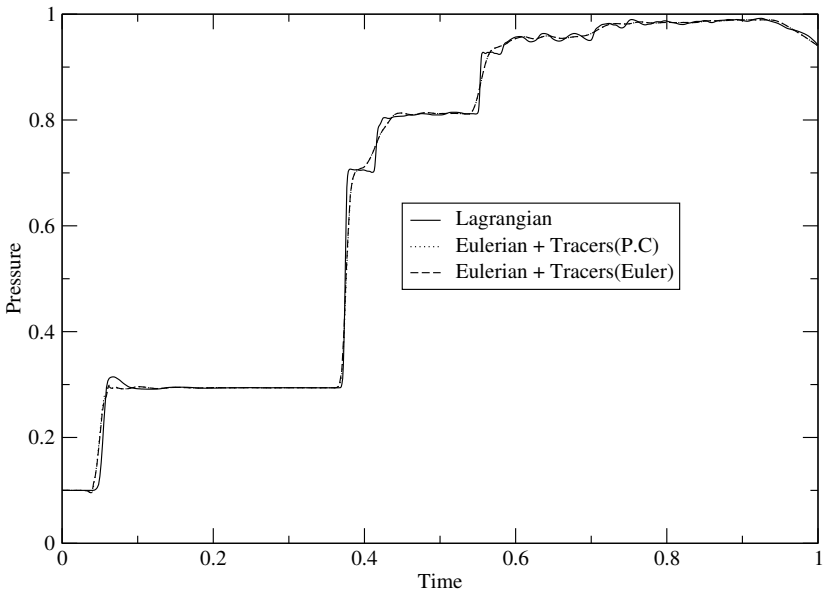

Figure 4.7: Particle pressure as a function of time for the 1D cartesian shock problem.

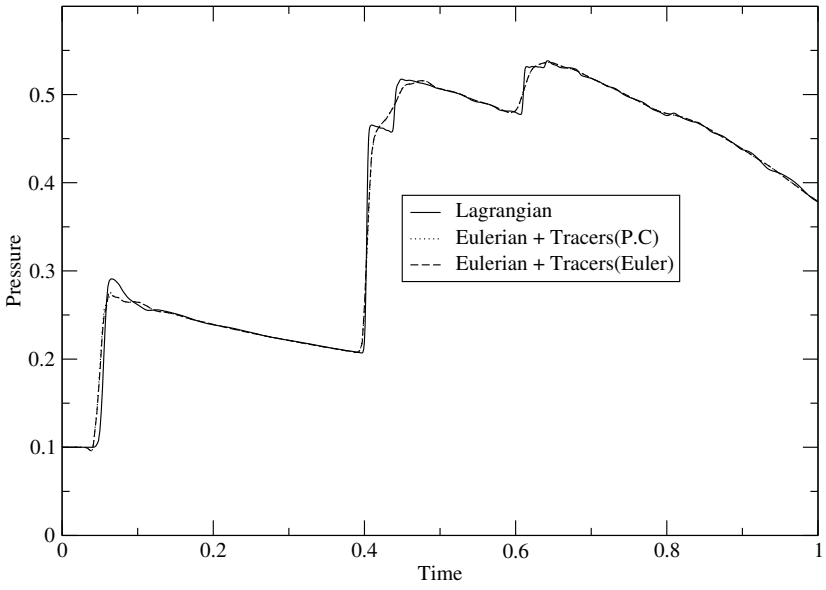

Figure 4.8: Particle pressure as a function of time for the 1D cylindrical shock problem.

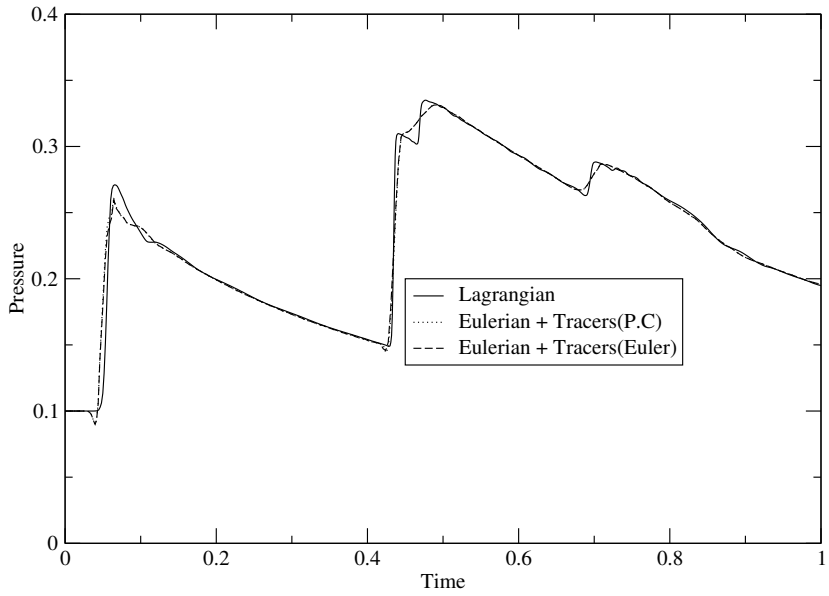

Figure 4.9: Particle pressure as a function of time for the 1D spherical shock problem.

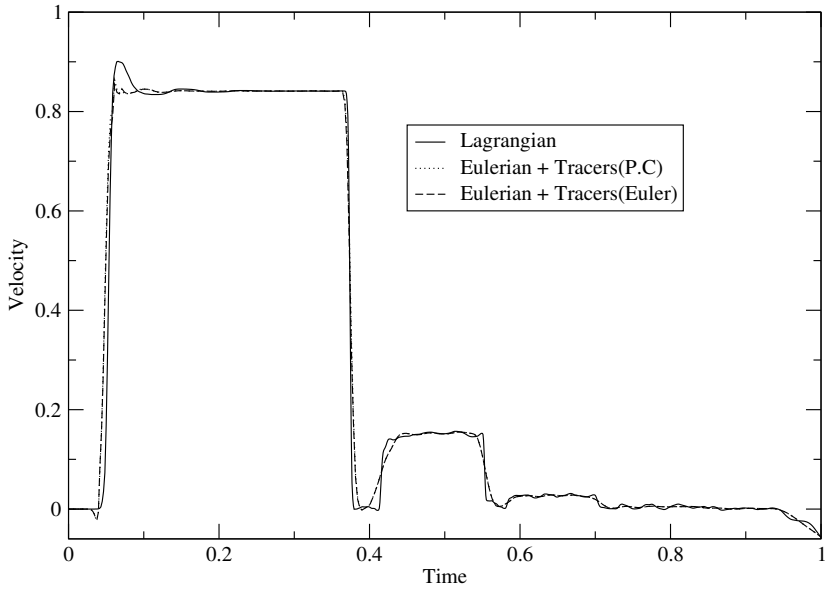

Figure 4.10: Particle velocity as a function of time for the 1D cartesian shock problem.

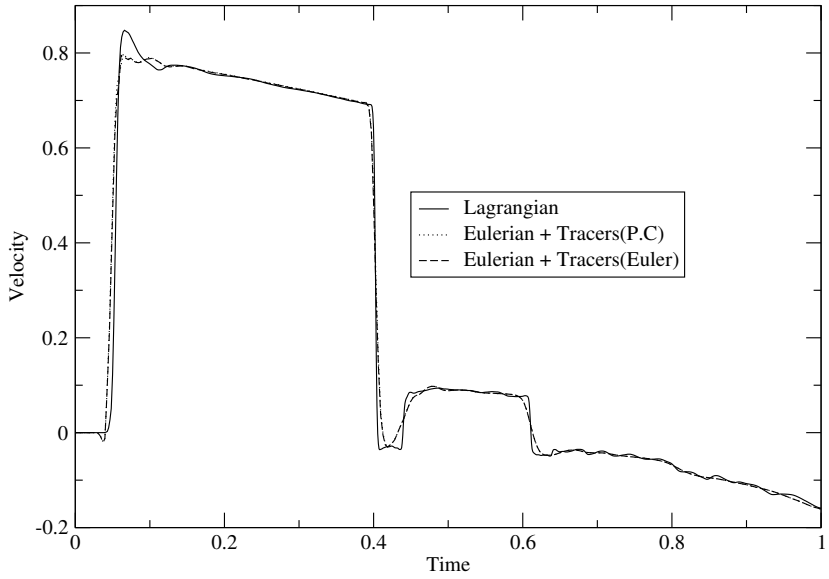

Figure 4.11: Particle velocity as a function of time for the 1D cylindrical shock problem.

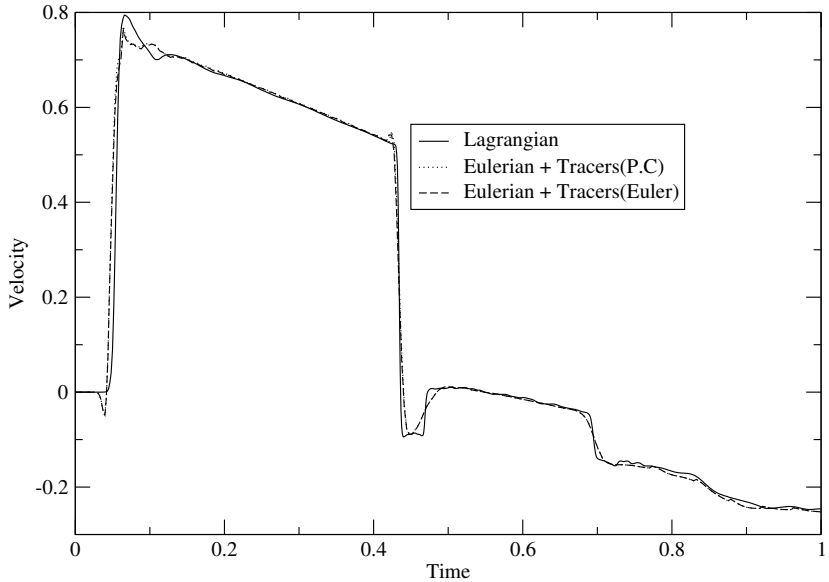

Figure 4.12: Particle velocity as a function of time for the 1D spherical shock problem.

each processor has only one ray of local data. This inhibits use of the 2D interpolation functions. Instead, we use the 1D interpolation and update the tracer particle data at each sweep. To test the validity of the 1D interpolation, we choose the 2D cartesian Sod shock problem. The initial position of the contact discontinuity is at a 45 degree angle so that the shock and rarefaction wave propagate diagonally. For comparison, we use 2D interpolation and update the tracer particle data after a pair of sweeps (X-Y). The results are shown in Figures 4.13-16. There is no significant difference between results of 1D and 2D interpolations.

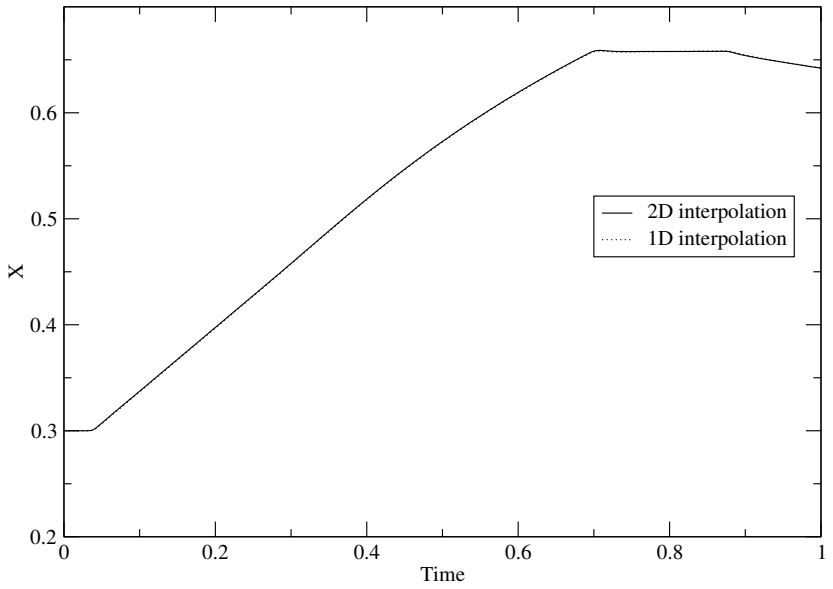

Figure 4.13: Particle position(X) as a function of time for the 2D cartesian shock problem.

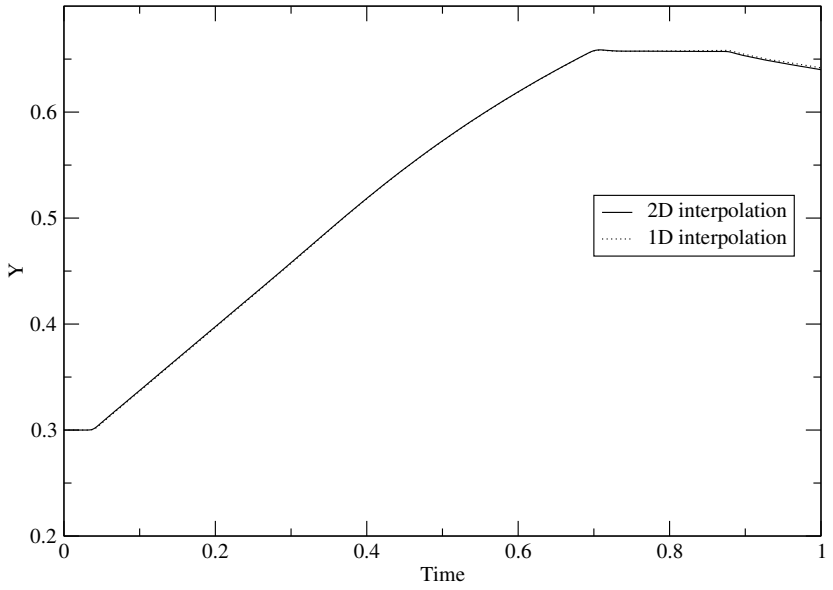

Figure 4.14: Particle position(Y) as a function of time for the 2D cartesian shock problem.

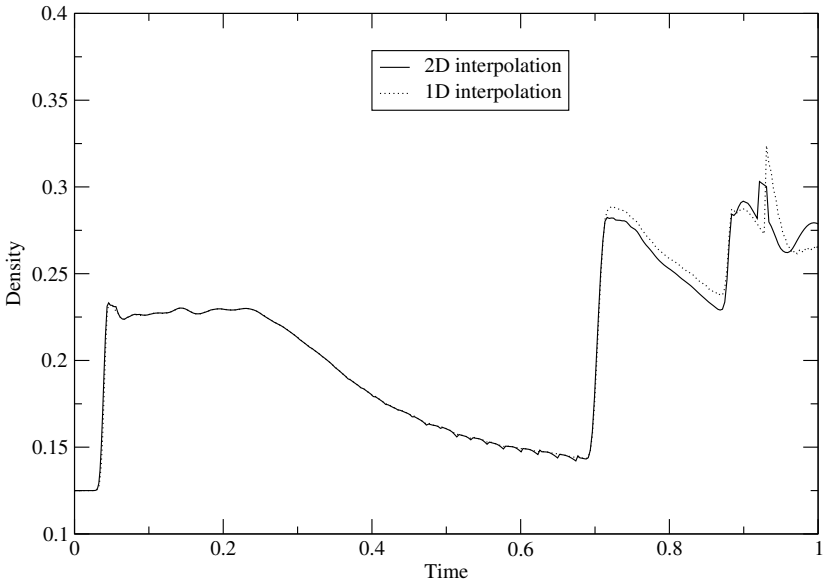

Figure 4.15: Particle density as a function of time for the 2D cartesian shock problem.

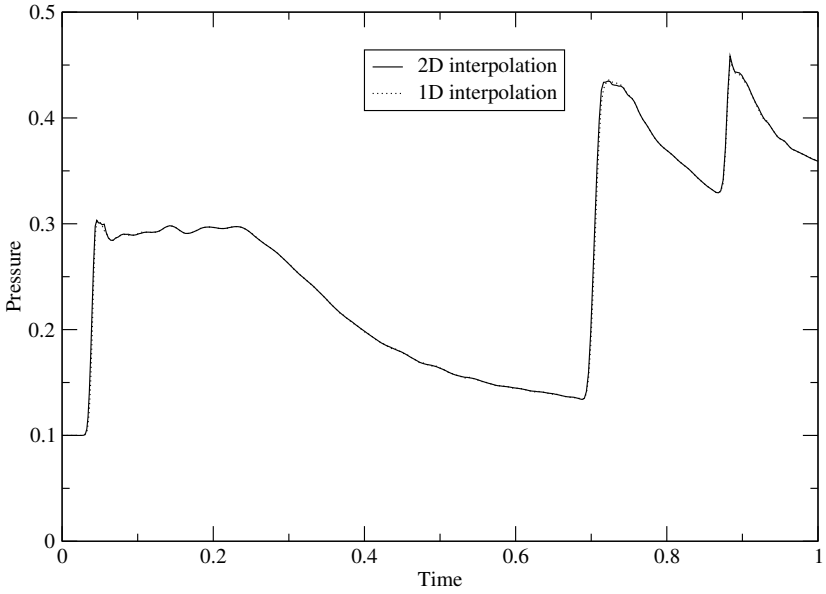

Figure 4.16: Particle pressure as a function of time for the 2D cartesian shock problem

Chapter 5

The implementation of the tracer particle module in CHIMERA

5.1 The supernova code "CHIMERA"

Supernovae are complex multi-physics phenomena in which several physical processes including hydrodynamic motion, neutrino processes, and thermonuclear processes are tightly coupled. For example, the thermonuclear reaction rate is strongly dependent on temperature, density and chemical composition of the fluid. On the other hand, thermonuclear processes release (or absorb) energy, which alters the pressure and causes hydrodynamic motion.

"CHIMERA" is a multi-physics and multi-dimensional code developed to simulate core-collapse supernovae. It is composed of three major modules, which describe different physical processes : hydrodynamics, neutrino transport, and nuclear reaction network. All components of the code have been written in a modular form with well-defined interfaces which deal with the coupling. The hydrodynamics component of CHIMERA is based on the VH-1 code which has been widely used in astrophysical

fluid dynamics simulations. VH-1 is a Lagrangian remap implementation of the piecewise parabolic method (PPM) [Col84]. VH-1 solves the hyperbolic set of the inviscous and compressible Euler equations instead of the parabolic set of the viscous and compressible Navier-Stokes equations. Viscosity and heat conduction are negligibly small in supernova explosions. In principle, neutrino transport should be implemented with full multi-D Boltzmann transport. But it would be very computational expensive. CHIMERA use a "ray-by-ray-plus" approximation for neutrino transport, whereby the lateral effects of neutrinos such as lateral pressure gradients (in optically thick conditions), neutrino advection, and velocity corrections are taken into account, but the transport is performed only in the radial direction. Transport is computed by means of multigroup flux-limited diffusion with a flux limiter that has been tuned to reproduce Boltzmann transport results to within a few percent. The neutrino opacities employed in CHIMERA are the standard ones described in [Bru85], with the isoenergetic scattering of nucleons replaced by the more exact formalism of [Red98], which includes nucleon blocking, recoil, and relativistic effects, and with the addition of nucleon-nucleon bremsstrahlung [Han98]. The nuclear reaction network in CHIMERA is Xnet, which is a fully implicit general purpose reaction network. However, currently only reactions linking the 14 alpha nuclei from ^{4}He to ^{60}Zn are used. Data for these reactions is drawn from the REACLIB compilations. The equation of state of Lattimer-Swesty (LS-EOS) is currently employed for matter at high densities. General relativistic effects are treated only approximately by a self-gravity solver.

CHIMERA use "operator split" + "directionally split" algorithm. On the one hand, the code evolves one physical process after another forward in time, feeding the results to the next. Different physics packages are allowed to be turned on or off by the users depended on their particular applications. On the other hand, the hydrodynamics is directionally split. Directional splitting allows the sequential evolution of

one-dimensional sweeps. A time step update is accomplished by successive sweeps in X-Y-Z directions. All the physical quantities are updated during each "sweep" step. To increase accuracy, these sweep steps are done in pairs, inverting the order of the sweeps. For 2D, we pair two time step updates in the order: X-Y-Y-X. However, the ray-by-ray neutrino transport and nuclear reaction network are performed only during the radial (X) sweep, when all the necessary data is local to a processor.

Like VH1, MPI parallelization of the CHIMERA code has been accomplished through a stripe-wise domain decomposition. Sweeps are made on "pencils" along one direction of a mesh. Then, a data transpose is performed to switch the sense of the sweeps to another directions. This decomposition is necessary for the ray-by-ray neutrino transport, as it allows a single "ray" to be resident on a processor at some point in a time step. This makes the neutrino transport solve a wholly local computation, requiring no communication between processors.

5.2 Tracer particles in CHIMERA

CHIMERA's highly modular framework endows it with great flexibility and extensibility. We have extended the CHIMERA code by adding a module to follow the evoluton of Lagrangian tracer particles. Implementation of the tracer particles has been much more involved, and interesting, than expected because of the unique parallel decomposition of the CHIMERA code. The hydro modules of CHIMERA, based on the VH-1 hydrodynamics code, use a global stripe-wise decomposition between processors instead of the more ordinary block decomposition. This requires a global transform of the data between directional sweeps, but obviates coordination of neighboring blocks and simplifies coupling with the ray-by-ray neutrino transport modules in CHIMERA, which also operate on radial stripes. This simplicity for the transport however makes

implementation of the tracers more difficult. Each processor has only one ray of local data. This inhibits use of the 2D interpolation functions. Moreover, the tracer particles must be assigned to processors correctly according to their positions. This requires much bookkeeping to keep track of the many particles. The passing of particles must be done via the All-to-All collective communication between sweeps in different directions.

The particle module has been implemented into the CHIMERA code. It contains several subroutines (Table 5.1). All the particle variables are declared in particle_module. The number of particles (npar) is read by the master processor and broadcasted to all the other processors. The input of the initial particle positions is read by the master processor. Then the particles are dispersed to different processors according to their positions. Subroutine radhyd_to_particlex and Subroutine radhyd_to_particlex serve as interfaces between the main program and the particle module. They are called at the end of each sweep step. The subroutine particlex_step and particley_step in turn calculate the particle quantities for the radial direction and the spherical-polar (θ) direction. The particle quantities include position, temperature, density, and neutrino flux for four flavors (Table 5.2). The hydro variables used in the tracer particle module are shown in Table 5.3. Assuming the neutrino spectra have Fermi-Dirac form, we can

Table 5.1: Description of the particle subroutines in CHIMERA

Subroutine name	Description
particle_module	declare particle variables
dimension_particle_arrays	allocate the dimensions of the particle arrays
radhyd_to_particlex radhyd_to_particley1 radhyd_to_particley2	interfaces between the main program and the particle module
particlex_step	evolve the tracer particles in the x direction
particley_step	evolve the tracer particles in the x direction
edit_particle	subroutine for output
particle_gather	gather particle data to make a restart file

Table 5.2: Particle variables and corresponding description

Particle variables	Description
px	particle positions in the x direction
py	particle positions in the y direction
pzte	temperatures of the particles
pzro	densities of the particles
pu	x velocities of the particles
pv	y velocities of the particles
pye	electron fraction of the particles
fluxe	neutrino flux
pfluxe	neutrino flux of the particles
ptemp	neutrino temperatures of the particles
pagr	lapse functions of particles

Table 5.3: Hydro variables extracted in tracer particle module

Hydro variables	Description
t_c	zone average temperature
rho_c	zone average density
u_c	zone average x velocity
v_y	zone average y velocity
ye_c	zone average electron fraction
agr_c	zone average of lapse function
unue_e	the zone_centered neutino energy
dunue_e	the width of energy zone
psi0_e	the first moment of the occupation distribution of neutrinos

deduce the neutrino temperatures from the neutrino flux. Both the neutrino flux and the neutrino temperature can be used the calculate the neutrino-matter interaction rates. Note the neutrino temperatures are not necessarily equal to the hydrodynamic temperatures.

The more tracer particles that are distributed in the simulations, the more detailed information we can gain on the nucleosynthesis. However, it may slow down the running significantly if we distribute too many tracer particles. The slow-down is very sensitive to the number of the particles and mainly due to the All-to-All collective communication and the I/O of the particle data. The tracer particles move from one processor to the other via the All-to-All communication at every cycle. All-to-All is a global communication which does not take into account whether the transferred data are really needed on remote processors. Therefore, there is a lot of redundant data involved in the communication, which makes it very time consuming. To decrease the delay resulted from All-to-All communication, we optimized the tracer particle module in two ways. First, we applied the simple Euler method instead of the predictor-corrector method. We have shown these two intergration methods give similar results (see Chapter 4.4). Thus the variables which need to be involved in All-to-All communication are reduced significantly. Second, we cancelled the particle data transposition between sweeps in the same direction, which reduced the number of the All-to-All communications needed.

The output of the particle data is another factor which can slow down the program's execution. For the sake of convenience, we output the data for each particle to an individual file. We open and close the output file for a given tracer on a given processor if the tracer particle happens to be on the processor. Since each processor outputs its own set of particle data, no communications between processors are needed. In addition to the output files, we also need to provide the particle positions for the

restart files. We may need to restart the running from time to time. The output of large quantities of data and the opening of many files is very time consuming, and the delay increases as the number of the tracer particles increases. Moreover, the frequent opening and closing of files can be technically problematic.

The performance test

We performed a short 2D simulation of a core-collapse supernova to see how the execution speed decreased with the number of tracer particles. The tests have been carried up on the Cray XT4, Jaguar, at the National Center for Computational Science with 256 processors. The progenitor model we adopted is the 20 solar-mass model of Heger et al. We started the run from the infall phase and set the walltime to be 90 min. The results are illustrated in Table 5.4, where we see the number of elapsed timesteps drop rapidly with increase of the particle number. Without output, using 8000 tracer particles costs only 8% slowdown. As we expected, the output is a very important factor to cause the slowdown. Using binary output causes almost the same slowdown as ASCII output. However, in this test, the size of each ASCII output file (934KB) is much larger than that of the binary output file (285KB). To save space, we adopt the binary output instead of the ASCII output in the future simulations.

Table 5.4: The number of cycles produced in 90 min walltime

Particle number	no output	binary output	ASCII output
0	839		
4000		716	
6000		675	681
8000	771	643	

The verification test

We performed a 2D simulation of core-collapse supernova to test the accuracy of the tracer particle module. The progenitor model for this model is the 11.2 solar-mass from Heger. We started the simulation from the infall phase and restarted the running many times to achive 17964 cycles (Time = 0.21514s). We have seen the tracer particles, which were initially in the inner iron core, suddenly halted (Figure 5.1). At the moment, the densities and temperatures of these tracer particles become very high (Figure 5.2-3). It's clear that the basic features of the core collapse and bounce have been reproduced in this simulation. This gives us confidence for future long-time simulations.

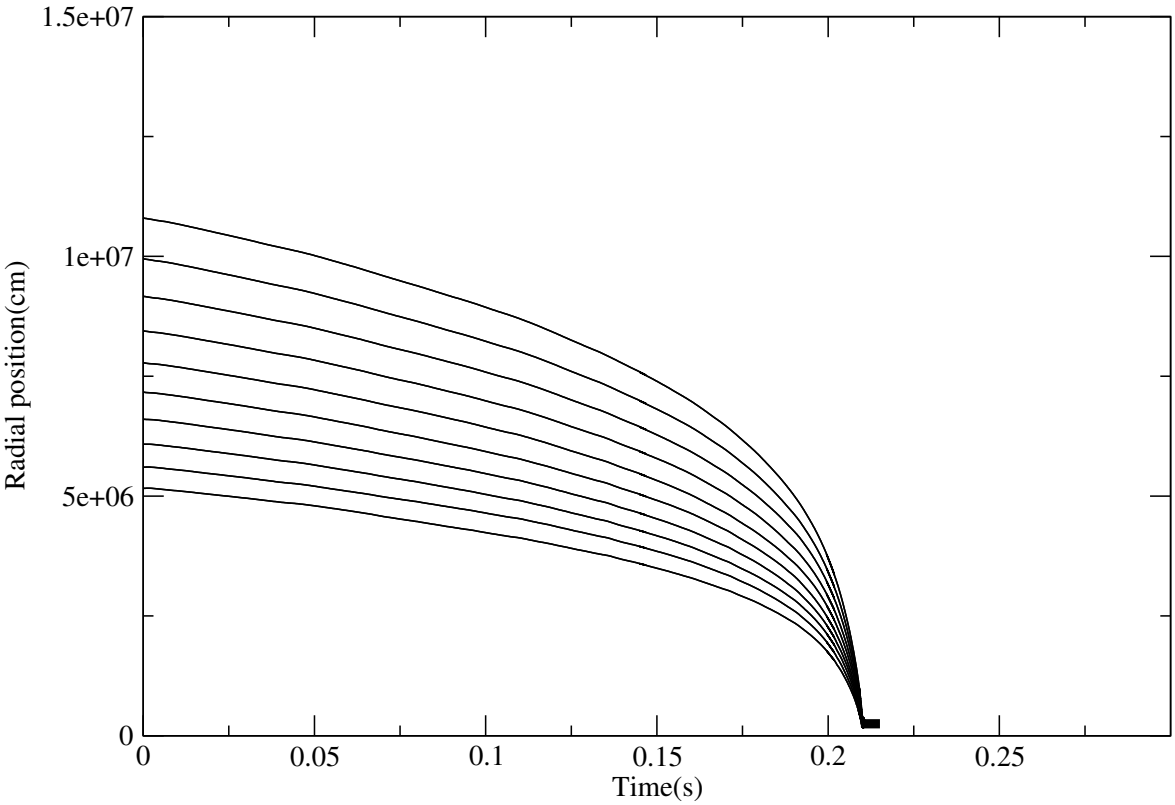

Figure 5.1: Particle positions as a function of time for the 11.2 Heger progenitor.

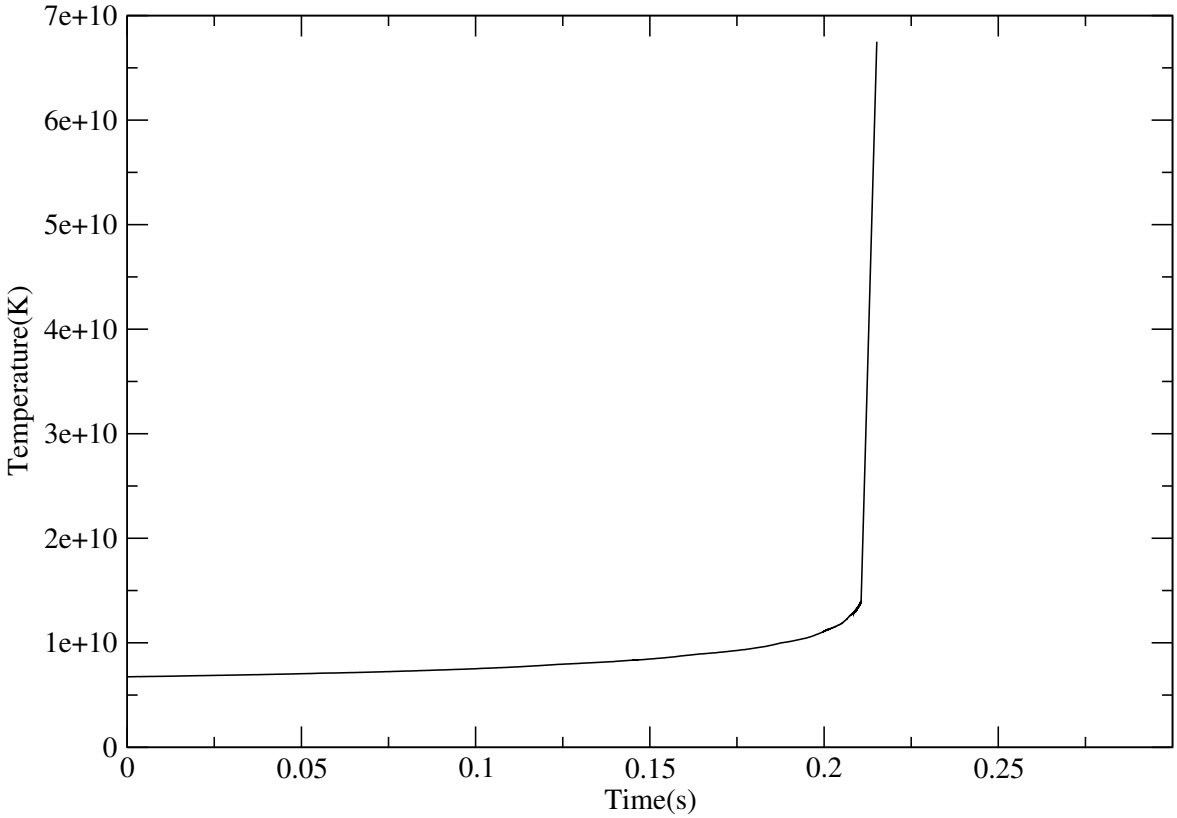

Figure 5.2: Particle temperature (the particle is initially at r=6×10^7cm) as a function of time for the 11.2 Heger progenitor.

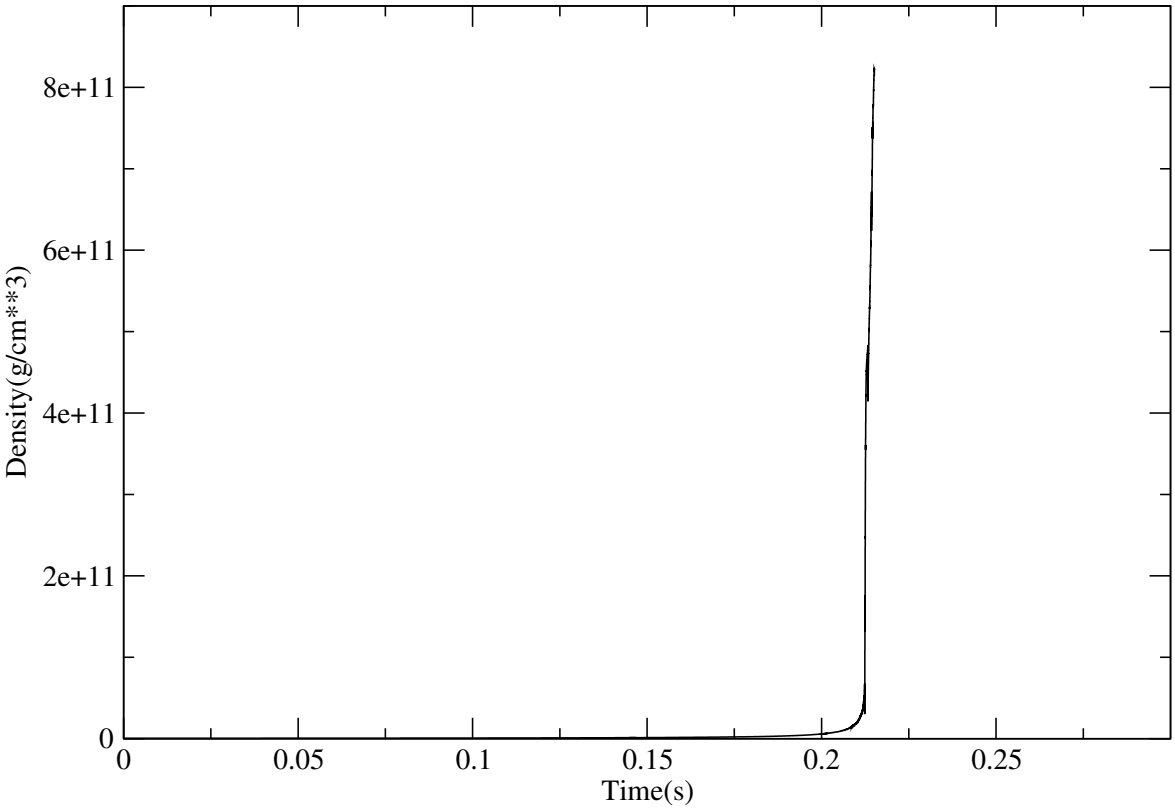

Figure 5.3: Particle density (the particle is initially at r=6×10^7cm) as a function of time for the 11.2 Heger progenitor.

Chapter 6

Multi-D supernova simulations

Based on the CHIMERA code, our group is performing a series of 2D simulations of core-collapse supernovae with 256 radial and 256 angular zones, assuming axisymmetry. The progenitor models we adopted are 12, 15, 20, and 25 solar mass models from Heger et al. [Woo07]. All of the simulations ran on 256 processors. Initially we disperse 4000, 5000, 6000 and 8000 particles for these models which we call Heger12, Heger15, Heger20 and Heger25, respectively. The particles are dispersed homogeneously (in mass) in the radial direction throughout the outer part of the iron core, silicon-rich and oxygen-rich layers, while they are dispersed uniformly in the polar direction. The relations between the radius and the enclosed mass for the progenitor models are shown in Figure 6.1. We use the 2-4 order polynomials to fit the original data of the progenitor files. By using these polynomials, we can make initial tracer particle files. Our 2D simulations were carried out from infall.

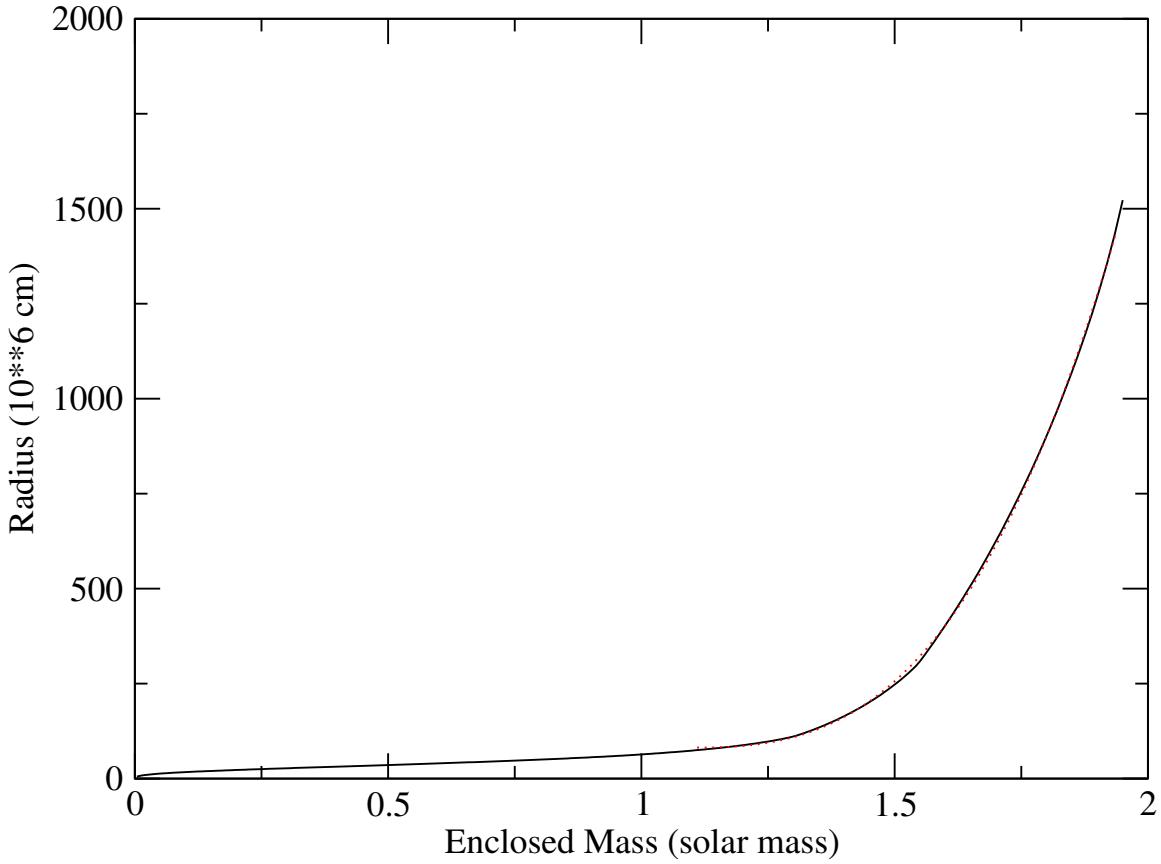

Figure 6.1: Radius vs. enclosed mass for Heger12 model. The solid line shows the original data from the progenitor file. The red dashed line is plotted by the fitting polynomial: r=1890$\times m^3$-5869$\times m^2$+6038.1$\times m^1$-1974.4

6.1 Results of the Heger12 model

The first main application of the tracer particle method is to provide a Lagrangian description of supernova simulations. We start by examining the motion of the tracer particles for the Heger12 model. In this model, we disperse 1040 particles in the iron core and 2960 particles in the silicon-rich and the oxygen-rich layers (Figure 6.2). These particles are named from 0001 to 4000 according to their initial positions. The inner part of the iron core bounces around 227ms. The nuclear repulsion at high densities drives the shock wave at core bounce. The passage of the shock wave heats up the matter inside the iron core. However, the shock wave stalls quickly because of the energy loss due to neutrino escape and photo-disintegration of the matter. Until the bounce shock stalls, the evolution of the core is essentially spherical. Using Lagrangian tracer particles allows us to obtain the temporal evolution of the physical quantities for individual fluid elements. Figures 6.3-6.6 show the evolution of the hydrodynamic variables for particle 0010 through infall and bounce. As seen in Figure 6.3, particle 0010 goes through the shock very soon after bounce at the time $\approx$ 230ms. Then temperature and density of particle 0010 increase rapidly. The electron fraction of particle 0010 varies slowly during the infall but drops suddenly around 230ms when the shock drives the density over 10^{11} g/cm^3. The sudden drop of electron fraction results from the rapid deleptonization following the shock induced dissassociation of the nuclei into free neutrons and protons. Particle 0010 continues to fall into the center of the core. It is unlikely to be ejected.

Figures 6.8-12 show the particle distribution at 235ms, 240ms, 392ms, 414ms and 417ms after the start of the simulation. For comparison, we also plot the initial particle distribution in this region in Figure 6.7. At 235ms, the inner particles are approching r = 10^7 cm. At 240ms, some of the particles have falled into r = 10^7 cm, and the

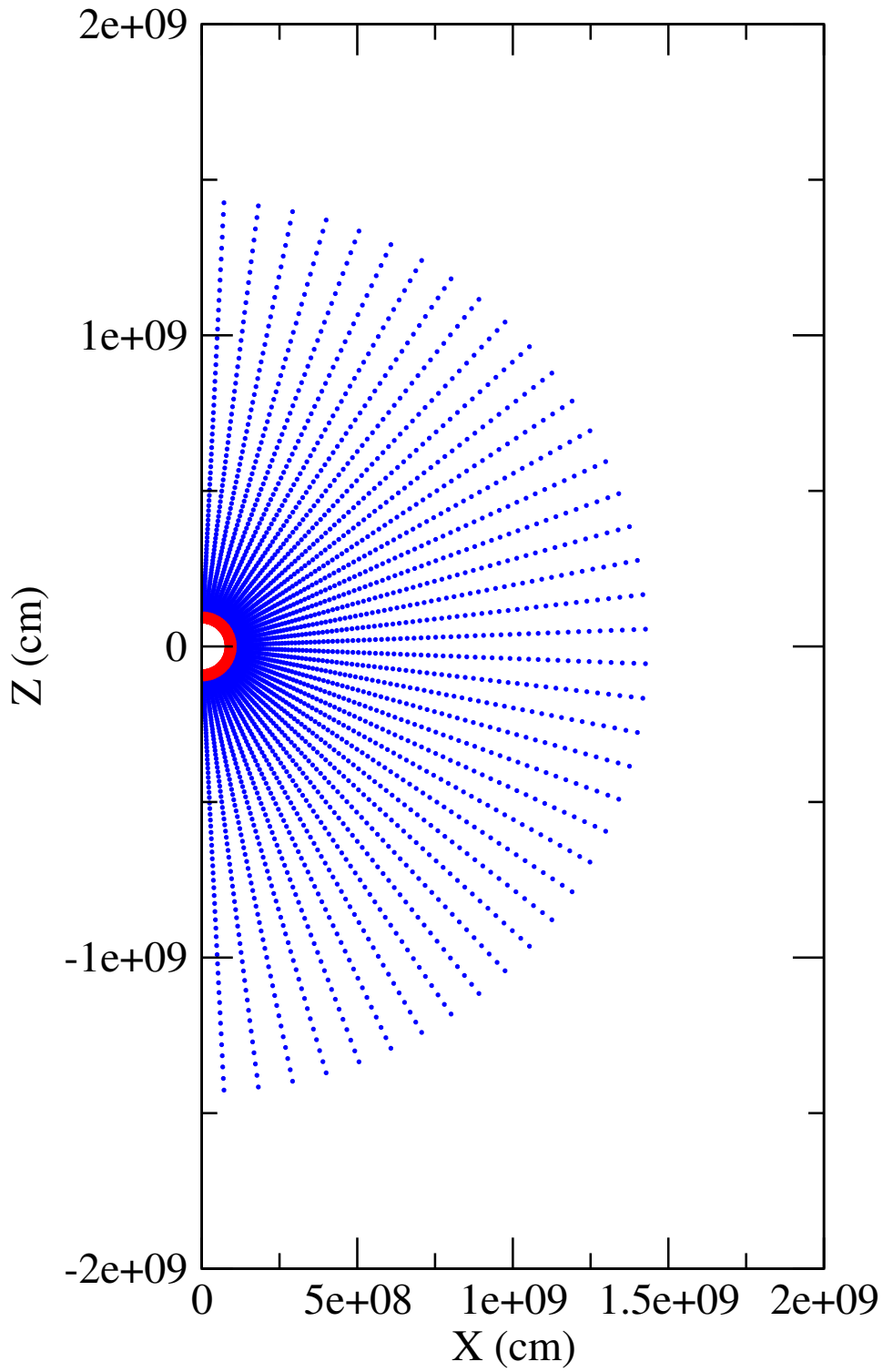

Figure 6.2: Initial distribution of tracer particles for the Heger12 model. The tracer particles in the iron core are plotted in red color, while the tracer particles in silicon-rich and oxygen-rich layers are plotted in blue color.

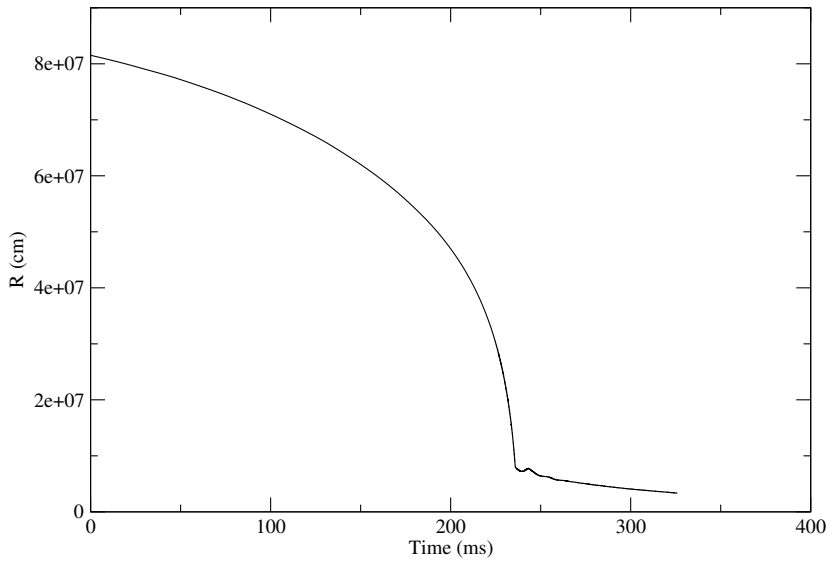

Figure 6.3: Radial position as a function of time for particle 0010.

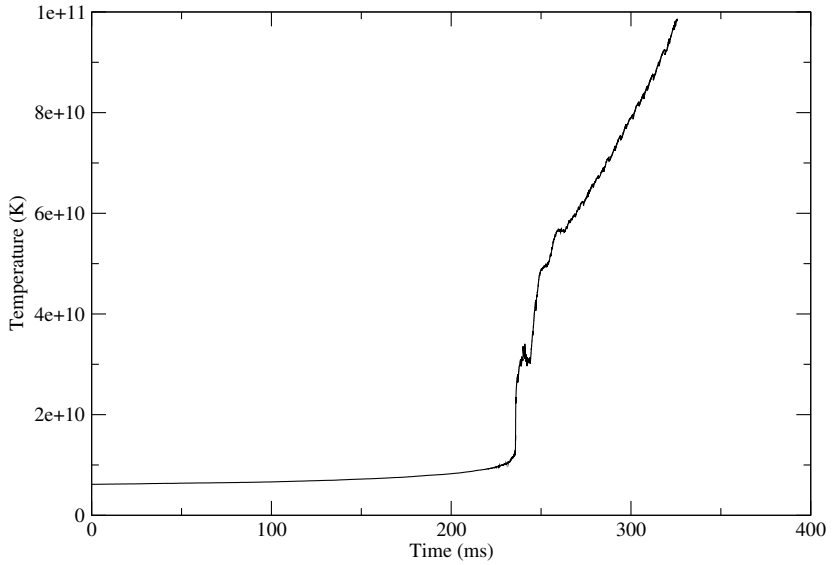

Figure 6.4: Particle temperature as a function of time for particle 0010.

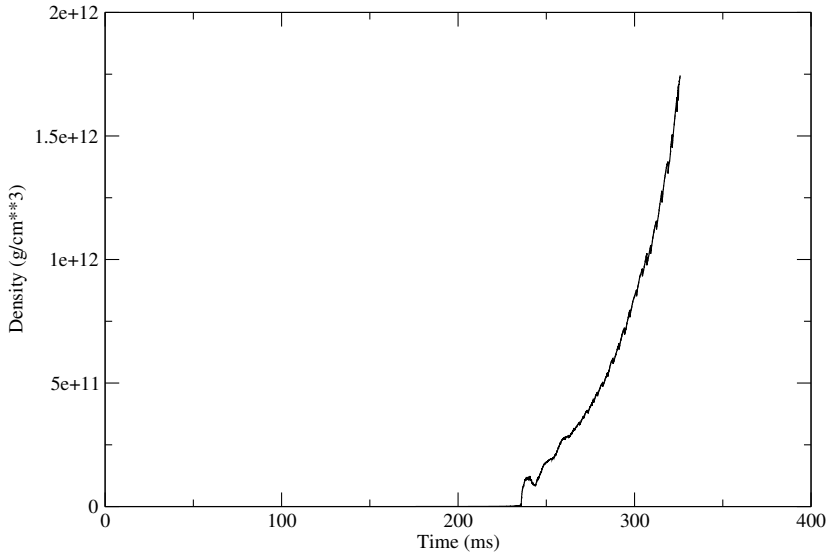

Figure 6.5: Particle density as a function of time for particle 0010.

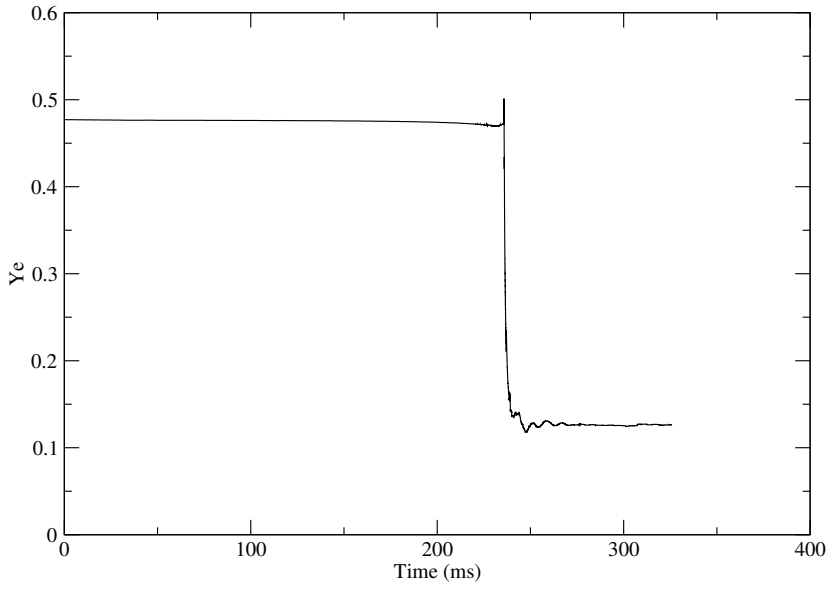

Figure 6.6: Electron fraction as a function of time for particle 0010.

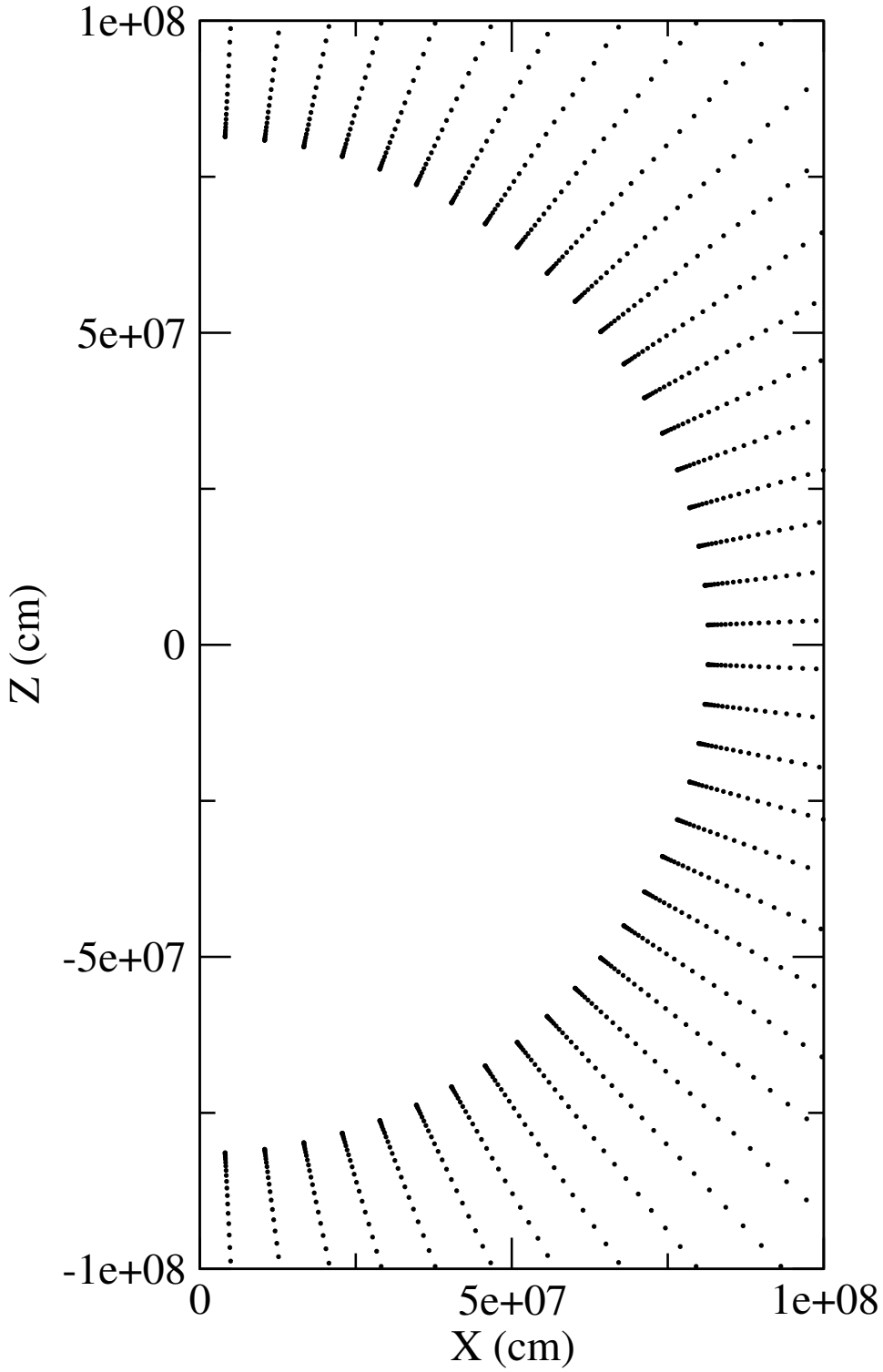

Figure 6.7: The distribution of tracer particles for the Heger12 model at the start of the simulation.

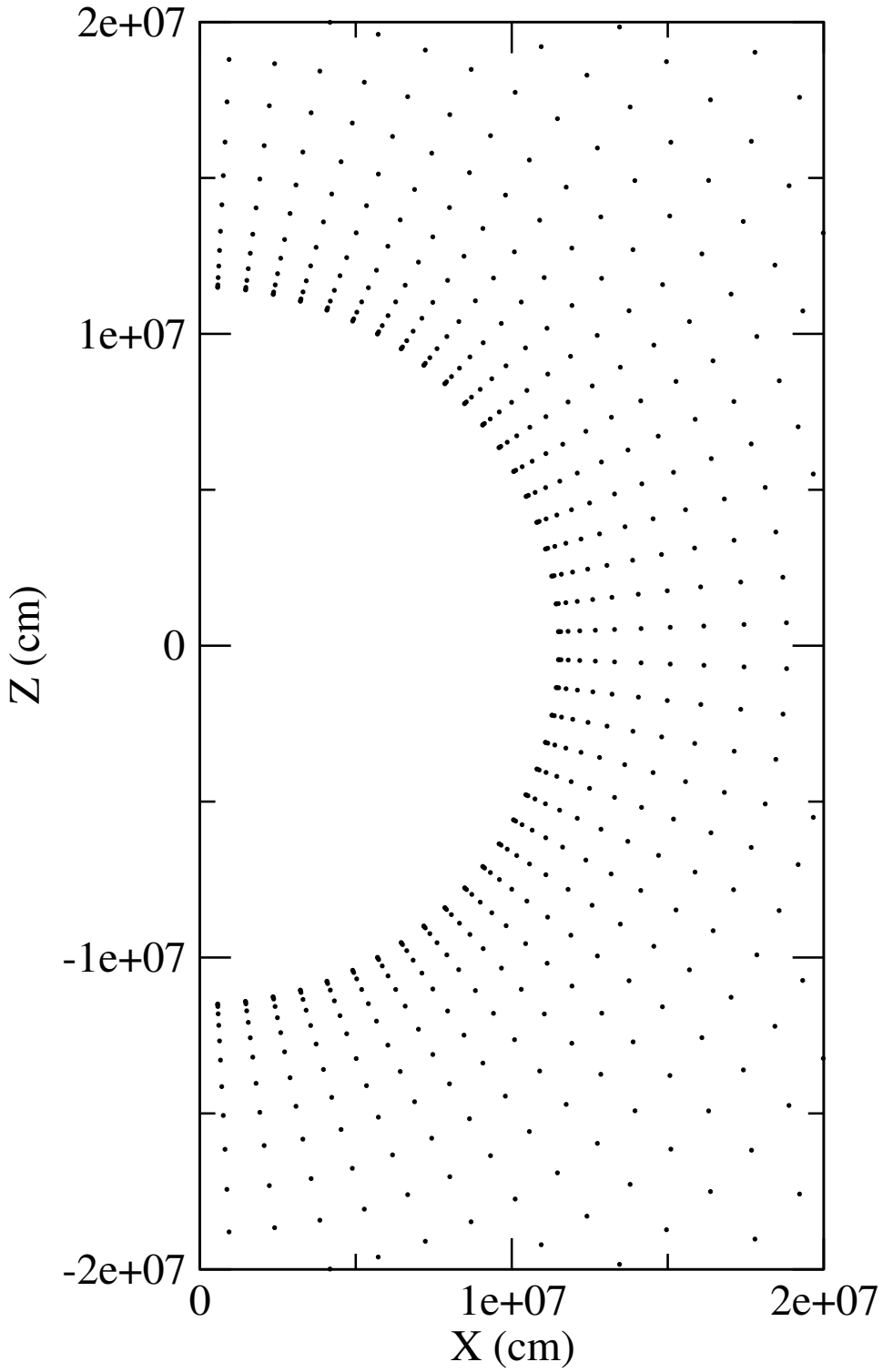

Figure 6.8: The distribution of tracer particles for the Heger12 model after 235 ms of simulation.

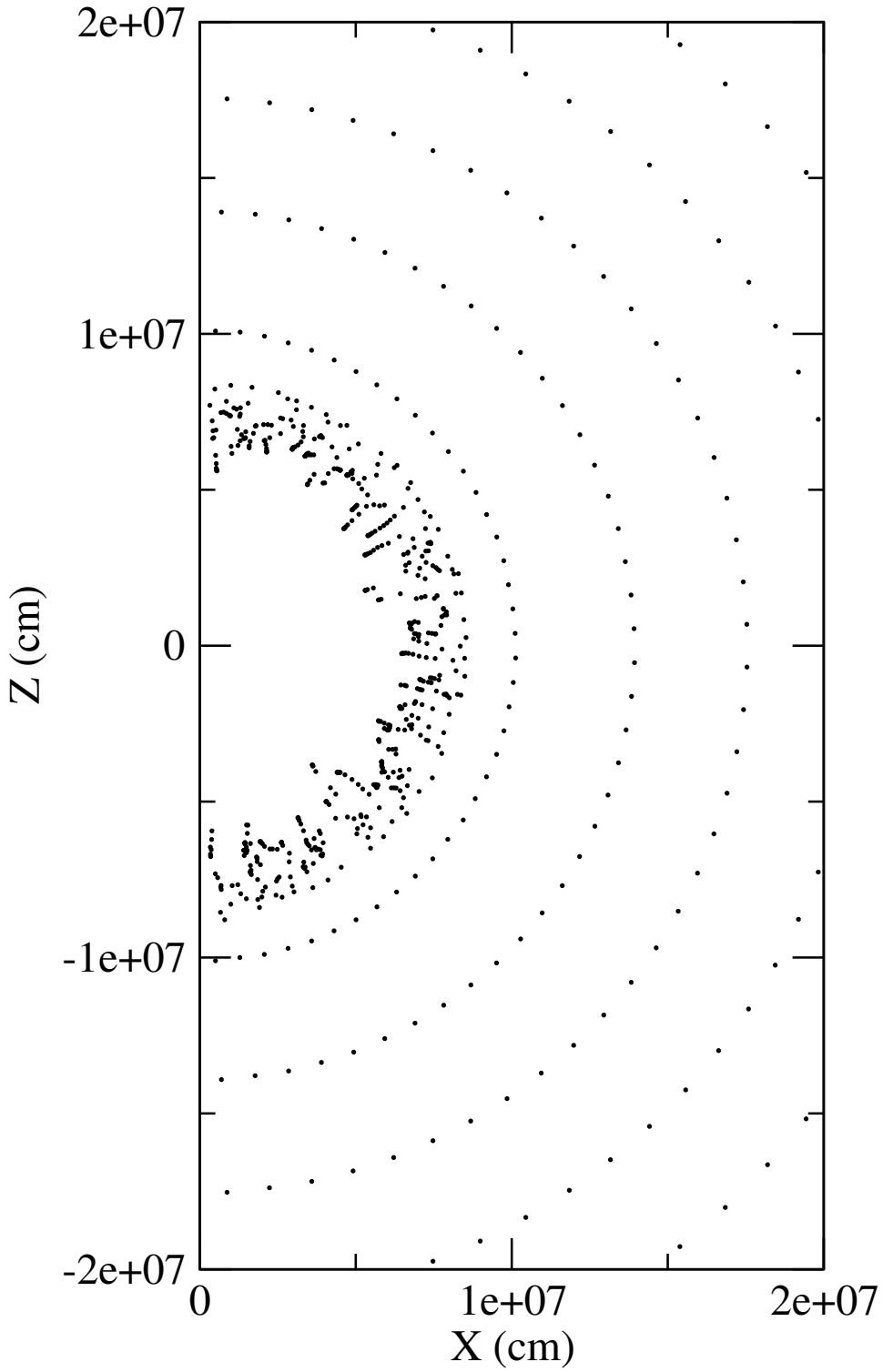

Figure 6.9: The distribution of tracer particles for the Heger12 model after 240 ms of simulation.

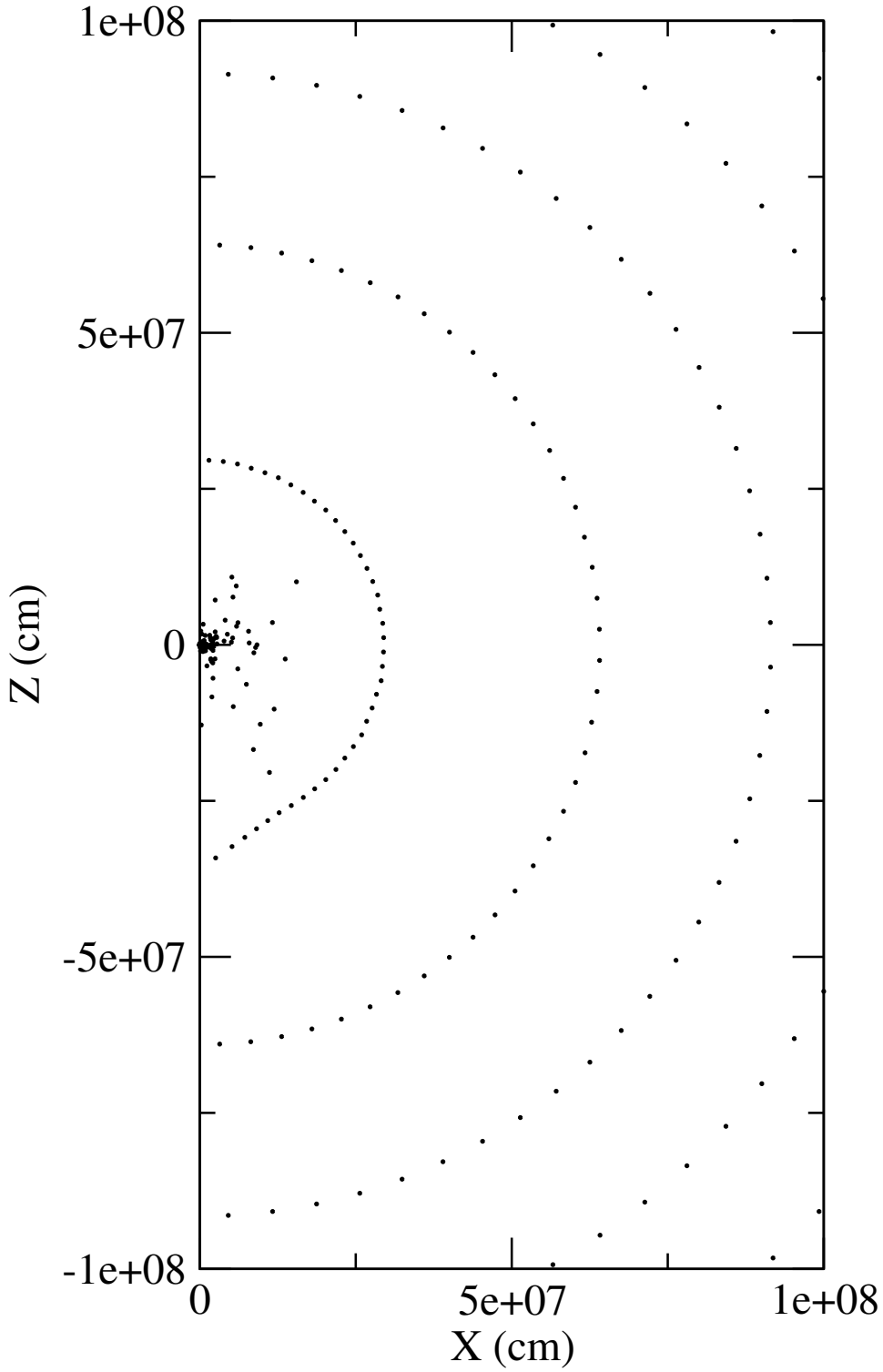

Figure 6.10: The distribution of tracer particles for the Heger12 model 392 ms after the start of the simulation.

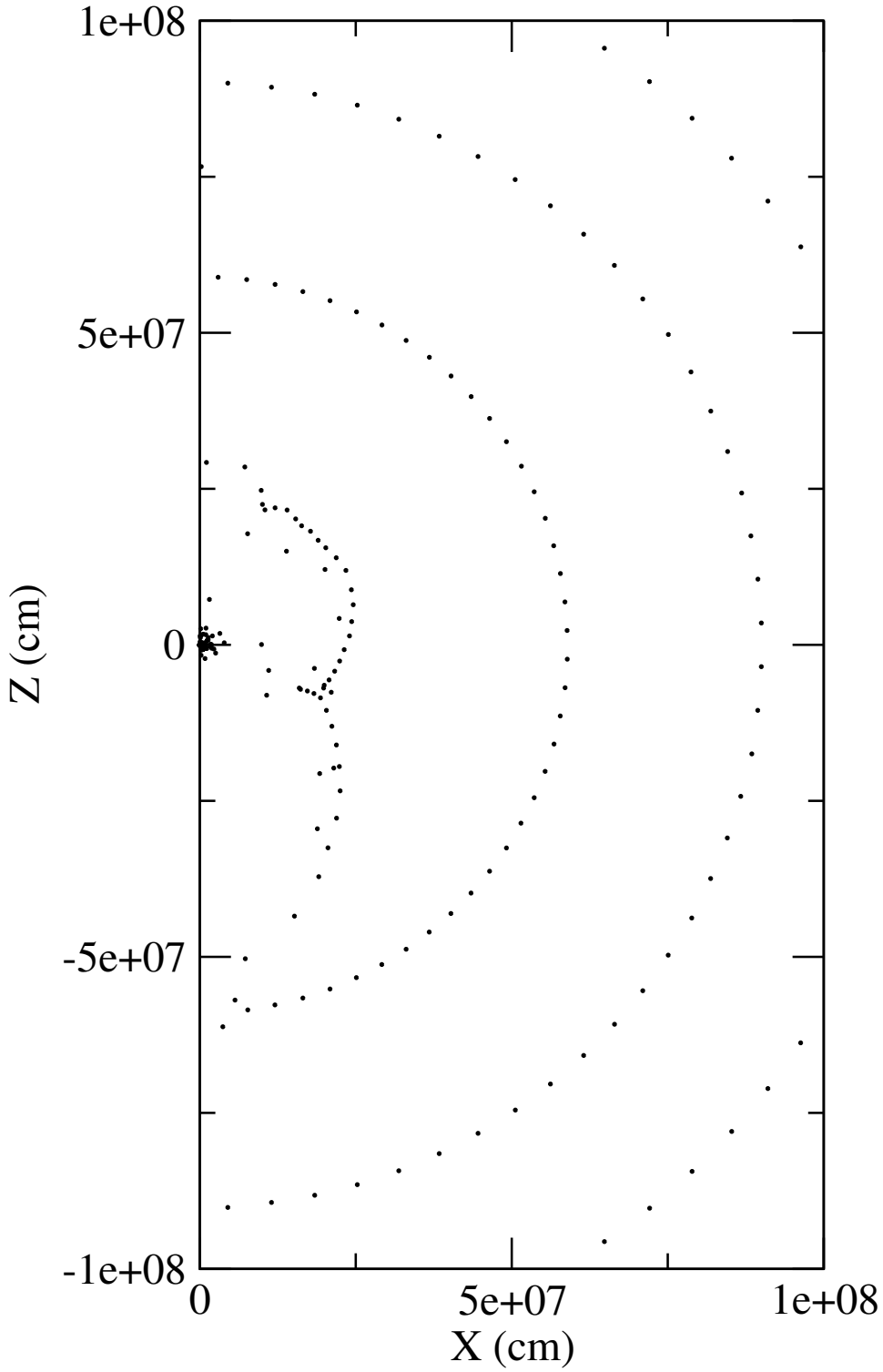

Figure 6.11: The distribution of tracer particles for the Heger12 model 414 ms after the start of the simulation.

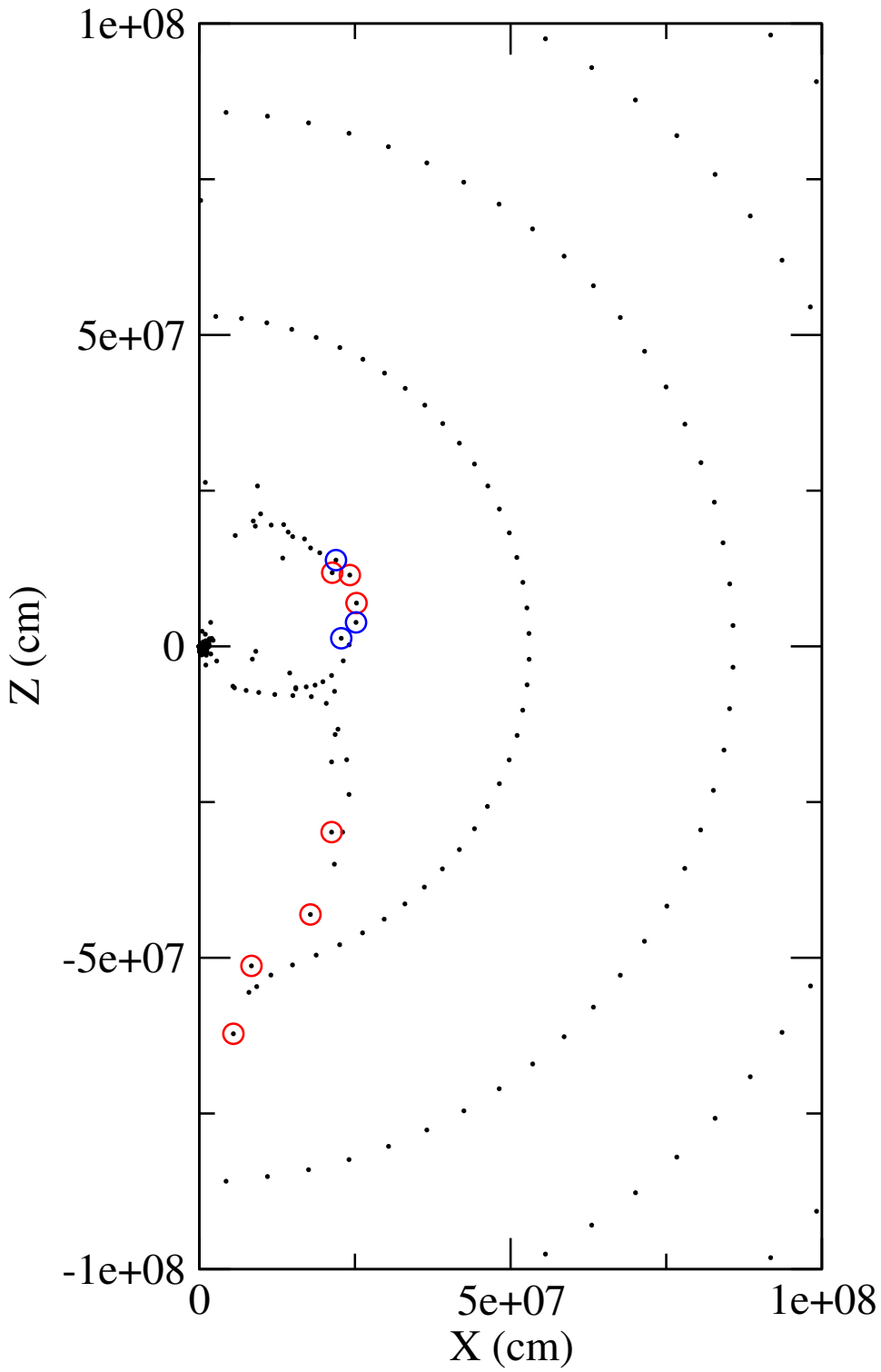

Figure 6.12: The distribution of tracer particles for the Heger12 model at 417 ms after the start of the simulation. The red cicles mark the exploding particles which have radial velocities larger than 10^8 cm/s. The blue cicles mark the explodingparticles which have radial velocities between 10^7 cm/s and 10^8 cm/s.

distribution of the particles begins to exhibit departure from spherical symmetry. We attribute this to the convective instability developing behind the shock. Convection breaks the spherical symmetry and helps produce the explosion. By 392 ms, the distribution of the particles is highly aspherical within r = 3×10^7 cm . The outer part of the particles are still collapsing spherically. Around 400 ms, we found the first signs of the explosion. Figure 6.10 shows the positions of some particles which have positive velocities at $\approx$ 417ms. The radial positions of these particles are larger than 10^7 cm. They were initially in the silicon-rich layer. Analysis of the tracer particle data can reveal the aspherical geometry of the explosion. As seen in Figure 6.12, there may exist two possible preferential directions of the explosion. It will be interesting to see if the explosion will become bi-polar or jet-like. We will have to follow the explosion for a longer time to make final statements.

Using the tracer particle method can provide information about these exploding particles in detail. We plot the time evolution of physical quantities for the exploding particle 1557 (Figures 6.13-15). This particle passes through the shock wave and gains positive velocity. At the same time, the temperature and density of this particle increase significantly. As seen in the Figure 6.13, the electron fraction drops suddenly when the particle passes through the shock. This is due to the rapid electron capture, similar to that described by Frohlich et al [Fro06a]. As the particle is being ejected, it experiences decreasing density. Once electron degeneracy is lifted, electron capture drops and neutrino captures rises. This results in the sharp rise of the electron fraction. Other exploding particles exhibit similar behavior to particle 1557. The distribution of these exploding particles is highly anisotropic becuase they were recently deflected by a deformed shock wave.

At 417ms, the shock wave is highly asymmetric, extending from 290 km to 540 km. We attribute the strong deformation of the shock to the standing accretion shock

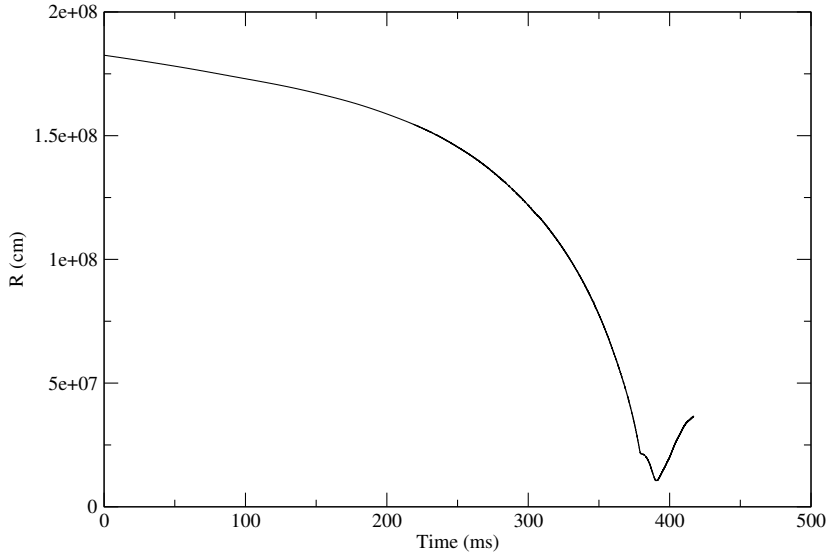

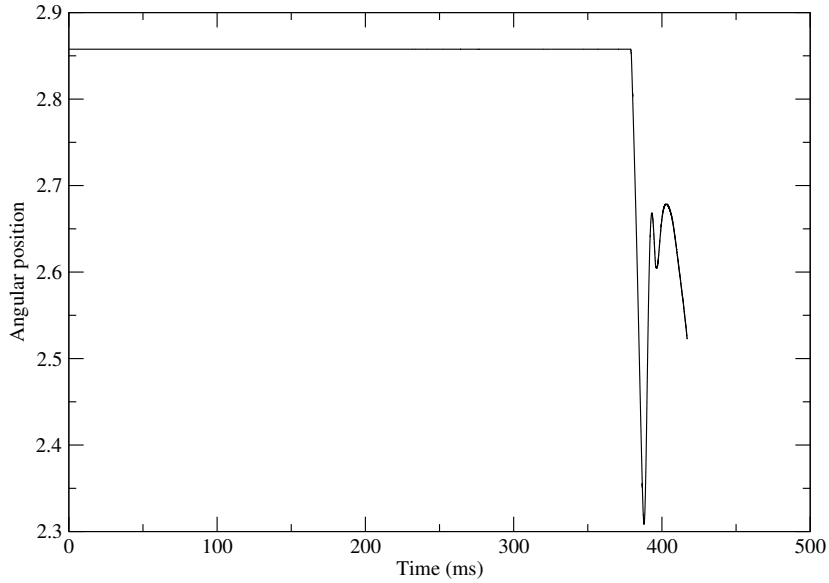

Figure 6.13: Radial and angular positions as functions of time for particle 1557.

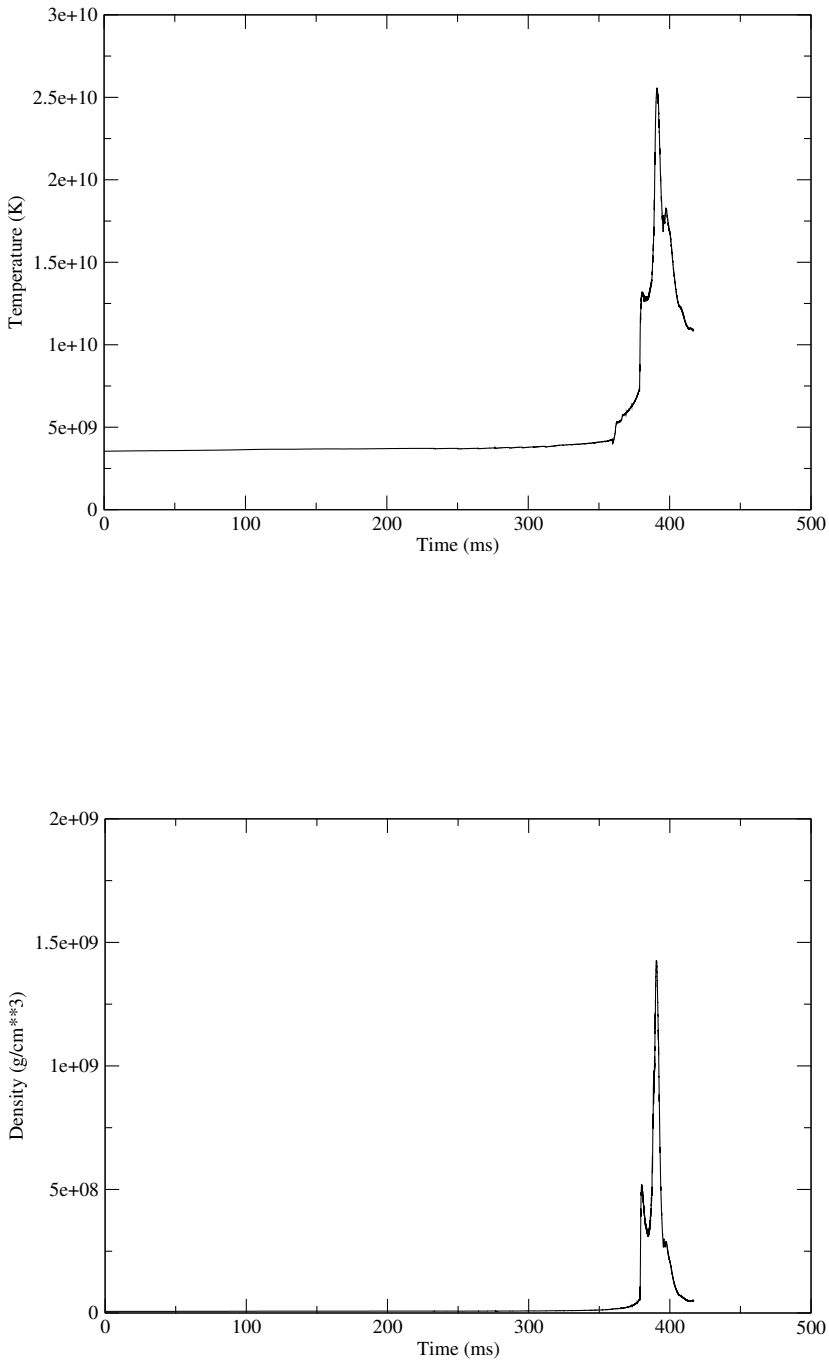

Figure 6.14: Temperature and density as functions of time for particle 1557.

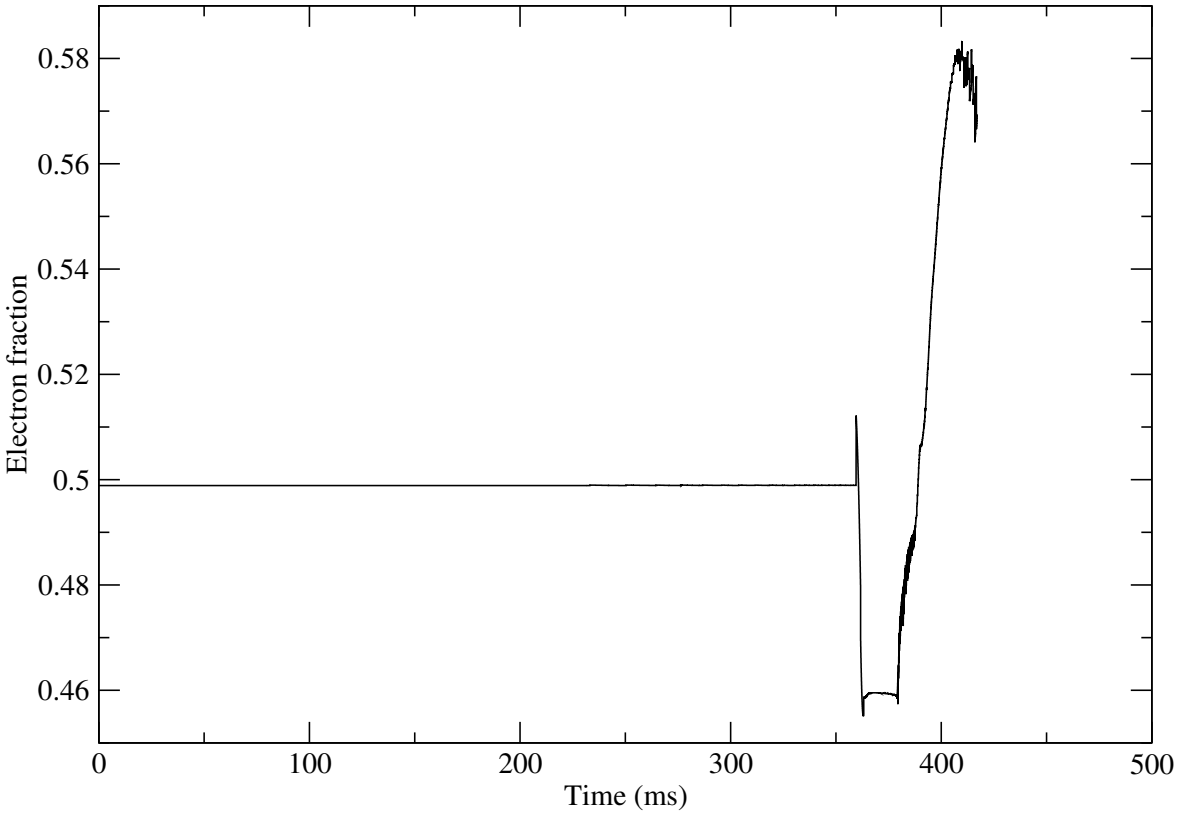

Figure 6.15: Electron fraction as functions of time for particle 1557.

instability (SASI). The SASI pushes the shock farther out and helps reverse falling particles to move outward. Behind the shock, there is a "hot bubble" region where the density is low and the temperature is high. This region is thought to be the ideal site of the νp-process and later the r-process. The strong neutrino fluxes from the surface of the proto-neutron star may later drive a continuous mass flow into the hot bubble region. The so-called "neutrino driven wind" is used to denote this outflow of material. All of the tracer particles we dispersed in the iron core sink into the deep core within 417ms. They are unlikely to be ejected. This suggests that the explosion does not set in the iron core, but in the silicon-rich layer. However, if the "neutrino driven wind" mechanism works, some tracer particles may rise from the deep core later as part of this wind.

6.2 Nucleosynthesis calculations

The nucleosynthesis calculations in this chapter are based on the simulation of the Heger12 model. Using tracer particles to follow the simulation, we obtained the temperature and density history of the matter as well as its neutrino exposure. Thus we are able to calculate the post-processing nucleosynthesis using a large nuclear reaction network. The ejecta from the innermost part of the supernova can be divided into two categories: the hot bubble ejecta and the neutrino driven winds [Pru05]. Material in the hot bubble comes from a region outside the proto-neutron star that is made convectively unstable by neutrino heating. The neutrino driven wind originates later from the surface of the proton-neutron star and is pushed outward along pressure gradients caused by neutrino heating. Both of these ejecta are thought to be initially proton-rich. This provides the necessary conditions for the production of the proton-rich isotopes

between A = 92 and 126. Though many recent studies focus on early proton-rich outflows, there remains the possibilities that some small amount of neutron-rich material which is ejected at late times. It is interesting to see if the neutron-rich outflows can satisfy the conditions needed for r-process.

Neutrino reactions play an important role in supernova nucleosynthesis. We have included the neutrino reactions in the nuclear reaction network Xnet. Assuming the type of the neutrino spectra is Fermi-Dirac, we calculate neutrino temperatures for four types: electron neutrinos, anti-electron neutrinos, muon (or tau) neutrinos, and anti-muon (or tau) neutrinos. We do not differentiate muon neutrinos and tau neutrinos in our simulations. The neutrino temperatures for muon (or tau) neutrinos and anti-muon (or tau) neutrinos are not used in our nucleosynthesis calculations. The available neutrino cross sections include only electron and anti-electron neutrinos. The peak around 230ms resulted from the neutrino burst which occurred just after bounce. At time = 370ms, the particle encounters a shock wave and enters the convecting region which results in strong peaks and fluctuations of both hydrodynamic temperature and neutrino temperatures. Figures 6.16-25 show the temporal evolution of physical quantities for several exploding particles. These particles just pass through the shock and fall in the hot bubble. Hitting the shock raises their temperature and entropy. The neutrino heating in the hot bubble provides additional energy to these particles and help them to rise. The neutrino temperatures of the exploding particle 1557 are shown in Figure 6.26. Particle 1557 has reached its peak temperature and began expanding outward at time = 413ms. At this moment, the electron fraction of most exploding particles is larger than 0.5.

With the Heger12 model, at this writing, 417 milliseconds after the onset of collapse and only just showing the earliest signs of explosion, a full analysis of the nucleosynthesis from this model would be premature. Perhaps another 500 milliseconds or more

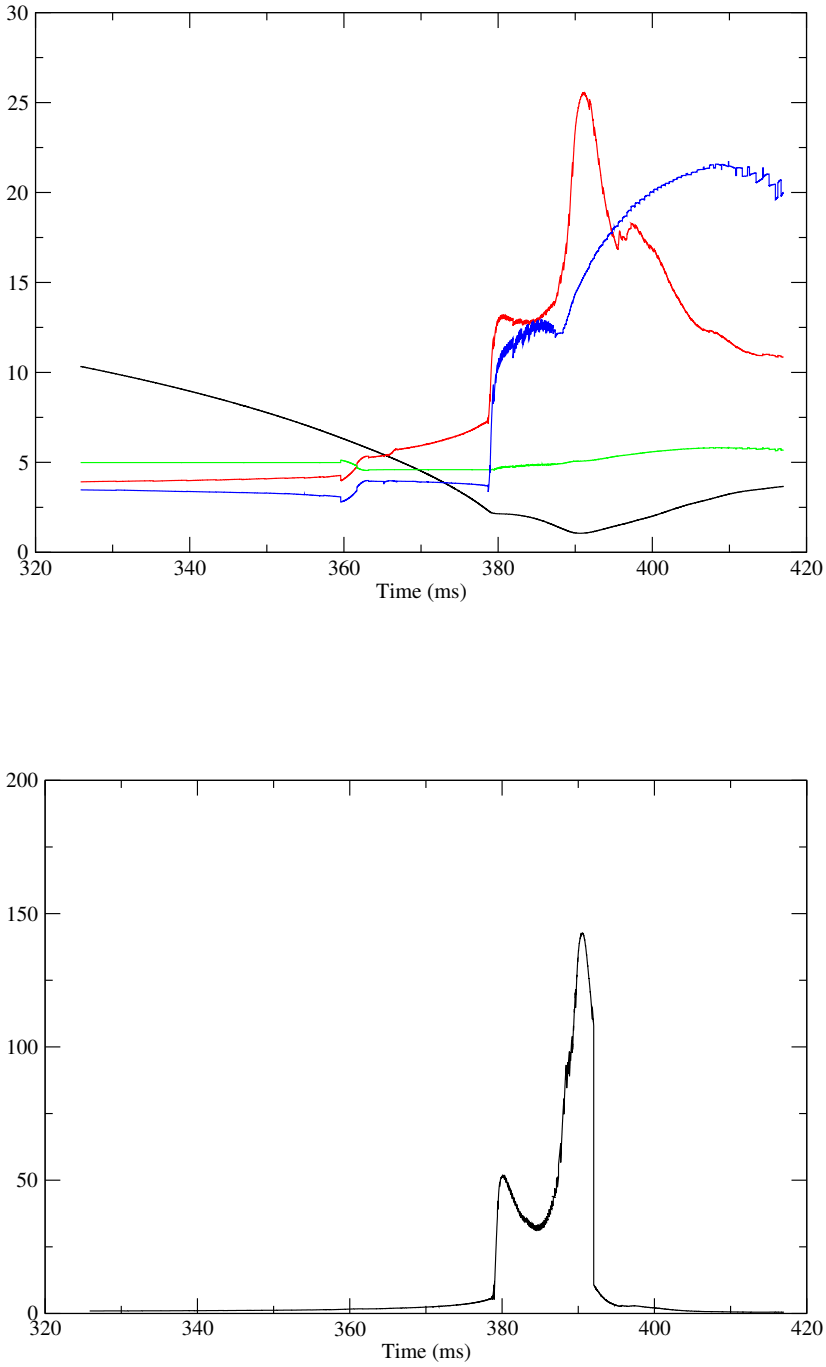

Figure 6.16: Temporal evolution of physical quantities for particle 1557. The black(top), red, green, blue, black(bottom) show radial position(in 100 km), temperature(GK), electron fraction, entropy(k_B), density(in 10^7 g/cm^3), respectively.

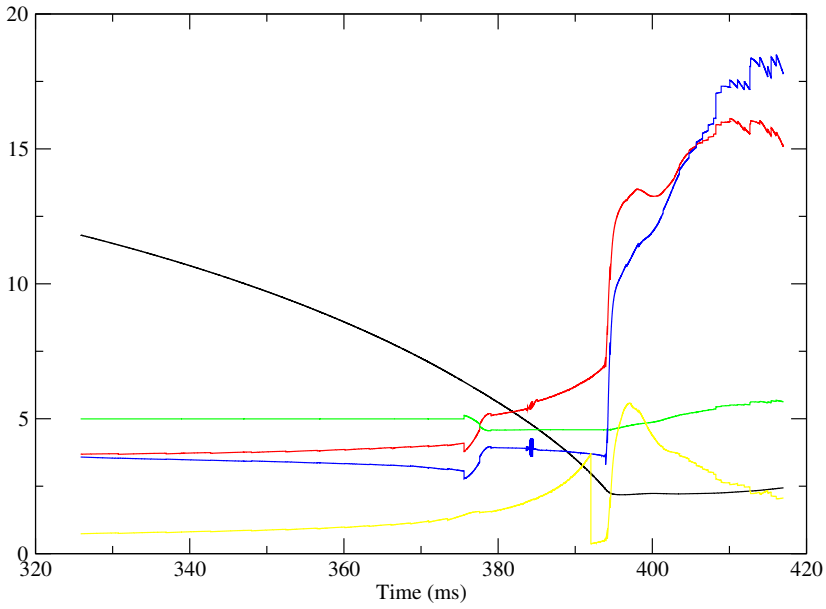

Figure 6.17: Temporal evolution of physical quantities for particle 1572. The black, red, green, blue, yellow lines show the radial position(in 100 km), temperature(GK), electron fraction, entropy(k_B), density(in 10^7 g/cm^3), respectively.

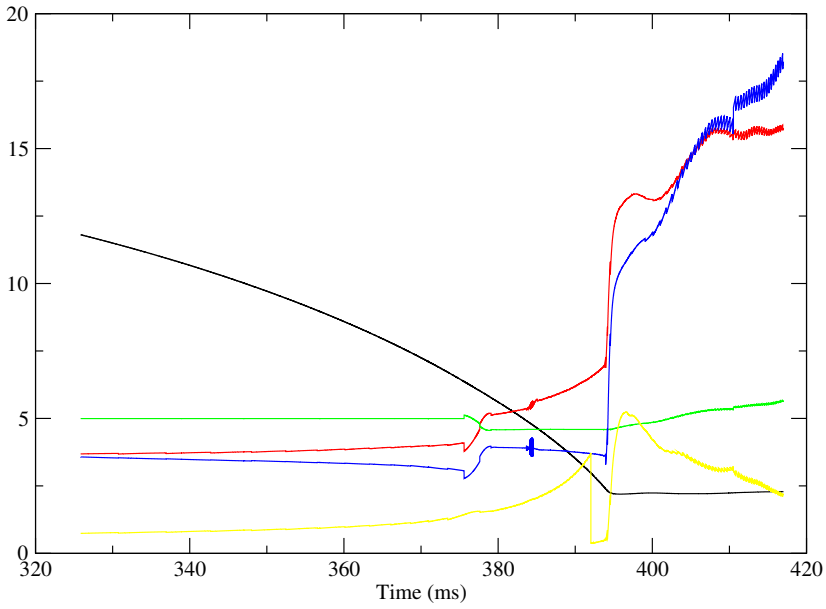

Figure 6.18: Same as Figure 6.17, for particle 1573.

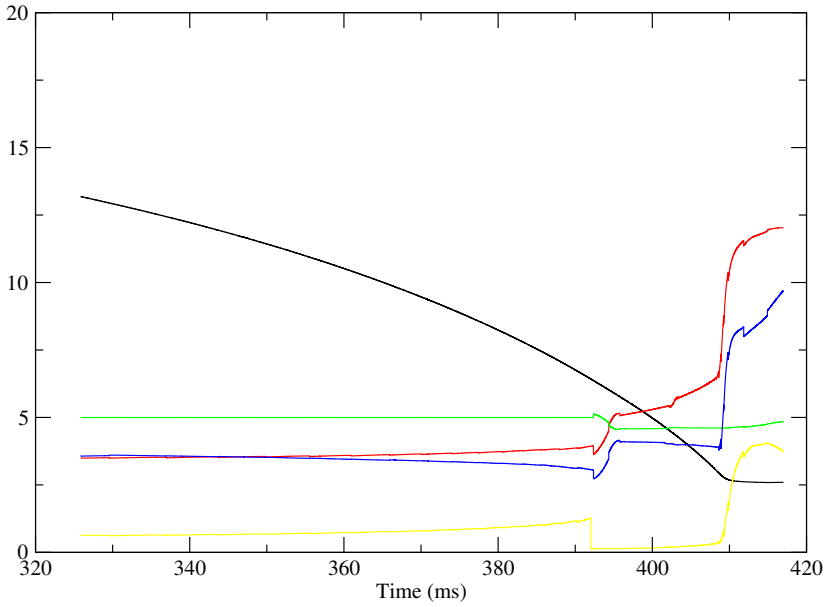

Figure 6.19: Same as Figure 6.17, for particle 1613.

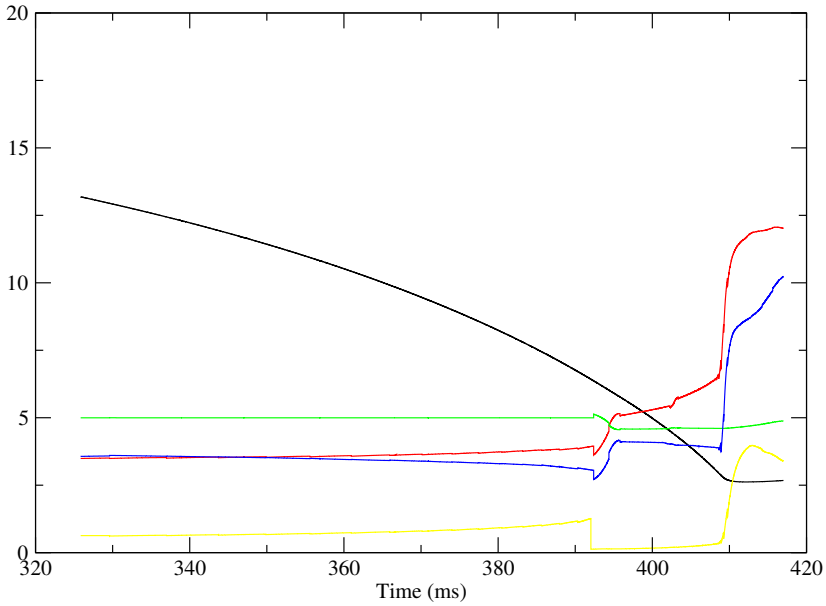

Figure 6.20: Same as Figure 6.17, for particle 1614.

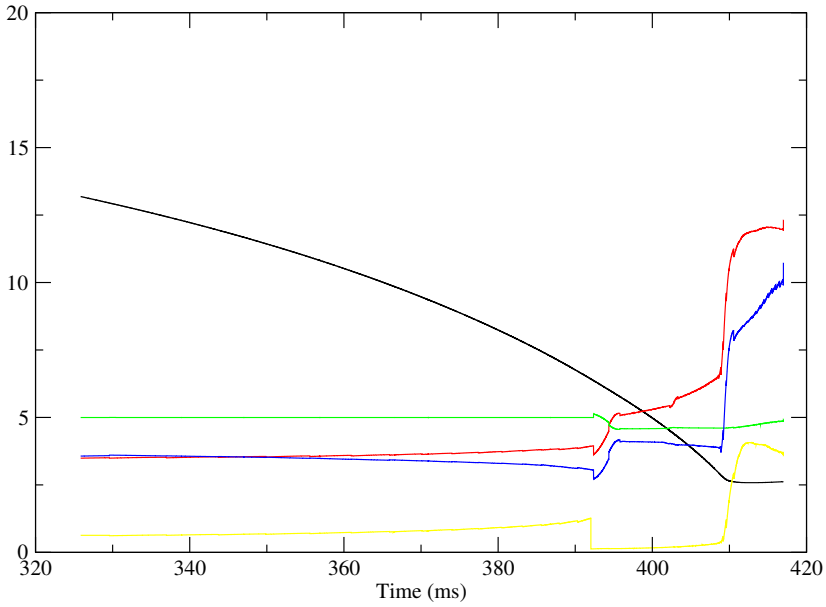

Figure 6.21: Same as Figure 6.17, for particle 1615.

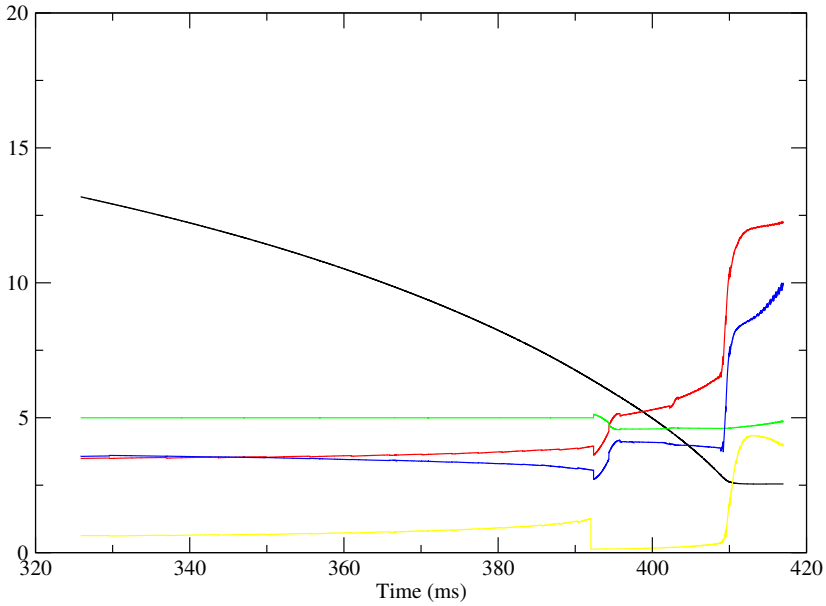

Figure 6.22: Same as Figure 6.17, for particle 1616.

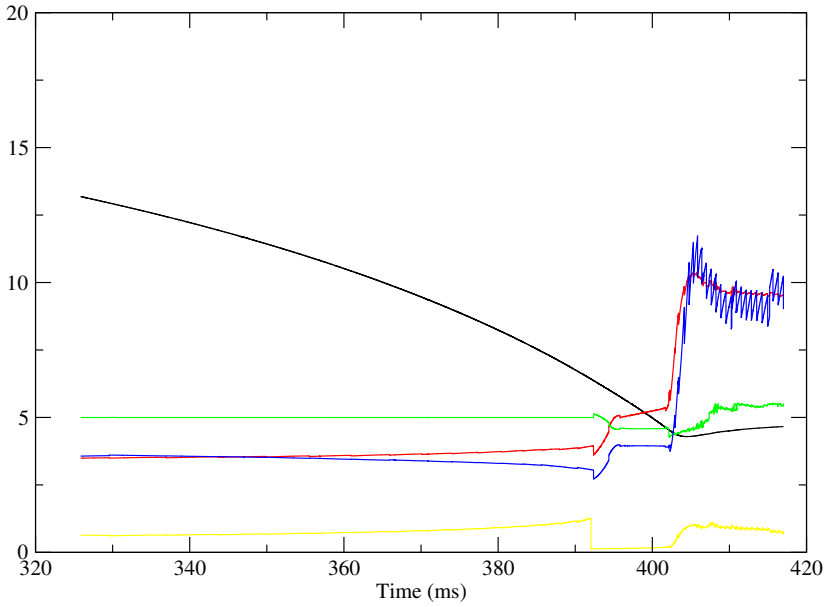

Figure 6.23: Same as Figure 6.17, for particle 1639.

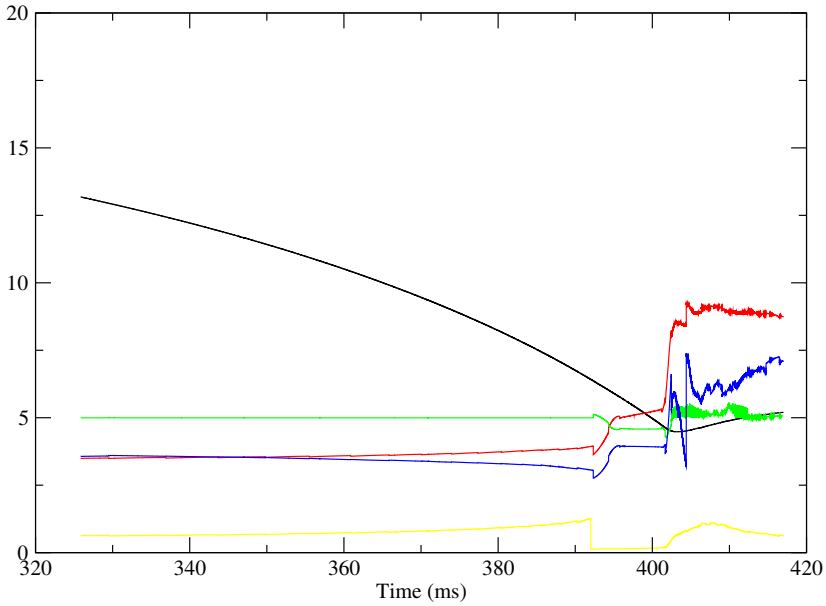

Figure 6.24: Same as Figure 6.17, for particle 1640.

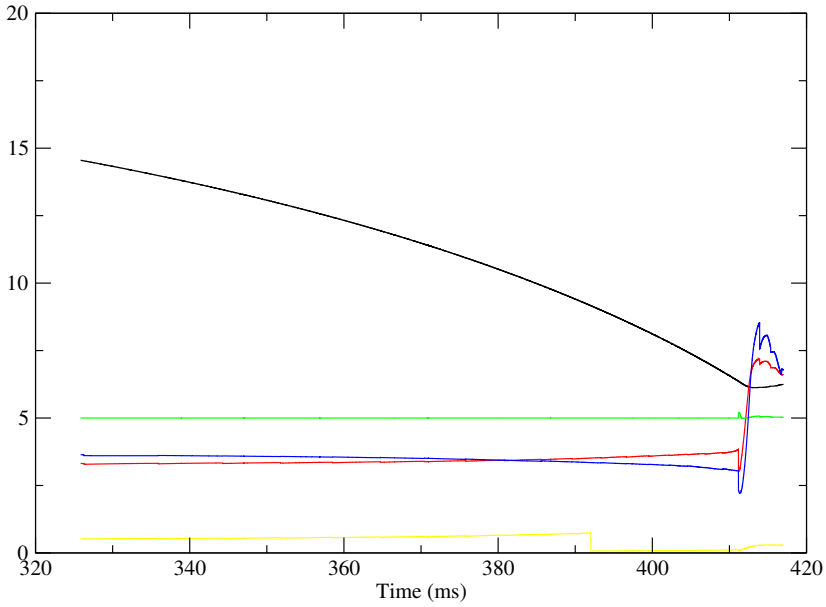

Figure 6.25: Same as Figure 6.17, for particle 1680.

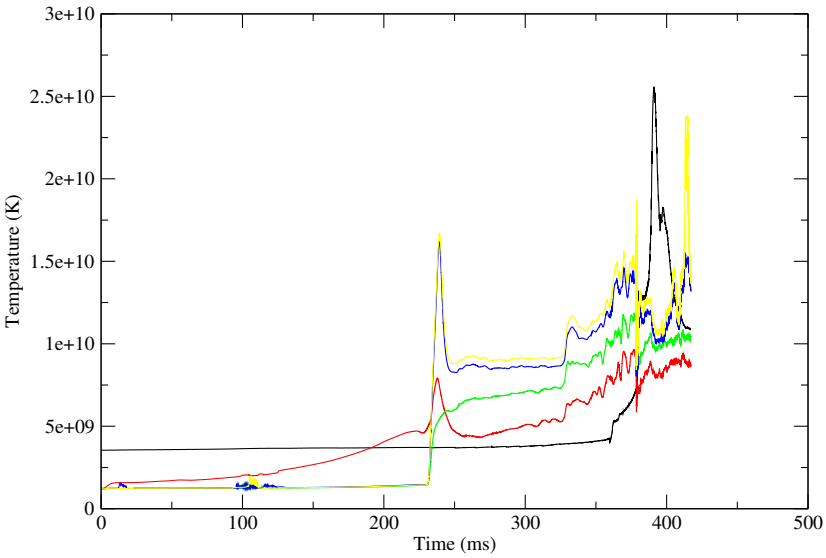

Figure 6.26: Neutrino temperatures as functions of time for the exploding particle 1557. The black, red, green, yellow, bluel ines show the temperatures of hydrodynamics, electron neutrinos, anti-electron neutrinos, muon neutrinos and anti-muon neutrinos, respectively.

must elapse before we can consider the nucleosynthesis caused by the passage of the shock through the outer layers of the core. However, we are able to present some preliminary discussion on the possibility of νp-process nucleosynthesis in this model. We focus on tracer 1557, the deepest of the tracers that are moving outward with significant velocity at this time. In previous studies, (see, e.g., [Fro06a]) it is in the deepest ejected zones, closest to the neutrino source and therefore reaching the highest entropy and neutrino exposure, that experience the strongest νp-process.

In order to extend tracer 1557's thermodynamic history through νp-process conditions (temperatures of 1-3 GK), we have used the declining temperature of this expanding tracer to estimate an expansion timescale, achieving a result of 56 milliseconds, only slightly faster than the freefall timescale (64 milliseconds for these densities), which is often employed as the expansion timescale in parameterized explosion studies. The homologous expansion timescale is calculated as:

$$Time(hom) = (t_f - t_i)/ln(d_f - d_i), \tag{6.1}$$

where the subscript i denotes the value of a quantity when the temperature achives maximum and the subscript f denotes the value of a quantity at the last time given by the tracer particle. For a chosen expansion timescale, the temperature goes as:

$$t = t_i \times exp(-t/3 \times Time(hom)), \tag{6.2}$$

while the density goes as:

$$d = d_i \times exp(-t \times Time(hom)). \tag{6.3}$$

The assumption is made that the temperature and fluxes at the neutrino source are constant, thus the only change in the neutrino exposure is the decrease in flux that results from the tracer's increasing distance from the source. The tracer is assumed to expand with the velocity it has at the end of the simulation. This approach to extending the model is similar to that employed by [Pru05], albeit at an earlier point in the evolution of our still running models.

Figure 6.27 shows the temporal evolution of the mass fractions of the most important species as well as a selection of those species important for the νp-process. Two families of curves are shown, one neglecting neutrino capture reactions on nuclei (solid lines) and the other including these reactions (dotted lines). Common to both families is the early evolution,when a composition initially dominated by free nucleons and α-particles cools, recombining into iron-peak nuclei, first ^{54}Fe and ultimately ^{56}Ni, as the temperature drops below 5 GK. Along with the rise in iron-peak nuclei, one sees a rise in the mass fractions of heavier proton-rich nuclei such as ^{60}Zn, ^{64}Ge, ^{68}Se and ^{72}Kr. The first divergence seen between the calculations which consider and ignore the neutrino-nucleus reactions occurs at 600 milliseconds, when the decline of the free neutron abundance in the "neglected" case is arrested in the "included" case by neutrino captures on protons. The ongoing neutrino captures on protons provide a steady population of free neutrons that can capture on heavy nuclei, once the temperature drops below $\sim$ 3 GK and photodissociation ceases. Captures of these neutrons, particularly (n,p) reactions which accelerate slow beta decays like that of ^{64}Ge, are the driver for the νp-process. Comparison in Figure 6.28 of the integrated reaction fluxes for the "included" case (top) and "neglected" case (bottom) clearly shows a series of proton captures and (n,p) reaction/beta decays reaching as high as strontium. Harder to discern in Figure 6.28 is the fact that critical flows like ^{67}Se to ^{67}As are more than two orders of magnitude larger in the "included" case. While these νp-process fluxes are

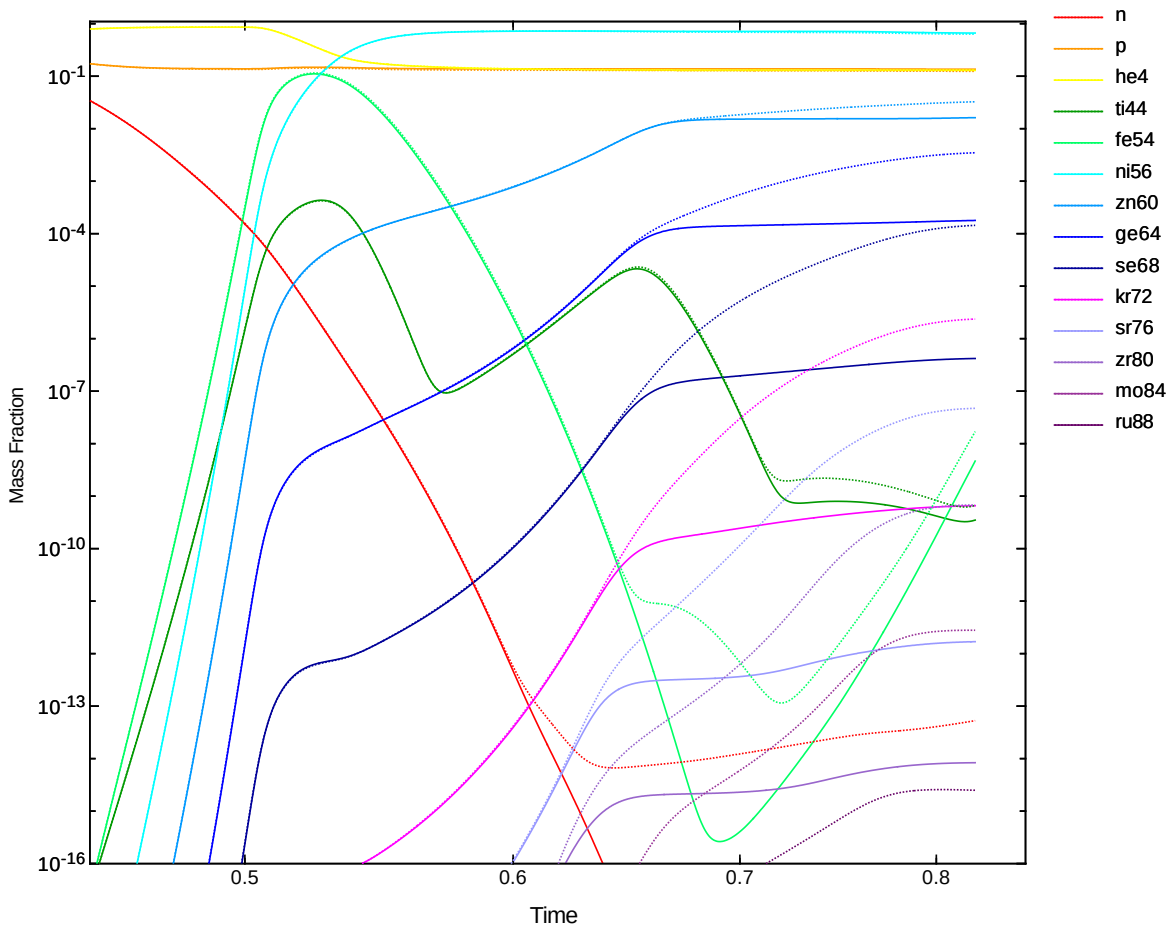

Figure 6.27: Mass Fractions of species critical to the νp-process as a function of time for tracer 1557 with neutrino nucleus reactions included (dotted) and ignored (solid).

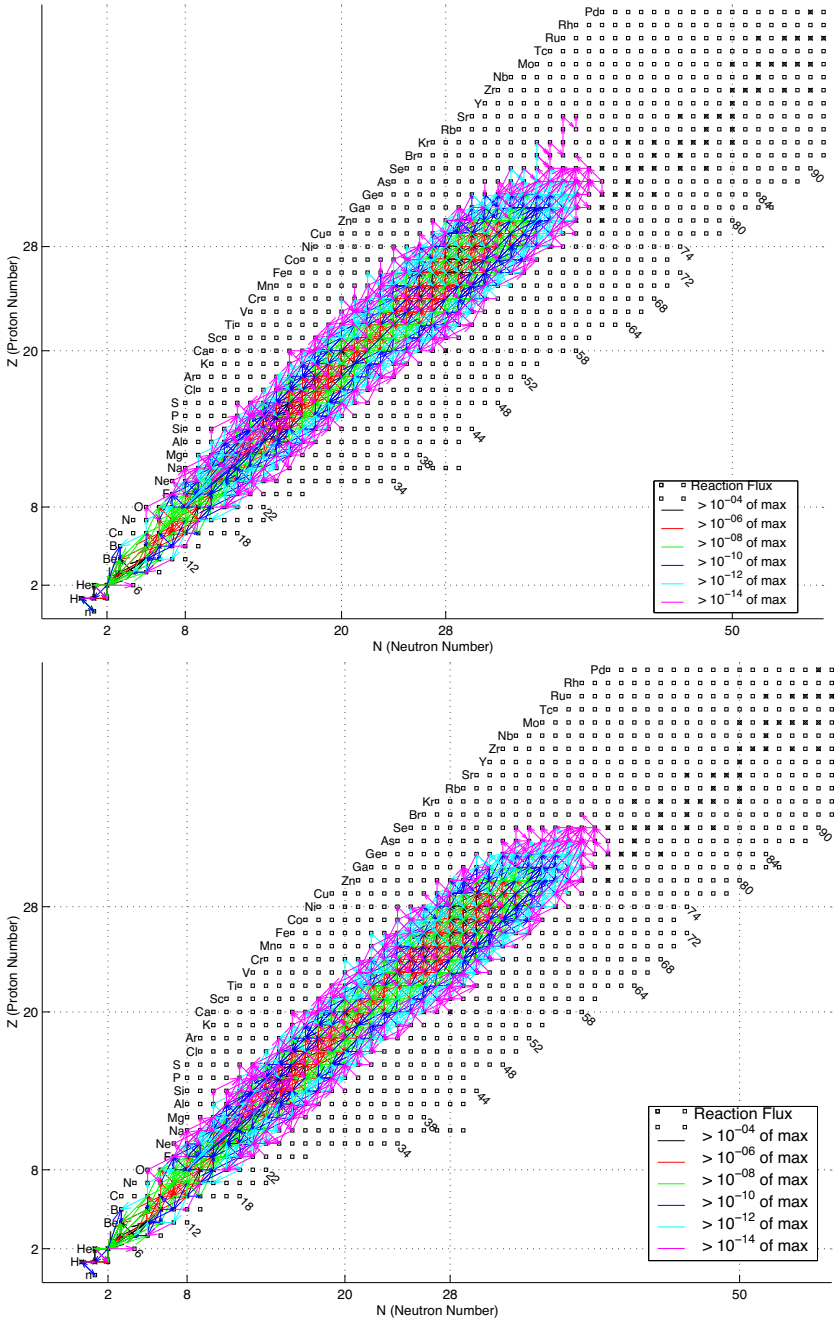

Figure 6.28: Integrated Reaction fluxes for tracer 1557 over the interval corresponding to T= 9 GK to 1 GK with neutrino nucleus reactions included (top) and ignored (bottom).

considerably smaller than the fluxes that built the dominant iron-peak nuclei from free nucleons and α-particles (colored black, red and green in Figure 6.28), they are none the less sufficient to drive a signficantly enhanced population of these light p-process nuclei. Figure 6.27 clearly shows concentrations of ^{68}Se, ^{72}Kr and ^{76}Sr enhanced by several orders of magnitude when the creation of neutrons from protons by neutrinos is considered. Tables 6.1-6 provide more complete listings of the composition at 820 milliseconds (when the temperature drops below 1 GK) in the "included" case and "neglected" case, respectively.

While it is clear from Figure 6.27 and Figure 6.28 that the νp-process does occur for this tracer, they also make clear that the effect is weaker here than in previously published studies [Fro06a, Pru05], where the mass fractions of species like ^{72}Kr can exceed 0.1%. Concentrations at these higher levels are required for the νp-process to be the source of the terrestrial light p-process nuclei. Several factors differentiate the thermodynamic behavior of tracer 1557 from those typical of the νp-process favorable sites discussed by [Fro06a]. First, the average electron and anti-electron neutrino energies are modestly higher (30%) in this simulation while the electron neutrino flux is enhanced and the anti-electron neutrino flux is suppressed (both by $\sim$ 50%). These differences in the neutrino exposure should however enhance the νp-process. Second, the entropy of νp-process favorable sites in [Fro06a] are typically higher by a few than that of tracer 1557. Higher entropy results in a lower density at a common temperature and a more α-rich freezeout. Third, the typical expansion timescale for νp-process favorable sites in [Fro06a] is typically longer, at least for the critical period where the temperature is between 3 GK and 1GK, allowing a longer νp-process phase.

While the final answer to this issue of the strength of the νp-process in these models must await the model's completion, a couple of simple tests help to illuminate the possibilities. First, to test the effect of higher entropy, the result of enhanced or

Table 6.1: Mass Fractions of species from Hydrogen to Vanadium at the end of the νp-process for tracer 1557 with neutrino nucleus reactions included.

n	3.44×10^{-16}	p	1.14×10^{-1}	^{2}H	4.51×10^{-14}	^{3}H	5.78×10^{-22}
^{3}He	2.44×10^{-11}	^{4}He	4.65×10^{-2}	^{6}He	0.00×10^{0}	^{6}Li	1.57×10^{-22}
^{7}Li	5.97×10^{-22}	^{8}Li	0.00×10^{0}	^{9}Li	0.00×10^{0}	^{7}Be	2.54×10^{-11}
^{8}B	4.90×10^{-17}	^{10}B	3.83×10^{-18}	^{9}C	5.00×10^{-17}	^{10}C	1.36×10^{-14}
^{11}C	1.88×10^{-11}	^{12}C	4.22×10^{-13}	^{13}C	7.43×10^{-20}	^{14}C	0.00×10^{0}
^{11}N	0.00×10^{0}	^{12}N	4.64×10^{-15}	^{13}N	9.20×10^{-15}	^{14}N	1.03×10^{-12}
^{15}N	5.83×10^{-20}	^{16}N	0.00×10^{0}	^{17}N	0.00×10^{0}	^{13}O	9.54×10^{-14}
^{14}O	1.45×10^{-8}	^{15}O	6.86×10^{-8}	^{16}O	1.18×10^{-8}	^{17}O	7.13×10^{-20}
^{18}O	0.00×10^{0}	^{16}F	2.18×10^{-17}	^{17}F	2.15×10^{-11}	^{18}F	1.02×10^{-15}
^{19}F	5.70×10^{-22}	^{20}F	0.00×10^{0}	^{21}F	0.00×10^{0}	^{22}F	0.00×10^{0}
^{17}Ne	3.34×10^{-16}	^{18}Ne	1.67×10^{-7}	^{19}Ne	2.67×10^{-11}	^{20}Ne	4.58×10^{-12}
^{21}Ne	6.68×10^{-20}	^{22}Ne	4.30×10^{-22}	^{19}Na	4.09×10^{-15}	^{20}Na	5.95×10^{-12}
^{21}Na	9.33×10^{-12}	^{22}Na	3.64×10^{-13}	^{23}Na	4.30×10^{-21}	^{24}Na	0.00×10^{0}
^{20}Mg	1.18×10^{-14}	^{21}Mg	9.54×10^{-8}	^{22}Mg	1.59×10^{-6}	^{23}Mg	3.09×10^{-12}
^{24}Mg	1.45×10^{-16}	^{25}Mg	5.10×10^{-19}	^{26}Mg	7.28×10^{-24}	^{27}Mg	0.00×10^{0}
^{22}Al	5.24×10^{-14}	^{23}Al	2.09×10^{-11}	^{24}Al	5.84×10^{-12}	^{25}Al	8.07×10^{-12}
^{26}Al	7.04×10^{-14}	^{27}Al	9.41×10^{-18}	^{23}Si	4.96×10^{-17}	^{24}Si	4.98×10^{-8}
^{25}Si	2.03×10^{-7}	^{26}Si	4.90×10^{-6}	^{27}Si	5.80×10^{-11}	^{28}Si	1.76×10^{-13}
^{29}Si	1.37×10^{-17}	^{30}Si	1.12×10^{-19}	^{25}P	1.46×10^{-18}	^{26}P	3.14×10^{-13}
^{27}P	1.06×10^{-7}	^{28}P	1.37×10^{-9}	^{29}P	1.27×10^{-10}	^{30}P	1.61×10^{-11}
^{31}P	3.59×10^{-16}	^{27}S	3.20×10^{-16}	^{28}S	2.04×10^{-7}	^{29}S	6.01×10^{-7}
^{30}S	1.35×10^{-5}	^{31}S	3.71×10^{-10}	^{32}S	6.69×10^{-14}	^{33}S	7.30×10^{-16}
^{34}S	1.40×10^{-17}	^{35}S	0.00×10^{0}	^{29}Cl	1.64×10^{-22}	^{30}Cl	2.00×10^{-15}
^{31}Cl	4.42×10^{-10}	^{32}Cl	1.61×10^{-9}	^{33}Cl	1.80×10^{-10}	^{34}Cl	4.78×10^{-11}
^{35}Cl	4.46×10^{-14}	^{36}Cl	0.00×10^{0}	^{37}Cl	7.68×10^{-24}	^{30}Ar	0.00×10^{0}
^{31}Ar	5.72×10^{-20}	^{32}Ar	5.42×10^{-9}	^{33}Ar	2.22×10^{-6}	^{34}Ar	2.14×10^{-5}
^{35}Ar	2.94×10^{-8}	^{36}Ar	5.88×10^{-12}	^{37}Ar	1.41×10^{-14}	^{38}Ar	4.94×10^{-17}
^{39}Ar	3.23×10^{-23}	^{32}K	0.00×10^{0}	^{33}K	9.31×10^{-24}	^{34}K	6.06×10^{-16}
^{35}K	5.32×10^{-11}	^{36}K	1.80×10^{-9}	^{37}K	7.45×10^{-10}	^{38}K	4.40×10^{-10}
^{39}K	5.47×10^{-10}	^{40}K	4.04×10^{-20}	^{41}K	8.85×10^{-23}	^{42}K	0.00×10^{0}
^{34}Ca	0.00×10^{0}	^{35}Ca	9.31×10^{-16}	^{36}Ca	6.34×10^{-9}	^{37}Ca	4.73×10^{-6}
^{38}Ca	2.15×10^{-5}	^{39}Ca	1.64×10^{-5}	^{40}Ca	3.37×10^{-8}	^{41}Ca	1.53×10^{-12}
^{42}Ca	2.01×10^{-14}	^{43}Ca	1.29×10^{-20}	^{44}Ca	0.00×10^{0}	^{38}Sc	2.58×10^{-17}
^{39}Sc	1.78×10^{-14}	^{40}Sc	5.24×10^{-9}	^{41}Sc	8.17×10^{-9}	^{42}Sc	1.65×10^{-9}
^{43}Sc	5.38×10^{-13}	^{44}Sc	5.68×10^{-20}	^{45}Sc	1.93×10^{-19}	^{39}Ti	1.28×10^{-18}
^{40}Ti	4.52×10^{-12}	^{41}Ti	5.26×10^{-6}	^{42}Ti	2.00×10^{-5}	^{43}Ti	1.25×10^{-8}
^{44}Ti	6.47×10^{-11}	^{45}Ti	4.02×10^{-12}	^{46}Ti	3.50×10^{-13}	^{47}Ti	2.82×10^{-18}
^{48}Ti	1.49×10^{-23}	^{49}Ti	0.00×10^{0}	^{41}V	0.00×10^{0}	^{42}V	8.84×10^{-14}
^{43}V	1.15×10^{-10}	^{44}V	9.68×10^{-9}	^{45}V	2.47×10^{-8}	^{46}V	4.60×10^{-9}
^{47}V	1.42×10^{-11}	^{48}V	1.10×10^{-16}	^{49}V	5.28×10^{-17}	^{50}V	0.00×10^{0}

Table 6.2: Mass Fractions of species from Vanadium to Bromine at the end of the νp-process for tracer 1557 with neutrino nucleus reactions included.

^{51}V	1.81×10^{-22}	^{43}Cr	4.24×10^{-14}	^{44}Cr	1.77×10^{-8}	^{45}Cr	8.77×10^{-6}
^{46}Cr	2.11×10^{-5}	^{47}Cr	3.57×10^{-8}	^{48}Cr	1.27×10^{-9}	^{49}Cr	9.79×10^{-11}
^{50}Cr	1.57×10^{-11}	^{51}Cr	3.25×10^{-14}	^{52}Cr	1.97×10^{-19}	^{53}Cr	1.27×10^{-23}
^{45}Mn	4.28×10^{-20}	^{46}Mn	6.28×10^{-11}	^{47}Mn	1.08×10^{-8}	^{48}Mn	5.59×10^{-8}
^{49}Mn	9.67×10^{-8}	^{50}Mn	5.03×10^{-8}	^{51}Mn	2.68×10^{-8}	^{52}Mn	5.87×10^{-13}
^{53}Mn	1.57×10^{-14}	^{54}Mn	5.48×10^{-22}	^{55}Mn	2.13×10^{-21}	^{56}Mn	0.00×10^{0}
^{44}Fe	0.00×10^{0}	^{45}Fe	0.00×10^{0}	^{46}Fe	2.22×10^{-20}	^{47}Fe	4.08×10^{-10}
^{48}Fe	2.01×10^{-7}	^{49}Fe	7.72×10^{-6}	^{50}Fe	1.34×10^{-5}	^{51}Fe	1.05×10^{-5}
^{52}Fe	7.16×10^{-7}	^{53}Fe	4.41×10^{-9}	^{54}Fe	6.48×10^{-10}	^{55}Fe	5.97×10^{-12}
^{56}Fe	1.19×10^{-12}	^{57}Fe	2.18×10^{-18}	^{58}Fe	0.00×10^{0}	^{59}Fe	0.00×10^{0}
^{47}Co	0.00×10^{0}	^{48}Co	1.27×10^{-21}	^{49}Co	8.66×10^{-20}	^{50}Co	6.66×10^{-13}
^{51}Co	4.44×10^{-10}	^{52}Co	1.67×10^{-7}	^{53}Co	4.96×10^{-7}	^{54}Co	4.04×10^{-7}
^{55}Co	1.88×10^{-6}	^{56}Co	3.62×10^{-7}	^{57}Co	1.82×10^{-10}	^{58}Co	3.14×10^{-17}
^{59}Co	9.96×10^{-15}	^{60}Co	7.07×10^{-22}	^{50}Ni	7.93×10^{-20}	^{51}Ni	1.20×10^{-12}
^{52}Ni	2.74×10^{-10}	^{53}Ni	5.09×10^{-6}	^{54}Ni	2.19×10^{-5}	^{55}Ni	8.49×10^{-5}
^{56}Ni	5.55×10^{-1}	^{57}Ni	4.69×10^{-5}	^{58}Ni	3.02×10^{-6}	^{59}Ni	2.34×10^{-7}
^{60}Ni	2.12×10^{-10}	^{61}Ni	1.19×10^{-14}	^{62}Ni	5.40×10^{-17}	^{63}Ni	0.00×10^{0}
^{53}Cu	0.00×10^{0}	^{54}Cu	1.15×10^{-14}	^{55}Cu	3.44×10^{-13}	^{56}Cu	6.13×10^{-9}
^{57}Cu	1.33×10^{-3}	^{58}Cu	2.36×10^{-3}	^{59}Cu	5.04×10^{-3}	^{60}Cu	6.21×10^{-6}
^{61}Cu	3.30×10^{-9}	^{62}Cu	9.30×10^{-12}	^{63}Cu	2.78×10^{-13}	^{64}Cu	8.15×10^{-20}
^{65}Cu	9.58×10^{-22}	^{54}Zn	0.00×10^{0}	^{55}Zn	1.07×10^{-18}	^{56}Zn	9.52×10^{-14}
^{57}Zn	9.58×10^{-9}	^{58}Zn	4.46×10^{-2}	^{59}Zn	9.15×10^{-2}	^{60}Zn	1.33×10^{-1}
^{61}Zn	6.63×10^{-5}	^{62}Zn	5.16×10^{-6}	^{63}Zn	3.28×10^{-8}	^{64}Zn	2.88×10^{-11}
^{65}Zn	6.88×10^{-15}	^{66}Zn	3.10×10^{-17}	^{67}Zn	7.95×10^{-22}	^{68}Zn	0.00×10^{0}
^{57}Ga	0.00×10^{0}	^{58}Ga	1.43×10^{-22}	^{59}Ga	6.71×10^{-13}	^{60}Ga	3.45×10^{-8}
^{61}Ga	2.59×10^{-4}	^{62}Ga	1.26×10^{-4}	^{63}Ga	2.58×10^{-4}	^{64}Ga	7.00×10^{-7}
^{65}Ga	5.20×10^{-10}	^{66}Ga	3.68×10^{-12}	^{67}Ga	7.17×10^{-15}	^{68}Ga	1.07×10^{-20}
^{69}Ga	2.13×10^{-21}	^{60}Ge	5.09×10^{-15}	^{61}Ge	1.30×10^{-9}	^{62}Ge	8.89×10^{-4}
^{63}Ge	1.16×10^{-3}	^{64}Ge	3.54×10^{-3}	^{65}Ge	2.42×10^{-6}	^{66}Ge	2.62×10^{-7}
^{67}Ge	3.21×10^{-10}	^{68}Ge	1.25×10^{-12}	^{69}Ge	8.97×10^{-16}	^{70}Ge	4.06×10^{-18}
^{71}Ge	7.94×10^{-21}	^{72}Ge	0.00×10^{0}	^{61}As	0.00×10^{0}	^{62}As	1.04×10^{-23}
^{63}As	1.67×10^{-15}	^{64}As	1.67×10^{-10}	^{65}As	1.59×10^{-9}	^{66}As	1.20×10^{-6}
^{67}As	1.67×10^{-6}	^{68}As	1.34×10^{-8}	^{69}As	2.46×10^{-11}	^{70}As	1.49×10^{-13}
^{71}As	2.09×10^{-15}	^{72}As	2.24×10^{-20}	^{73}As	3.39×10^{-21}	^{64}Se	1.47×10^{-16}
^{65}Se	7.98×10^{-14}	^{66}Se	4.15×10^{-9}	^{67}Se	2.83×10^{-6}	^{68}Se	3.69×10^{-5}
^{69}Se	5.85×10^{-8}	^{70}Se	5.08×10^{-9}	^{71}Se	3.08×10^{-11}	^{72}Se	2.23×10^{-13}
^{73}Se	2.73×10^{-16}	^{74}Se	3.53×10^{-18}	^{75}Se	1.44×10^{-20}	^{66}Br	0.00×10^{0}
^{67}Br	5.06×10^{-23}	^{68}Br	4.73×10^{-14}	^{69}Br	5.05×10^{-13}	^{70}Br	2.26×10^{-8}
^{71}Br	4.50×10^{-8}	^{72}Br	8.56×10^{-10}	^{73}Br	2.37×10^{-12}	^{74}Br	3.79×10^{-14}
^{75}Br	4.41×10^{-16}	^{76}Br	1.70×10^{-19}	^{77}Br	1.27×10^{-20}	^{78}Br	0.00×10^{0}

Table 6.3: Mass Fractions of species from Bromine to Palladium at the end of the νp-process for tracer 1557 with neutrino nucleus reactions included.

^{79}Br	0.00×10^{0}	^{68}Kr	0.00×10^{0}	^{69}Kr	1.33×10^{-17}	^{70}Kr	9.50×10^{-13}
^{71}Kr	7.67×10^{-8}	^{72}Kr	6.78×10^{-7}	^{73}Kr	2.76×10^{-9}	^{74}Kr	2.78×10^{-10}
^{75}Kr	2.15×10^{-12}	^{76}Kr	6.53×10^{-14}	^{77}Kr	2.31×10^{-16}	^{78}Kr	1.84×10^{-18}
^{79}Kr	1.90×10^{-20}	^{80}Kr	1.43×10^{-22}	^{72}Rb	4.75×10^{-18}	^{73}Rb	9.55×10^{-16}
^{74}Rb	6.63×10^{-10}	^{75}Rb	1.45×10^{-9}	^{76}Rb	6.67×10^{-11}	^{77}Rb	6.08×10^{-13}
^{78}Rb	6.43×10^{-15}	^{79}Rb	1.56×10^{-16}	^{80}Rb	2.32×10^{-19}	^{81}Rb	2.46×10^{-20}
^{82}Rb	0.00×10^{0}	^{72}Sr	0.00×10^{0}	^{73}Sr	2.09×10^{-20}	^{74}Sr	1.22×10^{-14}
^{75}Sr	1.31×10^{-9}	^{76}Sr	1.56×10^{-8}	^{77}Sr	1.56×10^{-10}	^{78}Sr	2.41×10^{-11}
^{79}Sr	2.46×10^{-13}	^{80}Sr	1.83×10^{-14}	^{81}Sr	1.51×10^{-16}	^{82}Sr	2.64×10^{-17}
^{83}Sr	7.24×10^{-20}	^{84}Sr	1.76×10^{-21}	^{85}Sr	0.00×10^{0}	^{75}Y	0.00×10^{0}
^{76}Y	4.53×10^{-19}	^{77}Y	2.84×10^{-15}	^{78}Y	2.39×10^{-11}	^{79}Y	6.78×10^{-11}
^{80}Y	4.83×10^{-12}	^{81}Y	1.11×10^{-13}	^{82}Y	5.69×10^{-15}	^{83}Y	2.38×10^{-16}
^{84}Y	2.69×10^{-19}	^{85}Y	2.06×10^{-20}	^{77}Zr	2.12×10^{-21}	^{78}Zr	5.96×10^{-16}
^{79}Zr	1.81×10^{-11}	^{80}Zr	3.71×10^{-10}	^{81}Zr	1.02×10^{-11}	^{82}Zr	2.41×10^{-12}
^{83}Zr	1.25×10^{-13}	^{84}Zr	2.32×10^{-15}	^{85}Zr	3.98×10^{-17}	^{86}Zr	7.41×10^{-19}
^{87}Zr	2.56×10^{-20}	^{88}Zr	0.00×10^{0}	^{80}Nb	0.00×10^{0}	^{81}Nb	1.33×10^{-19}
^{82}Nb	7.94×10^{-13}	^{83}Nb	5.01×10^{-12}	^{84}Nb	3.10×10^{-13}	^{85}Nb	1.09×10^{-14}
^{86}Nb	4.48×10^{-16}	^{87}Nb	3.18×10^{-17}	^{88}Nb	8.37×10^{-20}	^{89}Nb	4.90×10^{-21}
^{90}Nb	0.00×10^{0}	^{91}Nb	0.00×10^{0}	^{82}Mo	0.00×10^{0}	^{83}Mo	4.57×10^{-13}
^{84}Mo	7.81×10^{-12}	^{85}Mo	2.87×10^{-13}	^{86}Mo	6.93×10^{-14}	^{87}Mo	4.83×10^{-15}
^{88}Mo	1.27×10^{-16}	^{89}Mo	3.79×10^{-18}	^{90}Mo	2.22×10^{-19}	^{91}Mo	1.54×10^{-22}
^{92}Mo	0.00×10^{0}	^{93}Mo	0.00×10^{0}	^{84}Tc	0.00×10^{0}	^{85}Tc	1.33×10^{-22}
^{86}Tc	8.09×10^{-15}	^{87}Tc	6.34×10^{-14}	^{88}Tc	6.24×10^{-15}	^{89}Tc	4.49×10^{-16}
^{90}Tc	7.86×10^{-18}	^{91}Tc	1.53×10^{-19}	^{92}Tc	6.97×10^{-22}	^{93}Tc	0.00×10^{0}
^{84}Ru	0.00×10^{0}	^{85}Ru	0.00×10^{0}	^{86}Ru	1.88×10^{-23}	^{87}Ru	3.37×10^{-16}
^{88}Ru	3.46×10^{-14}	^{89}Ru	4.77×10^{-15}	^{90}Ru	5.17×10^{-16}	^{91}Ru	1.03×10^{-17}
^{92}Ru	6.02×10^{-19}	^{93}Ru	4.80×10^{-21}	^{94}Ru	0.00×10^{0}	^{87}Rh	0.00×10^{0}
^{88}Rh	0.00×10^{0}	^{89}Rh	1.29×10^{-22}	^{90}Rh	7.75×10^{-18}	^{91}Rh	2.49×10^{-17}
^{92}Rh	1.43×10^{-18}	^{93}Rh	9.58×10^{-20}	^{94}Rh	1.29×10^{-21}	^{95}Rh	0.00×10^{0}
^{89}Pd	0.00×10^{0}	^{90}Pd	0.00×10^{0}	^{91}Pd	8.41×10^{-20}	^{92}Pd	2.11×10^{-18}
^{93}Pd	7.70×10^{-19}	^{94}Pd	2.88×10^{-20}	^{95}Pd	0.00×10^{0}	^{96}Pd	0.00×10^{0}

Table 6.4: Mass Fractions of species from Hydrogen to Vanadium at the end of the νp-process for tracer 1557 with neutrino nucleus reactions ignored.

n	2.69×10^{-22}	p	1.17×10^{-1}	^{2}H	1.95×10^{-19}	^{3}H	0.00×10^{0}
^{3}He	1.09×10^{-16}	^{4}He	4.61×10^{-2}	^{6}He	0.00×10^{0}	^{6}Li	0.00×10^{0}
^{7}Li	0.00×10^{0}	^{8}Li	0.00×10^{0}	^{9}Li	0.00×10^{0}	^{7}Be	1.13×10^{-16}
^{8}B	2.25×10^{-22}	^{10}B	1.67×10^{-23}	^{9}C	2.35×10^{-22}	^{10}C	1.41×10^{-14}
^{11}C	8.42×10^{-17}	^{12}C	4.00×10^{-13}	^{13}C	0.00×10^{0}	^{14}C	0.00×10^{0}
^{11}N	0.00×10^{0}	^{12}N	2.13×10^{-20}	^{13}N	8.71×10^{-15}	^{14}N	2.83×10^{-16}
^{15}N	1.93×10^{-21}	^{16}N	0.00×10^{0}	^{17}N	0.00×10^{0}	^{13}O	4.49×10^{-19}
^{14}O	1.42×10^{-8}	^{15}O	4.62×10^{-9}	^{16}O	1.08×10^{-8}	^{17}O	1.29×10^{-21}
^{18}O	0.00×10^{0}	^{16}F	1.51×10^{-18}	^{17}F	2.04×10^{-11}	^{18}F	9.68×10^{-16}
^{19}F	3.38×10^{-23}	^{20}F	0.00×10^{0}	^{21}F	0.00×10^{0}	^{22}F	0.00×10^{0}
^{17}Ne	2.36×10^{-17}	^{18}Ne	1.64×10^{-7}	^{19}Ne	1.73×10^{-12}	^{20}Ne	4.10×10^{-12}
^{21}Ne	4.59×10^{-20}	^{22}Ne	0.00×10^{0}	^{19}Na	4.11×10^{-15}	^{20}Na	3.86×10^{-13}
^{21}Na	6.89×10^{-12}	^{22}Na	3.04×10^{-13}	^{23}Na	3.30×10^{-21}	^{24}Na	0.00×10^{0}
^{20}Mg	1.23×10^{-14}	^{21}Mg	3.66×10^{-9}	^{22}Mg	1.41×10^{-6}	^{23}Mg	2.57×10^{-12}
^{24}Mg	1.03×10^{-16}	^{25}Mg	3.35×10^{-19}	^{26}Mg	3.85×10^{-24}	^{27}Mg	0.00×10^{0}
^{22}Al	2.06×10^{-15}	^{23}Al	1.90×10^{-11}	^{24}Al	4.86×10^{-12}	^{25}Al	4.69×10^{-12}
^{26}Al	5.88×10^{-14}	^{27}Al	7.52×10^{-18}	^{23}Si	1.59×10^{-18}	^{24}Si	4.88×10^{-8}
^{25}Si	8.83×10^{-8}	^{26}Si	4.28×10^{-6}	^{27}Si	4.87×10^{-11}	^{28}Si	1.47×10^{-13}
^{29}Si	1.06×10^{-17}	^{30}Si	4.55×10^{-20}	^{25}P	1.47×10^{-18}	^{26}P	1.40×10^{-13}
^{27}P	9.52×10^{-8}	^{28}P	1.18×10^{-9}	^{29}P	1.03×10^{-10}	^{30}P	1.46×10^{-11}
^{31}P	3.11×10^{-16}	^{27}S	1.46×10^{-16}	^{28}S	1.95×10^{-7}	^{29}S	5.04×10^{-7}
^{30}S	1.26×10^{-5}	^{31}S	3.35×10^{-10}	^{32}S	5.93×10^{-14}	^{33}S	6.29×10^{-16}
^{34}S	1.26×10^{-17}	^{35}S	0.00×10^{0}	^{29}Cl	1.62×10^{-22}	^{30}Cl	1.72×10^{-15}
^{31}Cl	4.26×10^{-10}	^{32}Cl	1.46×10^{-9}	^{33}Cl	1.62×10^{-10}	^{34}Cl	4.47×10^{-11}
^{35}Cl	4.02×10^{-14}	^{36}Cl	0.00×10^{0}	^{37}Cl	0.00×10^{0}	^{30}Ar	0.00×10^{0}
^{31}Ar	5.04×10^{-20}	^{32}Ar	5.52×10^{-9}	^{33}Ar	2.05×10^{-6}	^{34}Ar	2.07×10^{-5}
^{35}Ar	2.75×10^{-8}	^{36}Ar	4.21×10^{-12}	^{37}Ar	1.27×10^{-14}	^{38}Ar	4.07×10^{-17}
^{39}Ar	0.00×10^{0}	^{32}K	0.00×10^{0}	^{33}K	9.73×10^{-24}	^{34}K	5.74×10^{-16}
^{35}K	5.27×10^{-11}	^{36}K	1.68×10^{-9}	^{37}K	6.95×10^{-10}	^{38}K	4.16×10^{-10}
^{39}K	4.96×10^{-10}	^{40}K	0.00×10^{0}	^{41}K	0.00×10^{0}	^{42}K	0.00×10^{0}
^{34}Ca	0.00×10^{0}	^{35}Ca	9.06×10^{-16}	^{36}Ca	6.54×10^{-9}	^{37}Ca	4.55×10^{-6}
^{38}Ca	2.10×10^{-5}	^{39}Ca	1.54×10^{-5}	^{40}Ca	3.08×10^{-8}	^{41}Ca	1.41×10^{-12}
^{42}Ca	1.87×10^{-14}	^{43}Ca	2.11×10^{-22}	^{44}Ca	0.00×10^{0}	^{38}Sc	2.55×10^{-17}
^{39}Sc	1.78×10^{-14}	^{40}Sc	5.02×10^{-9}	^{41}Sc	7.77×10^{-9}	^{42}Sc	1.58×10^{-9}
^{43}Sc	4.99×10^{-13}	^{44}Sc	3.69×10^{-22}	^{45}Sc	3.35×10^{-21}	^{39}Ti	1.30×10^{-18}
^{40}Ti	4.66×10^{-12}	^{41}Ti	5.22×10^{-6}	^{42}Ti	1.97×10^{-5}	^{43}Ti	1.20×10^{-8}
^{44}Ti	6.04×10^{-11}	^{45}Ti	3.71×10^{-12}	^{46}Ti	3.21×10^{-13}	^{47}Ti	2.70×10^{-19}
^{48}Ti	0.00×10^{0}	^{49}Ti	0.00×10^{0}	^{41}V	0.00×10^{0}	^{42}V	9.00×10^{-14}
^{43}V	1.17×10^{-10}	^{44}V	9.27×10^{-9}	^{45}V	2.37×10^{-8}	^{46}V	4.36×10^{-9}
^{47}V	1.30×10^{-11}	^{48}V	1.15×10^{-18}	^{49}V	2.66×10^{-18}	^{50}V	0.00×10^{0}

Table 6.5: Mass Fractions of species from Vanadium to Bromine at the end of the νp-process for tracer 1557 with neutrino nucleus reactions ignored.

^{51}V	0.00×10^{0}	^{43}Cr	4.43×10^{-14}	^{44}Cr	1.84×10^{-8}	^{45}Cr	8.65×10^{-6}
^{46}Cr	2.06×10^{-5}	^{47}Cr	3.39×10^{-8}	^{48}Cr	1.18×10^{-9}	^{49}Cr	8.97×10^{-11}
^{50}Cr	1.45×10^{-11}	^{51}Cr	1.32×10^{-15}	^{52}Cr	1.51×10^{-23}	^{53}Cr	0.00×10^{0}
^{45}Mn	4.56×10^{-20}	^{46}Mn	6.35×10^{-11}	^{47}Mn	1.08×10^{-8}	^{48}Mn	5.32×10^{-8}
^{49}Mn	9.20×10^{-8}	^{50}Mn	4.81×10^{-8}	^{51}Mn	2.46×10^{-8}	^{52}Mn	8.49×10^{-15}
^{53}Mn	2.02×10^{-15}	^{54}Mn	0.00×10^{0}	^{55}Mn	0.00×10^{0}	^{56}Mn	0.00×10^{0}
^{44}Fe	0.00×10^{0}	^{45}Fe	0.00×10^{0}	^{46}Fe	2.43×10^{-20}	^{47}Fe	4.23×10^{-10}
^{48}Fe	2.07×10^{-7}	^{49}Fe	7.55×10^{-6}	^{50}Fe	1.31×10^{-5}	^{51}Fe	9.93×10^{-6}
^{52}Fe	6.64×10^{-7}	^{53}Fe	4.12×10^{-9}	^{54}Fe	6.04×10^{-10}	^{55}Fe	1.39×10^{-14}
^{56}Fe	8.13×10^{-17}	^{57}Fe	0.00×10^{0}	^{58}Fe	0.00×10^{0}	^{59}Fe	0.00×10^{0}
^{47}Co	0.00×10^{0}	^{48}Co	1.35×10^{-21}	^{49}Co	9.14×10^{-20}	^{50}Co	6.68×10^{-13}
^{51}Co	4.48×10^{-10}	^{52}Co	1.62×10^{-7}	^{53}Co	4.77×10^{-7}	^{54}Co	3.90×10^{-7}
^{55}Co	1.81×10^{-6}	^{56}Co	6.04×10^{-10}	^{57}Co	2.38×10^{-13}	^{58}Co	2.90×10^{-23}
^{59}Co	7.72×10^{-18}	^{60}Co	0.00×10^{0}	^{50}Ni	8.59×10^{-20}	^{51}Ni	1.24×10^{-12}
^{52}Ni	2.84×10^{-10}	^{53}Ni	5.09×10^{-6}	^{54}Ni	2.17×10^{-5}	^{55}Ni	8.42×10^{-5}
^{56}Ni	5.48×10^{-1}	^{57}Ni	4.19×10^{-5}	^{58}Ni	2.91×10^{-6}	^{59}Ni	1.28×10^{-7}
^{60}Ni	4.54×10^{-11}	^{61}Ni	7.87×10^{-17}	^{62}Ni	3.22×10^{-19}	^{63}Ni	0.00×10^{0}
^{53}Cu	0.00×10^{0}	^{54}Cu	1.18×10^{-14}	^{55}Cu	3.50×10^{-13}	^{56}Cu	6.24×10^{-9}
^{57}Cu	1.34×10^{-3}	^{58}Cu	2.40×10^{-3}	^{59}Cu	5.14×10^{-3}	^{60}Cu	2.61×10^{-6}
^{61}Cu	1.07×10^{-9}	^{62}Cu	2.15×10^{-13}	^{63}Cu	1.22×10^{-14}	^{64}Cu	0.00×10^{0}
^{65}Cu	0.00×10^{0}	^{54}Zn	0.00×10^{0}	^{55}Zn	1.13×10^{-18}	^{56}Zn	9.97×10^{-14}
^{57}Zn	1.00×10^{-8}	^{58}Zn	4.65×10^{-2}	^{59}Zn	9.57×10^{-2}	^{60}Zn	1.32×10^{-1}
^{61}Zn	4.28×10^{-5}	^{62}Zn	4.57×10^{-6}	^{63}Zn	2.09×10^{-8}	^{64}Zn	4.77×10^{-12}
^{65}Zn	2.61×10^{-16}	^{66}Zn	1.55×10^{-21}	^{67}Zn	0.00×10^{0}	^{68}Zn	0.00×10^{0}
^{57}Ga	0.00×10^{0}	^{58}Ga	1.53×10^{-22}	^{59}Ga	7.18×10^{-13}	^{60}Ga	3.70×10^{-8}
^{61}Ga	2.64×10^{-4}	^{62}Ga	1.14×10^{-4}	^{63}Ga	2.27×10^{-4}	^{64}Ga	2.91×10^{-7}
^{65}Ga	1.51×10^{-10}	^{66}Ga	3.39×10^{-14}	^{67}Ga	1.70×10^{-16}	^{68}Ga	0.00×10^{0}
^{69}Ga	0.00×10^{0}	^{60}Ge	5.59×10^{-15}	^{61}Ge	1.44×10^{-9}	^{62}Ge	9.02×10^{-4}
^{63}Ge	1.05×10^{-3}	^{64}Ge	2.29×10^{-3}	^{65}Ge	9.69×10^{-7}	^{66}Ge	9.78×10^{-8}
^{67}Ge	7.02×10^{-11}	^{68}Ge	3.95×10^{-14}	^{69}Ge	5.67×10^{-18}	^{70}Ge	9.12×10^{-22}
^{71}Ge	0.00×10^{0}	^{72}Ge	0.00×10^{0}	^{61}As	0.00×10^{0}	^{62}As	1.18×10^{-23}
^{63}As	1.73×10^{-15}	^{64}As	1.54×10^{-10}	^{65}As	1.06×10^{-9}	^{66}As	4.69×10^{-7}
^{67}As	5.46×10^{-7}	^{68}As	1.15×10^{-9}	^{69}As	1.39×10^{-12}	^{70}As	8.48×10^{-16}
^{71}As	2.36×10^{-17}	^{72}As	1.31×10^{-23}	^{73}As	0.00×10^{0}	^{64}Se	1.56×10^{-16}
^{65}Se	7.58×10^{-14}	^{66}Se	2.34×10^{-9}	^{67}Se	9.84×10^{-7}	^{68}Se	4.25×10^{-6}
^{69}Se	4.62×10^{-9}	^{70}Se	3.63×10^{-10}	^{71}Se	1.29×10^{-12}	^{72}Se	2.95×10^{-15}
^{73}Se	1.30×10^{-18}	^{74}Se	5.08×10^{-22}	^{75}Se	0.00×10^{0}	^{66}Br	0.00×10^{0}
^{67}Br	2.92×10^{-23}	^{68}Br	1.69×10^{-14}	^{69}Br	5.96×10^{-14}	^{70}Br	1.70×10^{-9}
^{71}Br	2.51×10^{-9}	^{72}Br	2.28×10^{-11}	^{73}Br	3.92×10^{-14}	^{74}Br	1.04×10^{-16}
^{75}Br	1.34×10^{-18}	^{76}Br	9.64×10^{-23}	^{77}Br	0.00×10^{0}	^{78}Br	0.00×10^{0}

Table 6.6: Mass Fractions of species from Bromine to Palladium at the end of the νp-process for tracer 1557 with neutrino nucleus reactions ignored.

^{79}Br	0.00×10^{0}	^{68}Kr	0.00×10^{0}	^{69}Kr	4.87×10^{-18}	^{70}Kr	9.36×10^{-14}
^{71}Kr	4.44×10^{-9}	^{72}Kr	2.28×10^{-8}	^{73}Kr	7.04×10^{-11}	^{74}Kr	6.73×10^{-12}
^{75}Kr	3.24×10^{-14}	^{76}Kr	5.17×10^{-16}	^{77}Kr	4.77×10^{-19}	^{78}Kr	6.66×10^{-22}
^{79}Kr	0.00×10^{0}	^{80}Kr	0.00×10^{0}	^{72}Rb	2.82×10^{-19}	^{73}Rb	3.29×10^{-17}
^{74}Rb	1.67×10^{-11}	^{75}Rb	3.23×10^{-11}	^{76}Rb	9.09×10^{-13}	^{77}Rb	6.40×10^{-15}
^{78}Rb	4.56×10^{-17}	^{79}Rb	3.33×10^{-19}	^{80}Rb	2.42×10^{-22}	^{81}Rb	0.00×10^{0}
^{82}Rb	0.00×10^{0}	^{72}Sr	0.00×10^{0}	^{73}Sr	1.27×10^{-21}	^{74}Sr	4.06×10^{-16}
^{75}Sr	3.03×10^{-11}	^{76}Sr	2.58×10^{-10}	^{77}Sr	2.04×10^{-12}	^{78}Sr	2.99×10^{-13}
^{79}Sr	1.99×10^{-15}	^{80}Sr	7.37×10^{-17}	^{81}Sr	3.79×10^{-19}	^{82}Sr	1.27×10^{-19}
^{83}Sr	0.00×10^{0}	^{84}Sr	0.00×10^{0}	^{85}Sr	0.00×10^{0}	^{75}Y	0.00×10^{0}
^{76}Y	1.07×10^{-20}	^{77}Y	4.81×10^{-17}	^{78}Y	3.10×10^{-13}	^{79}Y	7.91×10^{-13}
^{80}Y	4.01×10^{-14}	^{81}Y	7.46×10^{-16}	^{82}Y	3.11×10^{-17}	^{83}Y	8.88×10^{-19}
^{84}Y	2.31×10^{-22}	^{85}Y	0.00×10^{0}	^{77}Zr	5.15×10^{-23}	^{78}Zr	1.00×10^{-17}
^{79}Zr	2.22×10^{-13}	^{80}Zr	3.45×10^{-12}	^{81}Zr	8.11×10^{-14}	^{82}Zr	1.81×10^{-14}
^{83}Zr	7.68×10^{-16}	^{84}Zr	1.01×10^{-17}	^{85}Zr	1.39×10^{-19}	^{86}Zr	9.82×10^{-22}
^{87}Zr	0.00×10^{0}	^{88}Zr	0.00×10^{0}	^{80}Nb	0.00×10^{0}	^{81}Nb	1.27×10^{-21}
^{82}Nb	6.33×10^{-15}	^{83}Nb	3.49×10^{-14}	^{84}Nb	1.77×10^{-15}	^{85}Nb	5.30×10^{-17}
^{86}Nb	1.62×10^{-18}	^{87}Nb	1.11×10^{-19}	^{88}Nb	0.00×10^{0}	^{89}Nb	0.00×10^{0}
^{90}Nb	0.00×10^{0}	^{91}Nb	0.00×10^{0}	^{82}Mo	0.00×10^{0}	^{83}Mo	3.46×10^{-15}
^{84}Mo	4.83×10^{-14}	^{85}Mo	1.55×10^{-15}	^{86}Mo	3.52×10^{-16}	^{87}Mo	2.21×10^{-17}
^{88}Mo	4.78×10^{-19}	^{89}Mo	1.13×10^{-20}	^{90}Mo	5.92×10^{-22}	^{91}Mo	0.00×10^{0}
^{92}Mo	0.00×10^{0}	^{93}Mo	0.00×10^{0}	^{84}Tc	0.00×10^{0}	^{85}Tc	0.00×10^{0}
^{86}Tc	4.37×10^{-17}	^{87}Tc	3.12×10^{-16}	^{88}Tc	2.85×10^{-17}	^{89}Tc	1.87×10^{-18}
^{90}Tc	2.58×10^{-20}	^{91}Tc	3.17×10^{-22}	^{92}Tc	0.00×10^{0}	^{93}Tc	0.00×10^{0}
^{84}Ru	0.00×10^{0}	^{85}Ru	0.00×10^{0}	^{86}Ru	0.00×10^{0}	^{87}Ru	1.82×10^{-18}
^{88}Ru	1.65×10^{-16}	^{89}Ru	2.12×10^{-17}	^{90}Ru	2.19×10^{-18}	^{91}Ru	4.07×10^{-20}
^{92}Ru	2.00×10^{-21}	^{93}Ru	0.00×10^{0}	^{94}Ru	0.00×10^{0}	^{87}Rh	0.00×10^{0}
^{88}Rh	0.00×10^{0}	^{89}Rh	0.00×10^{0}	^{90}Rh	3.53×10^{-20}	^{91}Rh	1.07×10^{-19}
^{92}Rh	5.42×10^{-21}	^{93}Rh	0.00×10^{0}	^{94}Rh	0.00×10^{0}	^{95}Rh	0.00×10^{0}
^{89}Pd	0.00×10^{0}	^{90}Pd	0.00×10^{0}	^{91}Pd	3.90×10^{-22}	^{92}Pd	8.96×10^{-21}
^{93}Pd	2.10×10^{-21}	^{94}Pd	0.00×10^{0}	^{95}Pd	0.00×10^{0}	^{96}Pd	0.00×10^{0}

extended neutrino heating, we have artificially reduced the density for tracer 1557 by a factor of 10 and re-examined the nucleosynthesis that results. Figure 6.29 reflects this stronger νp-process with an increased divergence between thecases with neutrino-nucleus reactions included and neglected. Figure 6.30 shows a stronger νp-process, the result of a larger neutron abundance caused by the higher entropy. However, the overall effect on the mass fractions of species like ^{68}Se, ^{72}Kr and ^{76}Sr is more modest than this stronger νp-process implies, with abundances only moderately higher than the standard entropy case. The increased entropy also reduces the total mass fraction of heavy nuclei from more than 70% to less than 10%. This provides fewer seeds for the νp-process. This can be seen in the smaller mass fractions for the A$>$ 60 species in Figure 6.29 near 620 milliseconds, the point when the "included" and "neglected" cases diverge, compared to Figure 6.27. Thus even a large increase in entropy may not make tracer 1557 a better νp-process site.

While it is unlikely that tracer 1557 will have its entropy increased by a factor of 10 as it continues its progress away from the proto-neutron star, the rate of this expansion is a considerable uncertainty in this preliminary analysis. To investigate this issue, we have increased by a factor of three the expansion timescale used to extend tracer 1557's history. The effects of the resultant slower expansion on the abundances of the key species is shown in Figure 6.31. While the behavior prior to the cessation of photodisintegration is very similar to that displayed in Figure 6.27, except for the dilated time axis, the latter behavior shows a much more pronounced νp-process. For example, the mass fraction of ^{72}Kr shows 5 orders of magnitude divergence between "included" and "neglected" cases verses three when tracer 1557's standard values were used. This effect is also reflected in the integrated reaction fluxes, shown for this slower expanding trial in Figure 6.32. Clearly the extent to which tracer 1557 is decelerated as it progress outward will have a strong impact on its suitability as a νp-process site.

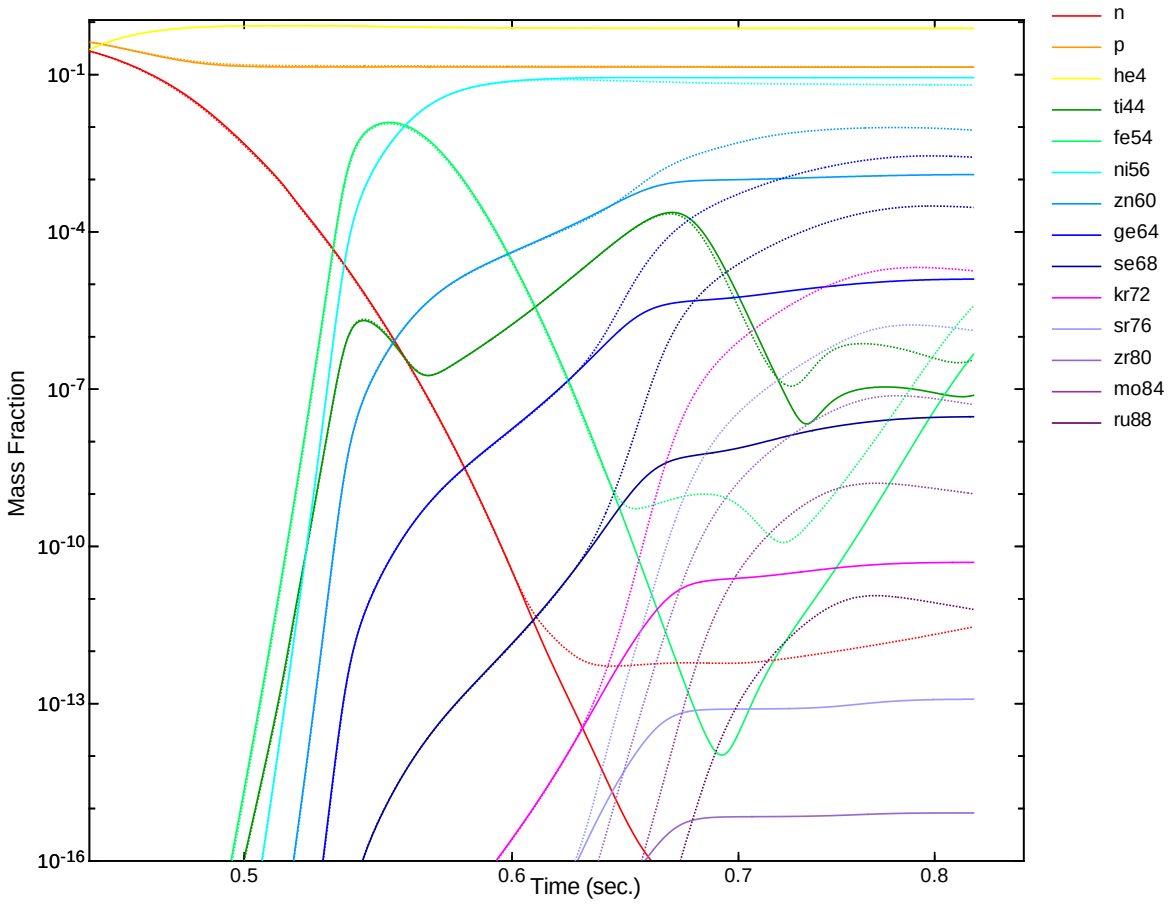

Figure 6.29: Mass Fractions of species critical to the νp-process as a function of time for tracer 1557 in the case of enhanced entropy with neutrino nucleus reactions included (dotted) and ignored (solid).

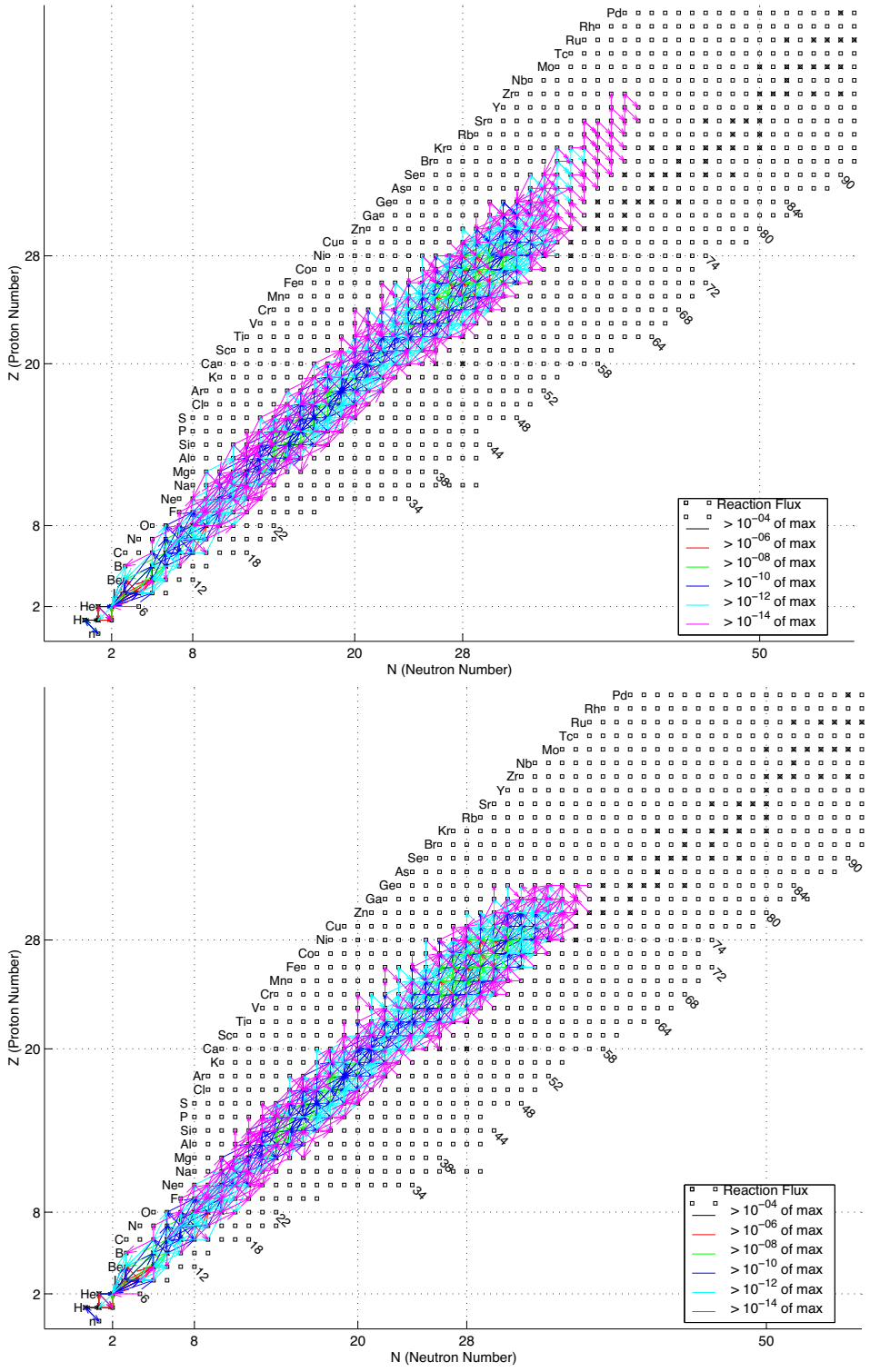

Figure 6.30: Integrated Reaction fluxes for tracer 1557 in the case of enhanced entropy over the interval corresponding to T= 9 GK to 1 GK with neutrino nucleus reactions included (top) and ignored (bottom)

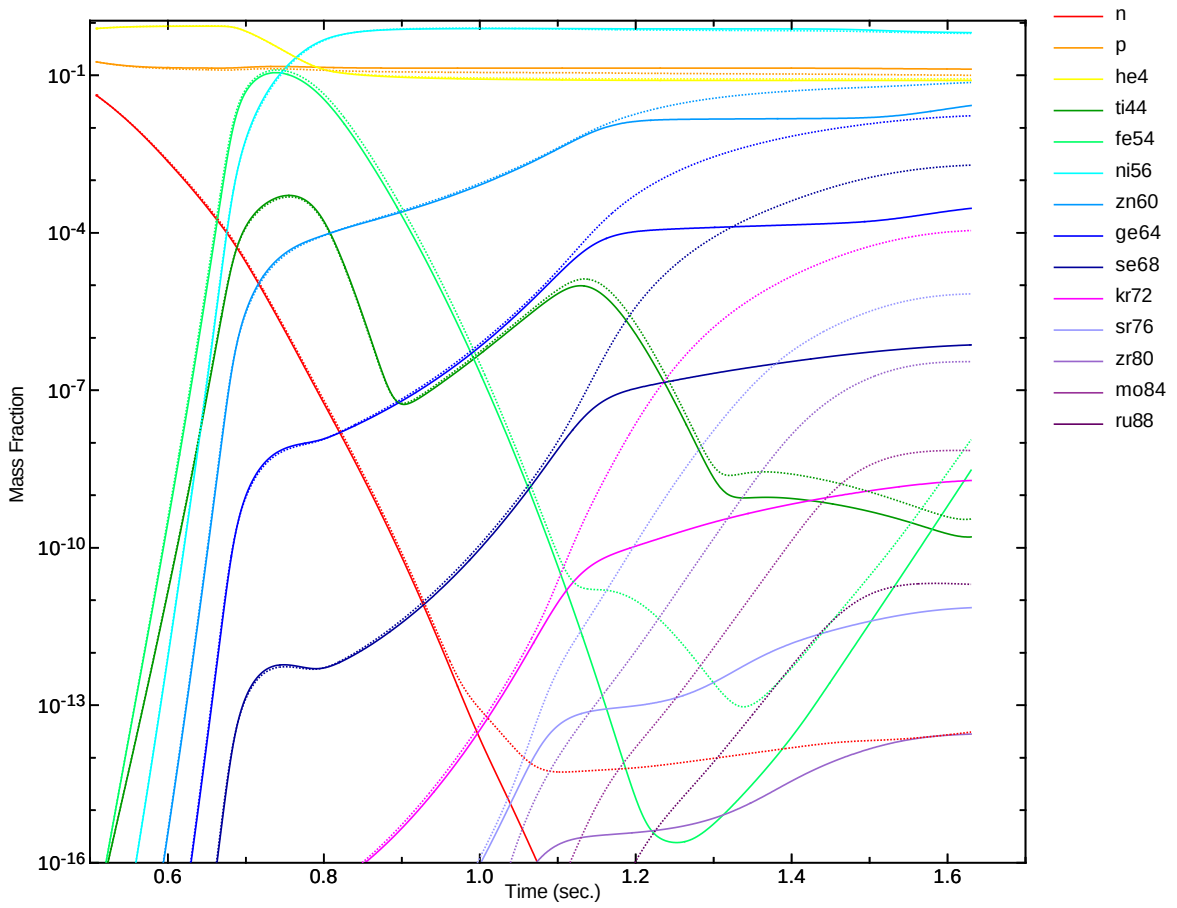

Figure 6.31: Mass Fractions of species critical to the νp-process as a function of time for tracer 1557 in the case of prolonged expansion, with neutrino nucleus reactions included (dotted) and ignored (solid).

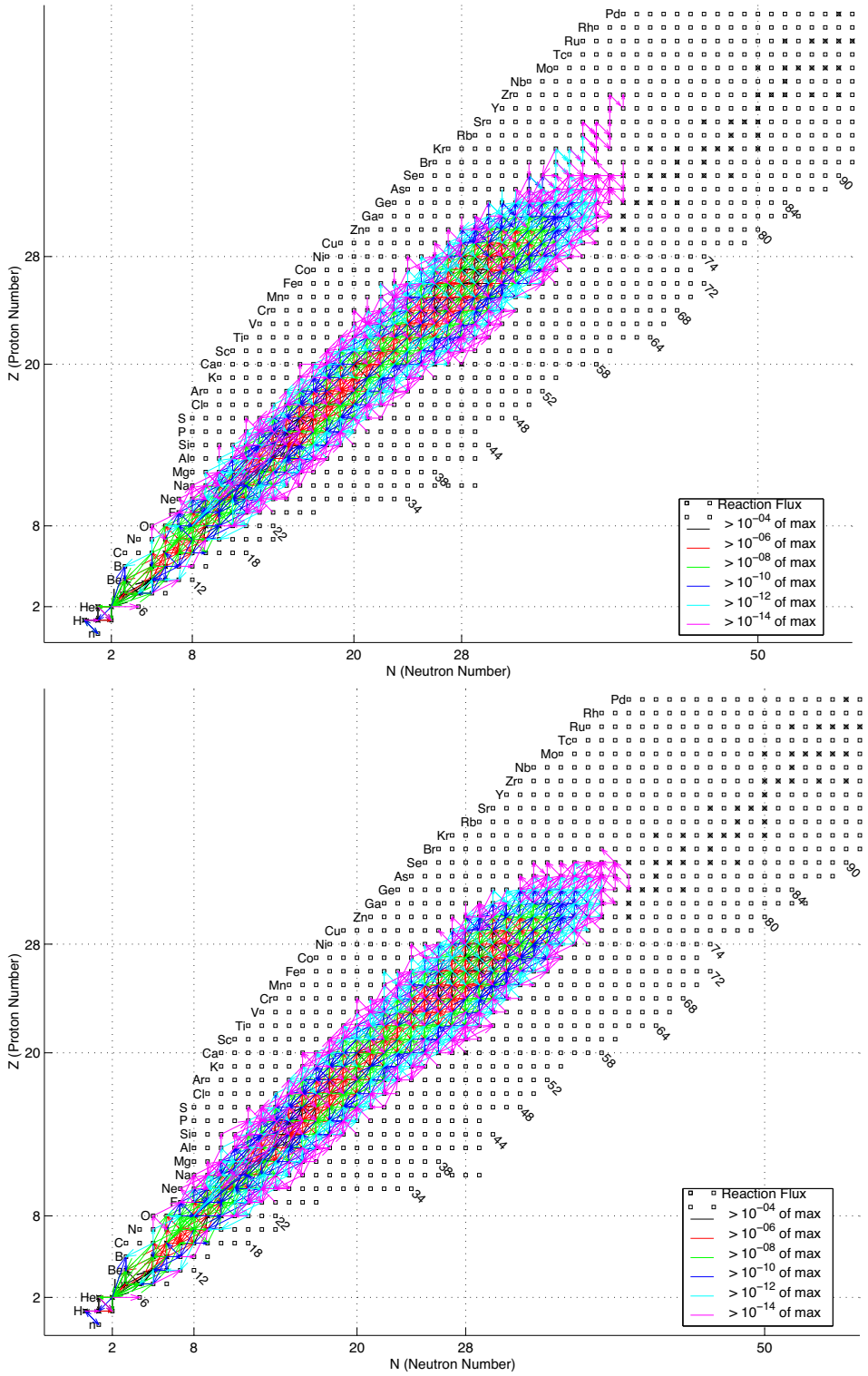

Figure 6.32: Integrated Reaction fluxes for tracer 1557 in the case of prolonged expansion over the interval corresponding to T= 9 GK to 1 GK with neutrino nucleus reactions included (top) and ignored (bottom)

6.3 Conclusion and outlook

The tracer particle method has been successfully applied to supernova simulations. In the case of the Heger12 model, we have obtained a successful explosion. With the tracer particle data on hand, we have begun post-processing nucleosynthesis calculations that will ultimately allow us to compare our result to observations. Many previous simulations suggested the explosion asymmetry, as inferred from polarization studies, is correlated with the rotation of the core. However, as seen in our simulations, the hydrodynamic instabilities alone can produce large-scale asphericities. Analysis of the tracer particle data generated by supernova simulations can reveal the aspherical geometry of the ejecta. Subsequent post-processing nucleosynthesis calculations can give the information on the distribution of elements. To fully study the geometry and the mechanism of supernova explosions, 3D simulations is needed. The implementation of 3D Lagrangian tracers into the CHIMERA code is underway. For 2D simulations, we use thousands of tracer particles. In the case of 3D simulations, we expect to use more than one million tracer particles. This presents a challenge due the openings of numerous files. Saving and analyzing the huge data set will also be very challenging.

The analysis presented in Chapter 6 demonstrates the possibilities that an accurate tracer implementation opens. By allowing detailed post-processing nucleosynthesic calculations as well as offering an alternative view of the supernova's mechanism, our tracer particles represent a significant addition to the CHIMERA supernova modeling code.

Bibliography

Bibliography

[Aki03] S. Akiyama, J. C. Wheeler, D. L. Meier, and I. Lichtenstadt, Astrophys. J. **584**, 954 (2003).

[And03] S. Ando, Phys. Rev. D **68**, 063002 (2003).

[Arn69] W. Arnett and J. Truran, Astrophys. J. **157**, 339 (1969).

[Auf91] M. B. Aufderheide, E. Baron, and F.-K. Thielemann, Astrophys. J. **370**, 630 (1991).

[Bar85] E. Baron, J. Cooperstein, and S. Kahana, Nucl. Phys. A **440**, 744 (1985).

[Bet85] H. A. Bethe and J. R. Wilson, Astrophys. J. **295**, 14 (1985).

[Blo03] J. M. Blondin, A. Mezzacappa, and C. DeMarino, Astrophys. J. **584**, 971 (2003).

[Blo07] J. M. Blondin and A. Mezzacappa, Nature **445**, 58 (2007).

[Bru85] S. W. Bruenn, Astrophys. J. **58**, S771 (1985).

[Bru89] S. W. Bruenn, Astrophys. J. **341**, 385 (1989).

[Bru07] S. W. Bruenn, C. J. Dirk, A. Mezzacappa, J. C. Hayes, J. M. Blondin, W. R. Hix, and O. E. B. Messer, arXiv.org , astroph/07090537 (2007).

[Bur03] R. Buras, M. Rampp, H.-T. Janka, and K. Kifonidis, Phys. Rev. Lett. **90**, 241101 (2003).

[Bur06] A. Burrows, E. Livne, L. Dessart, C. D. Ott, and J. Murphy, Astrophys. J. **640**, 878 (2006).

[Col84] P. Colella and P. R. Woodward, Journal of Computational Physics **54**, 174 (1984).

[Fed08] C. Federrath, S. C. O. Glover, R. S. Klessen, and W. Schmidt, arXiv.org , astroph/08050196 (2001).

[Fil97] A. V. Filippenko, Astron. Astrophys. **35**, 309 (1997).

[Fro06a] C. Frohlich, P. Hauser, M. Liebendorfer, G. Martinez-Pinedo, F.-K. Thielemann, E. Bravo, N. T. Zinner, W. R. Hix, K. Langanke, A. Mezzacappa, and K. Nomoto, Astrophys. J. **637**, 415 (2006).

[Fro06b] C. Frohlich, G. Martinez-Pinedo, M. Liebendorfer, F.-K. Thielemann, E. Bravo, W.-R. Hix, K. Langanke, and N.-T. Zinner, Phys. Rev. Lett. **96**, 142502 (2006).

[Fry02] C. L. Fryer and M. S. Warren, Astrophys. J. **574**, L65 (2002).

[Ful82] G. M. Fuller, W. A. Fowler, and M. J. Newman, Astrophys. J. **252**, 715 (1982).

[Gao06] Z.-C. Gao, Y. Sun, and Y.-S. Chen, Phys. Rev. C **74**, 054303 (2006).

[Han98] S. Hannestad and G. Raffelt, Astrophys. J. **507**, 339 (1998).

[Her94] M. Herant, W. Benz, W. R. Hix, C. L. Fryer, and S. A. Colgate, Astrophys. J. (1994).

[Hix03] W. R. Hix, O. E. Messer, A. Mezzacappa, M. Liebendörfer, J. Sampaio, K. Langanke, D. J. Dean, and G. Martínez-Pinedo, Phys. Rev. Lett. **91**, 201102 (2003).

[Hix06] W. R. Hix and B. S. Meyer, Nucl. Phys. A **777**, 188 (2006).

[Hof04] P. Hoflich, L. Lang, and A. Khokhlov, "Asymmetric supernova explosions", in *Stellar collapse*, edited by C. L. Fryer, page 237, 2004.

[Jan04] H.-T. Janka, R. Buras, K. Kifonidis, A. Marek, and M. Rampp, arXiv.org , astroph/0401461 (2004).

[Jan07] H.-T. Janka, A. Marek, and F.-S. Kitaura, arXiv.org , astroph/07063056 (2007).

[Kif03] K. Kifonidis, T. Plewa, H.-T. Janka, and E. Müller, Astron. Astrophys. **408**, 621 (2003).

[Kog70] B. Kogan, Astron Zh **47**, 813 (1970).

[Lan03] K. Langanke, G. Martínez-Pinedo, J. M. Sampaio, D. J. Dean, W. R. Hix, O. E. Messer, A. Mezzacappa, M. Liebendörfer, H.-T. Janka, and M. Rampp, Phys. Rev. Lett. **90**, 241102 (2003).

[Lan08] K. Langanke, G. Martínez-Pinedo, B. Müller, H.-T. Janka, A. Marek, W. R. Hix, A. Juodagalvis, and J. M. Sampaio, Phys. Rev. Lett. **100**, 011101 (2008).

[Lat91] J. M. Lattimer and F. Douglas Swesty, Nucl. Phys. A **535**, 331 (1991).

[Leo06] D. C. Leonard, A. V. Filippenko, M. Ganeshalingam, F. J. D. Serduke, W. Li, B. J. Swift, A. Gal-Yam, R. J. Foley, D. B. Fox, S. Park, J. L. Hoffman, and D. S. Wong, arXiv.org , astroph/0603297 (2006).

[Lie01] M. Liebendorfer, A. Mezzacappa, F.-K. Thielemann, O. E. Messer, W.-R. Hix, and S. W. Bruenn, Phys. Rev. D **63**, 103004 (2001).

[Lie05] M. Liebendörfer, M. Rampp, H.-T. Janka, and A. Mezzacappa, Astrophys. J. **620**, 840 (2005).

[Mac99] A. I. MacFadyen and S. E. Woosley, Astrophys. J. **524**, 262 (1999).

[Mar07] A. Marek and H.-T. Janka, arXiv.org , astroph/07083372 (2007).

[May91] R. W. Mayle and J. R. Wilson, "Calculations of Neutrino Heating Supernovae", in *Supernovae*, edited by S. E. Woosley, page 333, 1991.

[Mez99] A. Mezzacappa and O. E. B. Messer, Journal of Computational and Applied Mathematics **109**, 281 (1999).

[Mez01] A. Mezzacappa, M. Liebendörfer, O. E. Messer, W. R. Hix, F.-K. Thielemann, and S. W. Bruenn, Phys. Rev. Lett. **86**, 1985 (2001).

[Mez04] A. Mezzacappa, arXiv.org , astroph/0410085 (2004).

[Moi07] S. G. Moiseenko and G. S. Bisnovatyi-Kogan, Astrophys. J. **311**, S191 (2007).

[Mut87] H. Muther, M. Prakash, and T. L. Ainsworth, Physics Letters B **199**, 469 (1987).

[Nag98] S. Nagataki, T. M. Shimizu, and K. Sato, Astrophys. J. **495**, 413 (1998).

[Nag99] S. Nagataki, Astrophys. J. **511**, 341 (1999).

[Nag06] S. Nagataki, A. Mizuta, and K. Sato, Astrophys. J. **647**, 1255 (2006).

[Ott08] C. D. Ott, A. Burrows, L. Dessart, and E. Livne, arXiv.org , astroph/08061589 (2008).

[Pru05] J. Pruet, S. E. Woosley, R. Buras, H.-T. Janka, and R. D. Hoffman, Astrophys. J. **623**, 325 (2005).

[Ram02] M. Rampp and H.-T. Janka, Astron. Astrophys. **396**, 361 (2002).

[Rau04] T. Rauscher, New Astronomy Reviews **48**, 3 (2004).

[Red98] S. Reddy, M. Prakash, and J. M. Lattimer, Phys. Rev. D **63**, 013009 (1998).

[She98] H. Shen, H. Toki, K. Oyamatsu, and K. Sumiyoshi, Nucl. Phys. A **637**, 435 (1998).

[Sum04] K. Sumiyoshi, H. Suzuki, S. Yamada, and H. Toki, Nucl. Phys. A **730**, 227 (2004).

[Swe94] F. D. Swesty, J. M. Lattimer, and E. S. Myra, Astrophys. J. **425**, 195 (1994).

[Tan08] M. Tanaka, K. Kawabata, K. Maeda, T. Hattori, and K. Nomoto., arXiv.org , astroph/08061589 (2008).

[Tas78] J.-L. Tassoul, *Theory of rotating stars*, Princeton Series in Astrophysics, Princeton: University Press, 1978.

[Thi96] F.-K. Thielemann, K. Nomoto, and M.-A. Hashimoto, Astrophys. J. **460**, 408 (1996).

[Tra04] C. Travaglio, W. Hillebrandt, M. Reinecke, and F.-K. Thielemann, Astron. Astrophys. **425**, 1029.

[Wan02] L. Wang, J. C. Wheeler, P. Höflich, A. Khokhlov, D. Baade, D. Branch, P. Challis, A. V. Filippenko, C. Fransson, P. Garnavich, R. P. Kirshner, P. Lundqvist, R. McCray, N. Panagia, C. S. J. Pun, M. M. Phillips, G. Sonneborn, and N. B. Suntzeff, Astrophys. J. **579**, 671 (2002).

[Woo95] S. E. Woosley and T. A. Weaver, Astrophys. J. **S101**, 181 (1995).

[Woo07] S. E. Woosley and A. Heger, Physics Report **442**, 269 (2007).

[Yam04] S. Yamada and H. Sawai, Astron. Astrophys. **608**, 907 (2004).

[You07] P. A. Young and C. L. Fryer, Astrophys. J. **664**, 1033 (2007).

Vita

Ching-Tsai Lee received his master degree in 2000 from National Sun Yat-Sen University, Taiwan. He received his Doctor Philosophy degree majoring in Physics in 2008 from the University of Tennessee, Knoxville.